

THE INVESTIGATION OF HYDROTHERMAL PLUMES BY THE ACOUSTIC SCINTILLATION  
METHOD

by

GUANGYU XU

(Under the direction of Daniela Di Iorio)

ABSTRACT

The acoustic scintillation method is applied to the investigation and monitoring of a vigorous hydrothermal plume within the Main Endeavour vent field (MEF) at the Endeavour segment of the Juan de Fuca Ridge. A 40 day time series of the plume's vertical velocity and temperature fluctuations was estimated during the experiment. An integral plume model taking into account ambient stratification and horizontal cross flows is established from the conservation equations of mass, momentum, density deficit and dissolved tracers. The consistency of the model result to the experimental data suggests that the tidal oscillations observed in the acoustic scintillation measurement is a result of a tidally varying entrainment velocity that is a function of both the plume axial velocity and the ambient flow.

INDEX WORDS: hydrothermal vent, acoustic scintillation, acoustic back scattering, acoustic forward scattering, suspending particles, turbulence, heatflux

THE INVESTIGATION OF HYDROTHERMAL PLUMES BY THE ACOUSTIC SCINTILLATION  
METHOD

by

GUANGYU XU

B.S., Ocean University of China, 2008

A Thesis Submitted to the Graduate Faculty  
of The University of Georgia in Partial Fulfillment  
of the  
Requirements for the Degree

MASTER OF SCIENCE

ATHENS, GEORGIA

2010

© 2010

Guangyu Xu

All Rights Reserved

THE INVESTIGATION OF HYDROTHERMAL PLUMES BY THE ACOUSTIC SCINTILLATION  
METHOD

by

GUANGYU XU

Approved:

Major Professor: Daniela Di Iorio

Committee: Renato Castelao  
Leonid N. Germanovich

Electronic Version Approved:

Maureen Grasso  
Dean of the Graduate School  
The University of Georgia  
December 2010

## ACKNOWLEDGMENTS

I owe my sincere gratitude and appreciation to the people who have been involved in the completion of this master's thesis work, the first of which has to be no other than my advisor Daniela Di Iorio. First and foremost, it was she who granted me the cherishable opportunity of studying oceanography as a graduate student with her, which I appreciate very much. Daniela is the most patient and methodical teacher I have ever met in my entire career as a student. I need to thank her for all the meticulous instructions she has given me through the past two and a half years. I also need to thank her for guiding me through my research and helping me finish this thesis. Without her help, I could never have made it so far.

I would also like to thank Leonid N. Germanovich (Georgia Institute of Technology) for serving as my committee member and sharing his data which is of crucial importance to the completion of this thesis. I'd like to thank Renato Castelao for serving as my committee member and providing insightful suggestions on this thesis. I have to thank the National Science Foundation (NSF) for funding this research under grant number OCE0449578, which would have been impossible otherwise.

I owe my gratitude to Richard Thomson and Steven Mihaly for sharing their current meter data which is of great importance to understanding the interaction of hydrothermal plumes with the ambient ocean environment.

I am grateful to Trent Moore (Skidway Institute of Oceanography) who designed the scintillation system and helped collect all the data described in this thesis. I need to thank Rene Chave, Murray Clarke and David Lemon (ASL Environmental Science Ltd.) for the design and development of the acoustic scintillation mooring system. I have to thank Patrick Decker (Georgia Institute of Technology) for writing the programs for preprocessing the acoustic scintillation data. I would like to thank the Jason II crew and Alvin crew and

particularly pilots Pat Hickey, Bruce Strickrott, Mark Spear and Sean Kelley for collecting valuable data (including the SM2000 data). In particular, I have to thank Sean who gave me a ride to the ocean bottom over 2000 m deep and showed me around the dark world surrounding Alvin, which was quite an unforgettable experience. I would also like to thank David Butterfield (University of Washington) for his help filtering some of the water samples during one of our cruises.

I need to thank Vicki Soutar (Oconee High School) and Ron Prescott (Jackson County Comprehensive High School) who helped greatly during the cruises and particularly Rachael Parr (East Jackson Middle School) who helped tape and organize the diving videos and make a fabulous mini-movie of the cruise I attended.

I am grateful to Bill Chadwick (Oregon State University), Keir Becker (University of Miami), Raymond Lee (Washington State University) and James Holden (University of Massachusetts) who served as the chief scientists during the cruises and were supportive of our work. I also have to thank the captain and crew of the research vessel Atlantis.

I have to thank Adrian Burd who taught me the necessary knowledge of mathematics and modeling. I'd also like to thank William Miller and Wei-Jun Cai for teaching me chemical oceanography and Brian Binder for biological oceanography.

I'd also like to thank all the graduate students who shared classes with me and particularly Pan Hai for teaching me how to drive (probably the hardest one among all the classes I took). I'd like to thank Vladimir Samarkin for being my diving buddy and helping me get the diving license.

At last, I need to thank my parents who cultivate and support me and those friends who bring bliss and happiness to my life.

## TABLE OF CONTENTS

	Page
ACKNOWLEDGMENTS . . . . .	iv
LIST OF FIGURES . . . . .	ix
LIST OF TABLES . . . . .	xv
CHAPTER	
1 INTRODUCTION . . . . .	1
1.1 THE ENDEAVOUR VENT FIELD . . . . .	1
1.2 MEASURING HEAT FLUX FROM HYDROTHERMAL VENTS . . . . .	4
1.3 MOTIVATION . . . . .	7
1.4 OBJECTIVES . . . . .	8
1.5 THESIS OUTLINE . . . . .	9
2 EXPERIMENTAL APPROACH . . . . .	11
2.1 SUMMARY OF ALL RESEARCH CRUISES . . . . .	11
2.2 CTD RESULTS . . . . .	17
2.3 SAMPLING HYDROTHERMAL VENTS . . . . .	23
2.4 ACOUSTIC SCINTILLATION SYSTEM . . . . .	26
2.5 SM2000 MULTI-BEAM SONAR . . . . .	31
3 FORWARD SCATTERING FROM A HYDROTHERMAL PLUME . . . . .	37
3.1 THEORETICAL ESTIMATION FROM SUSPENDING PARTICLES . . . . .	37
3.2 EFFECT OF TURBULENCE . . . . .	46
4 VERTICAL VELOCITY OF HYDROTHERMAL PLUMES . . . . .	57

4.1	ACOUSTIC SCINTILLATION METHOD . . . . .	57
4.2	VERTICAL VELOCITY OF THE PLUME FROM DANTE . . . . .	61
5	HYDROTHERMAL PLUMES IN HORIZONTAL CROSS FLOWS . . . . .	65
5.1	HORIZONTAL FLOW WITHIN THE AXIAL VALLEY . . . . .	65
5.2	COMPARISON WITH ACOUSTIC SCINTILLATION MEASUREMENTS . .	70
5.3	SYNOPSIS . . . . .	72
6	INTEGRAL MODEL OF HYDROTHERMAL PLUMES . . . . .	76
6.1	INTEGRAL MODEL . . . . .	76
6.2	DIMENSIONAL ANALYSIS . . . . .	77
6.3	GOVERNING EQUATIONS OF THE INTEGRAL MODEL . . . . .	81
6.4	SIMPLIFYING THE CONSERVATION EQUATIONS . . . . .	90
6.5	NUMERICAL SOLUTIONS . . . . .	95
6.6	MODEL RESULTS . . . . .	96
6.7	COMPARISON WITH EXPERIMENTAL DATA . . . . .	101
6.8	SYNOPSIS . . . . .	109
7	BACK SCATTERING FROM THE PLUME . . . . .	112
7.1	BACK SCATTERING FROM TURBULENCE . . . . .	112
7.2	BACK SCATTERING FROM SUSPENDING PARTICLES . . . . .	119
8	CONCLUSIONS AND SUGGESTIONS FOR FUTURE RESEARCH . . . . .	122
8.1	CONCLUSIONS . . . . .	122
8.2	SUGGESTIONS FOR FUTURE RESEARCH . . . . .	124
	BIBLIOGRAPHY . . . . .	125
	APPENDIX	
A	COEFFICIENTS OF THE CONSERVATION EQUATIONS . . . . .	135
A.1	CONSERVATION EQUATION OF MASS . . . . .	135
A.2	CONSERVATION EQUATION OF VERTICAL MOMENTUM . . . . .	135

A.3	CONSERVATION EQUATION OF HORIZONTAL MOMENTUM . . . . .	136
A.4	CONSERVATION EQUATION OF TEMPERATURE ANOMALY . . . . .	137
A.5	CONSERVATION EQUATION OF SALINITY ANOMALY . . . . .	138
A.6	CONSERVATION EQUATION OF DENSITY DEFICIT . . . . .	139

## LIST OF FIGURES

1.1	Juan de Fuca Ridge and the location of the Endeavour segment. . . . .	2
1.2	The Endeavour segment and the location of the Main Endeavour vent Field. . . . .	3
1.3	Main Endeavour vent Field and the location of the main hydrothermal vents. . . . .	5
2.1	The vigorous hydrothermal vent on top of Dante on which the experiment is focused. . . . .	12
2.2	Bathymetry surrounding Dante and the placement of the acoustic scintillation transmitter (TX) and receiver (RX) array. . . . .	13
2.3	CTD transects during Cruise AT15-23 plotted in Alvin's UTM coordinates. . . . .	15
2.4	CTD transects during Cruise AT15-34 plotted in Alvin's UTM coordinates. . . . .	16
2.5	CTD transects during Cruise AT15-36 plotted in Alvin's UTM coordinates. . . . .	17
2.6	Background temperature measured from a CTD cast taken during AT1536001. . . . .	18
2.7	Transmissivity measured across Dante from CTD towys during AT1523002, AT1534003 and AT1536003. . . . .	19
2.8	Temperature anomalies measured across Dante from CTD towys during AT1523002, AT1534003 and AT1536003. . . . .	20
2.9	Transmissivity measured along the axial valley from CTD towys during AT1523001 and AT1534005. . . . .	21
2.10	Temperature anomalies measured along the axial valley from CTD towys during AT1523001 and AT1534005. . . . .	22
2.11	Sampling locations (yellow dots) plotted in Alvin's UTM coordinates. . . . .	24

2.12	Temperature measured at a high temperature vent on Dante using a Hobo high temperature probe. The length of the time series is approximately one year with sampling interval of one hour. Note that, the comb-shape spikes in the time series are due to the Hobo probe's low resolution ( $1^\circ\text{C}$ ). . . . .	25
2.13	Configuration of the transducers showing vertical and horizontal separations.	27
2.14	Configuration of the transmitter and receiver arrays relative to the hydrothermal plume. . . . .	28
2.15	Photo showing the deployment of the Transmitter mooring from the RV Atlantis (photo courtesy of D. DiIorio). . . . .	29
2.16	Configuration of the transmitted signal. . . . .	30
2.17	(a) Digitized amplitude captured by one sampling window where the green dots are the five points over which the quadratic fit is performed (dotted line). (b) Time series of the digitized amplitude as a function of travel time captured by the sampling window from Channel 1. . . . .	32
2.18	The original (blue) and despiked (red) amplitude time series of the received signal. . . . .	33
2.19	Vertical profiling with the SM2000 echosounder. . . . .	35
2.20	Back-scattered image of the plume from Dante. . . . .	35
2.21	Horizontal mode of the SM2000 sonar. . . . .	36
2.22	Horizontal profile of the plume 3m above Dante imaged by the SM2000 sonar.	36
3.1	Single scattering approximation where $\langle u(r) \rangle$ is the coherent line of sight path and $u_f$ is the single scattering of the acoustic field. . . . .	40
3.2	Particle scattering from a hydrothermal plume, in which $\mathbf{r}_0/\mathbf{r}$ is the location of the transmitter/receiver, $\mathbf{r}'$ is the location of a single particle within the plume and $\mathbf{r}_i/\mathbf{r}_o$ is the location of the intercept between the line connecting the transmitter/receiver to the particle and the boundary of the plume. . . .	40

3.3	Square of the scattering amplitude $ f(\mathbf{i}, \mathbf{o}) ^2$ for a rigid sphere with $a = 250\mu\text{m}$ ( $ka = 0.33$ ). Forward scattering is represented by $\theta = 0^\circ$ . . . . .	45
3.4	Variation of $C_{eff}^2$ along the distance between transmitter and receiver. . . . .	49
3.5	Normalized log-amplitude spectrum from measured data (blue) versus the theoretically calculated spectrum (red). . . . .	51
3.6	$\sigma_x^2$ and $\tilde{C}_{eff}^2$ calculated from 2007 deployment on Dante. The dashed line pinpoints the level of mean value. . . . .	52
3.7	(a) Temperature measurements of the plume above Dante from Jason's CTD data. SM2000 sonar images taken at the times pinpointed in figure (a) at 10 m above (b) and 30 m above (c). . . . .	55
3.8	Temperature measurements of the plume from Dante between 19-21 m above the orifice. . . . .	56
3.9	Standard deviation of the temperature variability within the plume from Dante at 20 m above the orifice. The dashed line pinpoints the level of mean value, . . . . .	56
4.1	Measuring a hydrothermal plume's vertical velocity with acoustic scintillation. . . . .	58
4.2	(a) Log-amplitude time series for parallel paths (top panel) and diverging paths (bottom panel). (b) Cross-covariance function for parallel paths. (c) Cross-covariance function for diverging paths. . . . .	59
4.3	Vertical velocity of the plume from Dante at 20 m above the orifice measured in 2007. . . . .	62
4.4	Power spectral density of the plume's vertical velocity measured at 20 m above Dante. . . . .	62
4.5	Tidal height vs the plume's vertical velocity. . . . .	63
5.1	Locations of the current meter deployments by Thomson in 2000 and 2001 and by Berdeal in 2002 and 2003. . . . .	66

5.2	Daily averaged current vectors measured during the 2000 deployment (data courtesy of R. Thomson) within the axial valley at 200 m (upper panel) and 50 m (lower panel) above the bottom which correspond to depths of 1974 and 2124 m respectively. . . . .	68
5.3	Daily averaged mean flow within the central valley measured during the 2001 deployment (data courtesy R. Thomson) at 19 m above bottom at 2175 m depth. (a) scatter plot and (b) stick plot. . . . .	69
5.4	Tidal oscillations within the central valley measured during the 2001 deployment (data courtesy R. Thomson) at 19 m above bottom at 2175 m depth. . . . .	71
5.5	Rotary spectrum of the tidal oscillations measured during the 2001 deployment (data courtesy R. Thomson) at 19 m above bottom at 2175 m depth. . . . .	71
5.6	Pressure vs horizontal flow measured during the 2001 deployment (data courtesy R. Thomson ). . . . .	73
5.7	Tidal height from the OSU tidal inversion model versus horizontal flow extrapolated from T-TIDE. . . . .	73
5.8	Vertical velocity vs horizontal flow . . . . .	74
5.9	$\tilde{C}_{eff}^2$ vs horizontal flow . . . . .	74
6.1	Characteristic length scales of a hydrothermal plume in a stratified environment with a uniform horizontal cross-flow. . . . .	79
6.2	Linear fits performed on the ambient temperature, salinity and density measured from CTD cast AT1536001. The solid lines are the CTD data while the dashed lines are the linear fits shown in equations (6.6) to (6.8). . . . .	82
6.3	A hydrothermal plume is a stratified environment with uniform horizontal flow. . . . .	84
6.4	Radial distribution profiles for the plume velocity and tracer concentration. . . . .	93
6.5	Radius of the plume. . . . .	98
6.6	Trajectory of the plume. . . . .	98
6.7	Radial averaged vertical velocity of the plume. . . . .	99

6.8	Declination angle of the plume's trajectory. . . . .	100
6.9	Density deficit of the plume. . . . .	100
6.10	Estimated horizontal cross-flow at the time of the acoustic scintillation measurement in 2007. The dashed lines pinpoint one standard deviation above and below the mean value. . . . .	101
6.11	The plume's radial-averaged vertical velocity at 20 m above the orifice as a function of the horizontal cross-flow. . . . .	103
6.12	(a) The effect of the bending of the plume on the vertical velocity measurement made at 20 m above the orifice. $S$ is the distance along the plume axis, $w_1$ is the vertical velocity measured at $S = 20$ m and $w_2$ is the vertical velocity measured at 20 m above the orifice. (b) Comparison between the vertical velocity of the plume at 20 m above the orifice and at 20 m away from the orifice along the axis. . . . .	104
6.13	Radius of the plume. . . . .	105
6.14	Radial-averaged vertical velocity of the plume for different drag coefficients: $C_d = 0.01$ (blue line), $C_d = 1$ (black line) and $C_d = 1.7$ (green line). . . . .	106
6.15	Radial-averaged vertical velocity of the plume with initial density deficit $\eta_0 = 310 \text{ kg/m}^3$ (black line) and $\eta_0 = 410 \text{ kg/m}^3$ (blue line). . . . .	107
6.16	$\langle W \rangle$ at 20 m above the orifice as a function of the horizontal cross-flow for different $\alpha$ and $\beta$ combinations. . . . .	108
6.17	Declination angles of the plume: during ebbing tide (dashed line), during flooding tide (solid line) . . . . .	110
7.1	Scattering of sound wave from a turbulent medium. $\mathbf{r}'$ location of the transmitter, $\mathbf{r}$ location of the receiver, $\mathbf{r}_0$ location of a turbulent microstructure within the scattering volume, $\mathbf{k}_i$ incident wave-number. . . . .	115
7.2	Bragg wave-number . . . . .	116

- 7.3 back scattering from suspending particles.  $\mathbf{r}_0$  location of the monostatic transmitter,  $\mathbf{r}'$  location of a single particle,  $\mathbf{r}_i$  intersection between the scattered acoustic line-of-sight and the boundary of the plume,  $\mathbf{R}$  radius of the plume. 121

## LIST OF TABLES

2.1	Cruises with the RV Atlantis using either the ROV Jason II or the HOV Alvin	11
2.2	Temperature Measurements on Dante . . . . .	23
2.3	Particle concentration and number density assuming a particle radius shown as $a$ . . . . .	26
2.4	Channel identification for various transmitter and receiver combinations. . .	27
2.5	Location (Alvin coordinates) and depth of the transmitter and receiver deploy- ments. . . . .	28
2.6	Parameters of the acoustic scintillation system . . . . .	31
2.7	Parameters of the SM2000 sonar system . . . . .	34

## CHAPTER 1

### INTRODUCTION

#### 1.1 THE ENDEAVOUR VENT FIELD

Hydrothermal vents are where geothermally heated fluids exit the seafloor mostly at spreading centers located along Mid-Ocean Ridges which teem with volcanic activity. Hydrothermal vents spew out high-temperature, mineral-rich sea water into the ambient environment. When the hot plume meets the cold ambient sea water, the dissolved minerals in the plume (mainly metal sulfides) precipitate out and make the plume black. Such a vent system is called a ‘black smoker’. Hydrothermal plumes emanating from both the high temperature focused vent (‘black smoker’) and low temperature diffuse flow can impose a significant impact on the local deep ocean environment. The heat and chemical minerals carried by the plumes support an abundant biosphere around the hydrothermal fields and in the meanwhile hydrothermal plumes help disperse organisms and minerals to the local biological community (Roth and Dymond, 1989; Jannasch, 1995; Marsh et al., 2000). In addition to the biological effect, hydrothermal plumes also affect the local current and fluid structure and even induces unique patterns of circulation around the vent field (Stommel, 1982; Thomson et al., 2003, 2005). Therefore hydrothermal vents play an important role in the deep ocean environment.

The Endeavour vent field (EVF) has been under intensive study for more than two decades. The numerous vigorous hydrothermal vents within the EVF make them perfect natural laboratories for the investigation of hydrothermal activity. These vents are located on the Endeavour segment of the Juan de Fuca Ridge. The Juan de Fuca ridge is part of the boundary between the Pacific plate and the Juan de Fuca plate, which is approximately 300

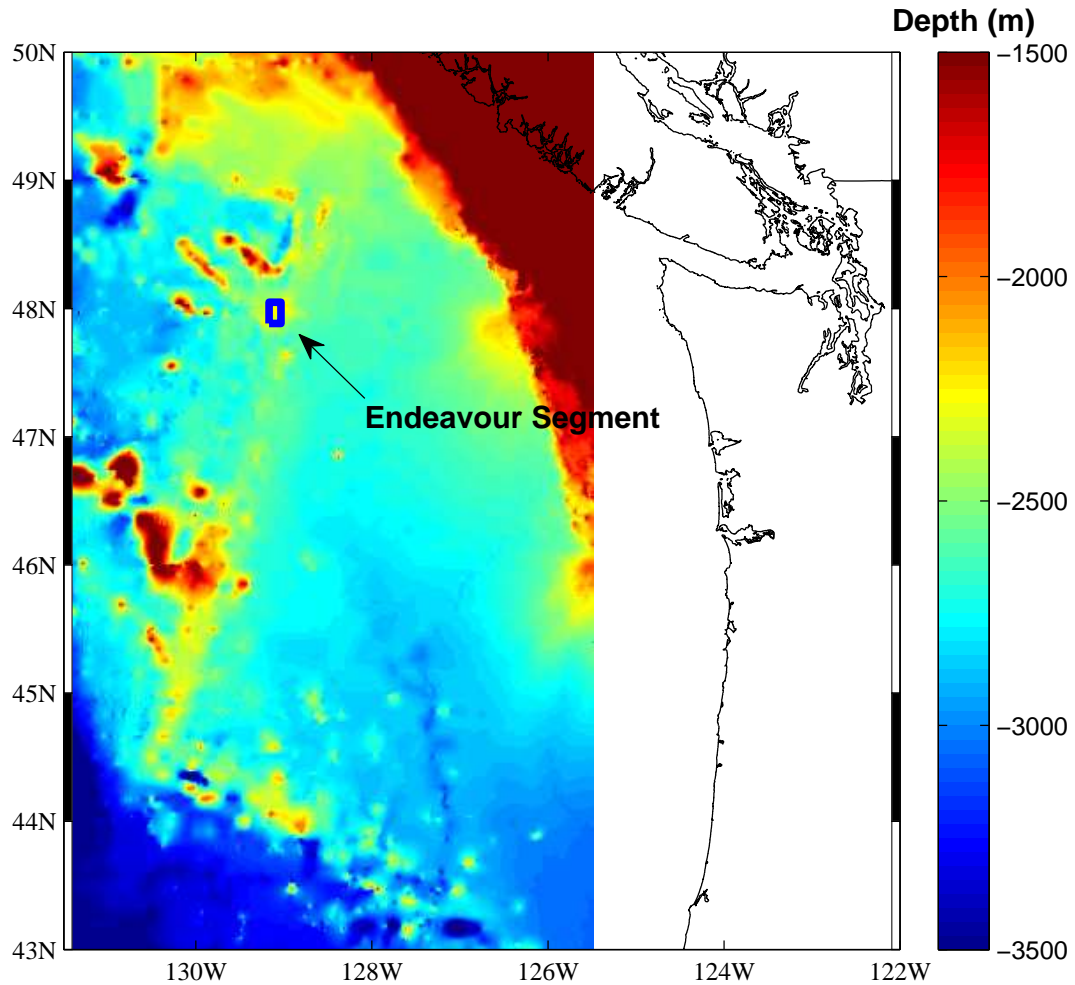


Figure 1.1: Juan de Fuca Ridge and the location of the Endeavour segment.

miles off the coasts of Washington and Oregon (see Figure 1.1). The Juan de Fuca ridge is an intermediate spreading rate ridge diverging at a rate of  $50 \sim 60$  mm per year (Riddihough, 1984). The entire ridge is oriented  $20^\circ$  N and is composed of several individual segments. Among them, the Endeavour segment lies in the northern part where the crest of the ridge reaches 300 m above the surrounding ocean bottom (at a depth of approximately 2400 m) (see Figure 1.1). The crest is cleaved by a 1 km wide and 10 km long axial-valley with an average depth of 100 m. The valley relief is  $100 \sim 150$  m tall (see Figure 1.2).

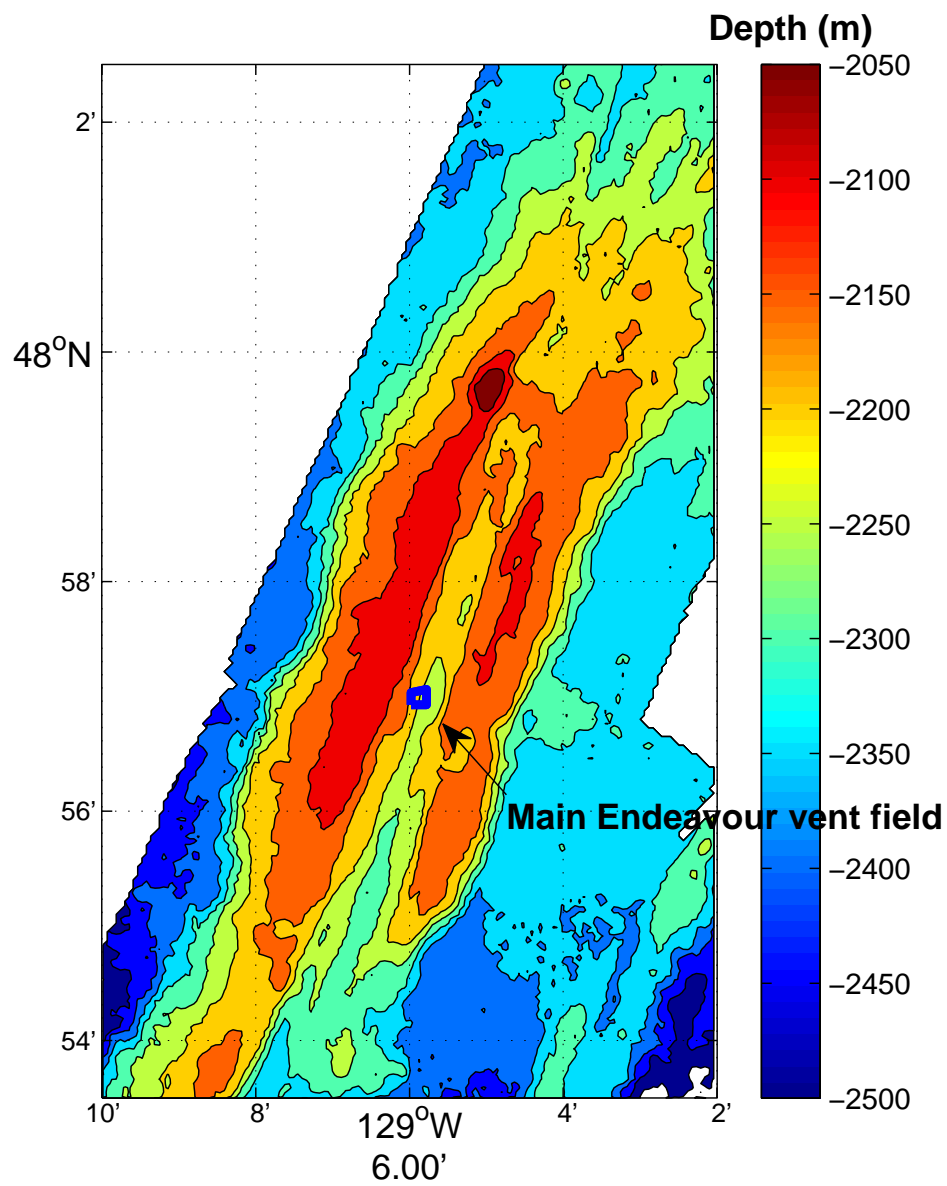


Figure 1.2: The Endeavour segment and the location of the Main Endeavour vent Field.

Within the axial valley of the Endeavour segment there are 5 major vent fields (Mothra to the south, Main Endeavour, High Rise, Salty Dawg and Sasquatch to the north), within which 15 large active sulfide edifices have been discovered with outflow temperatures averaging up to 375°C (Delaney et al., 1992; Kelley et al., 2001). A typical EVF hydrothermal edifice is 30 m wide and 20 m tall while the tallest one, Godzilla, stands up to 45 m high. Among the five vent fields, the Main Endeavour vent field (MEF) is the most intense and active. This field possesses at least 21 venting edifices (see Figure 1.3). Outflow temperatures as high as 380 °C was measured at 3 of those edifices (Kelley et al., 2001). Among the venting edifices in MEF, Dante is the largest and most active one. Dante is located in the Northern vent field. It is 35 m long, 32 m wide and 15 ~ 18 m tall (Fornari and Embley, 1995). Recent measurements show a height of 25 m, which may indicate a significant growth of Dante during the past two decades. During an Alvin dive in 2008, approximately ten high temperature black smokers were discovered on top of Dante with numerous low temperature diffuse flows leaking from both the top and flanks.

## 1.2 MEASURING HEAT FLUX FROM HYDROTHERMAL VENTS

Through mixing between hydrothermal plumes and ambient sea water, a significant amount of heat is transferred into the deep ocean from the sub-seafloor lithosphere. Therefore hydrothermal vents play important roles in the heat circulation between the earth's crust and the deep ocean. The heat removed by hydrothermal vents explain the discrepancy between the theoretically estimated heat loss from a cooling lithosphere to the deep ocean through conduction and the measured heat loss from conductive bottom heat flows (Stein and Stein, 1992, 1994; Ginster and Mottl, 1994). In addition, hydrothermal vents are also believed to be a convenient surrogate of the time-averaged magmatic budget (Baker et al., 1994).

In general, heat is removed from the sub-seafloor lithosphere in three forms. One is through high temperature focused vents (black smokers), another is through low temperature

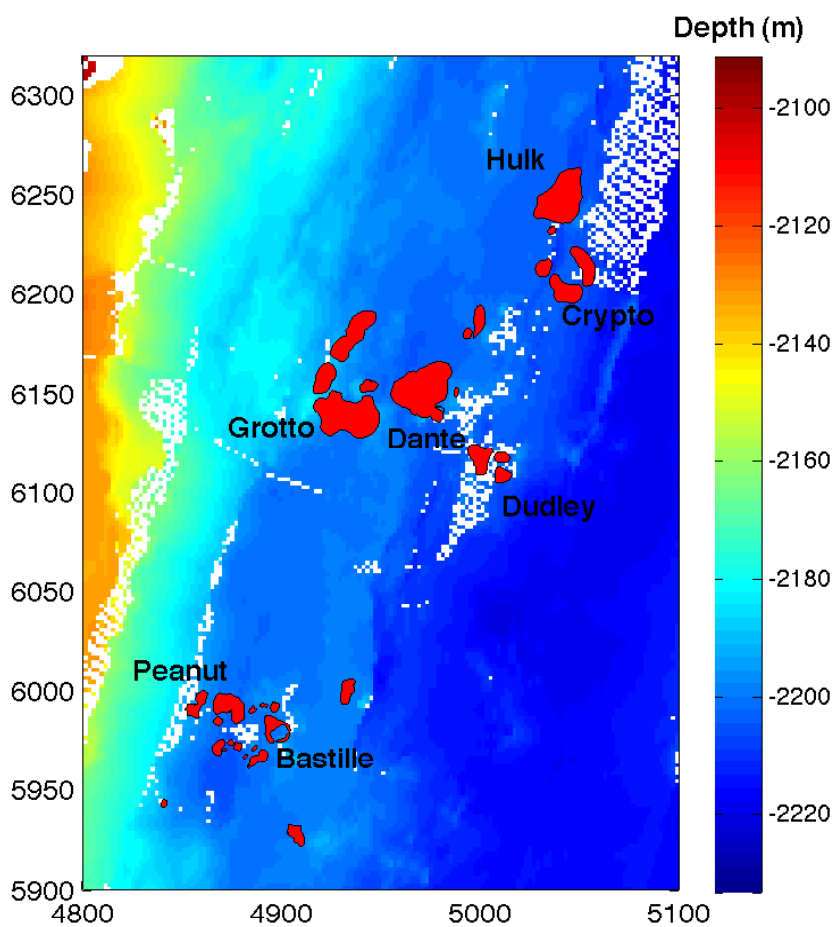


Figure 1.3: Main Endeavour vent Field and the location of the main hydrothermal vents.

diffuse flows and the third is through conductive heat flows at the sea-floor. According to the conductive heat flow measurements over the axial valley floor at the Endeavour segment (Johnson et al., 2010), only 3% of the heat flux of oceanic crustal formation is released by conductive heat flows. Therefore most of the crustal heat is carried by hydrothermal plumes into the deep ocean and thus quantifying heat flux from hydrothermal vents is of crucial importance for measuring heat transport from the earth's crusts to the deep ocean.

Despite knowing the importance of heat flow, measuring the heat flux from hydrothermal vents is by no means an easy task. Previous measurements have been carried out in a variety of ways. One way has been to measure the heat flux at individual high temperature focused vents directly and then sum up the results to extrapolate the heat flux from a hydrothermal edifice or even an entire vent field (Bemis et al., 1993; Ginster and Mottl, 1994). Such an approach provides results in the range 200 ~ 350 MW for MEF. With this method, it is hard to extrapolate the heat flux of an entire vent field from the measurements derived from individual smokers. Besides, since direct measurements are limited to high temperature focused vents, the contribution from diffuse flows is neglected. According to Schultz et al. (1992), Veirs et al. (2006), and Johnson and Hautala (2002), the heat flux from diffuse flows is of the same order of magnitude with, and could be greater than, focused vents. Therefore using heat flux from individual smokers to estimate the total heat flux of an entire vent field will lead to a significant underestimation.

Another way to measure the heat flux has been by surveying the water column at the equilibrium layer (where hydrothermal plumes reach neutral buoyancy with respect to the ambient sea water) (Baker and Massoth, 1987; Thomson et al., 1992), which leads to results in the range 1 ~ 3 GW above MEF. This relatively large result is probably due to the contribution from the other vent fields on the Endeavour segment and therefore the integrated heat flux measured this way is prone to be an overestimation.

A third approach is to set up a control volume enclosing a hydrothermal edifice or an entire vent field and measure the net heat flux leaking through the boundaries of the control

volume, which gives results of 600 MW for MEF (Veirs et al., 2006; Stahr et al., 2000). In this approach, significant temporal and spatial variance is observed in the temperature anomalies and current velocities measured at boundaries of the control volume. Thus it is hard to get a temporally and spatially invariant result to represent the heat flux of the vent field.

In addition to the problems stated previously, an earthquake occurred on June 8, 1999 at the Endeavour segment which significantly changed the vent field behavior. Substantial increases and large-amplitude oscillations were observed in the diffuse flow temperature measurements after the earthquake (Johnson et al., 2000) and therefore pre and post earthquake heat flux measurements need to be compared cautiously.

### 1.3 MOTIVATION

Temporal variability has been observed in numerous studies on hydrothermal systems along mid ocean ridges. In particular, a tidal signal was observed in many cases (Fujioka et al., 1997; Larson and Lilley, 2002; Little et al., 1988; McDuff and Delaney, 1995; Pruis and Johnson, 2004; Kinoshita et al., 1998), which implies that there is significant interaction between tides and hydrothermal systems. All of the research listed above was conducted either at low temperature diffuse flows or in the vicinity of an active hydrothermal edifice. The tidal oscillation observed in diffuse flow temperature and outflow velocity measurements is likely to be a result of the bottom currents and tidal-loading effect (Crone and Wilcock, 2005). Given the unique characteristics of a ‘black smoker’ (high temperature, strong caustic effect), it is hard to get a long-term measurement of the plume’s temperature and flow velocity directly and simultaneously. Only a few time series have been derived so far. Measurements made by conventional current meters and thermistors are restricted by their deployment location. Measurements at vent orifices (Converse et al., 1984) are limited to individual vents, either ‘black smokers’ or diffuse flows, while the ones made at certain levels above (Bemis et al., 1993) suffer from the spatial variation of the plume. Subsequent results may not be used as statistical representatives of the corresponding properties.

In order to investigate the temporal variability of hydrothermal physical properties (temperature variability and flow velocity), an alternate approach is needed to provide long-term, continuous monitoring of a hydrothermal system. With this goal in mind, the acoustic scintillation method is applied. Acoustic scintillation is a phenomenon in which the pattern of the modulation of the acoustic signal is evolving constantly due to the turbulence within the medium. By measuring fluctuations of the received signal, properties of the medium can be recovered through an inverse approach. Generally speaking, acoustic scintillation is an approach to estimating mean and turbulent features of the medium from the measurement of the fluctuation of an acoustic signal passing through it. Acoustic scintillation is a well-proven technology and has been applied in many cases of both atmospheric and oceanographic research during the past 50 years (Clifford and Farmer, 1983; Farmer and Clifford, 1986; Farmer et al., 1987; DiIorio, 1994; DiIorio and Farmer, 1994, 1998).

When applied to the investigation of hydrothermal vents, by analyzing the acoustic signal propagating through the plume (DiIorio et al., 2005), one can get a path-averaged measurement of plume properties like temperature variability and vertical flow. Acoustic scintillation is a non-intrusive technology since the transmitter and receiver are moored outside the plume during the measurement (see Chapter 2 for details about the deployment). Because of its path-averaged and non-intrusive characteristics, acoustic scintillation offers an alternative approach to the long-term monitoring of the integrated hydrothermal plume emanating from high temperature focused vents.

#### 1.4 OBJECTIVES

The major research objectives of this Master's thesis work are summarized as follows:

1. Theoretically quantify the effect of suspending particles on the forward scattering of acoustic signals using the particle concentration density measured from the plume above Dante.

2. Calculate the temperature variability and vertical velocity of the integrated plume above Dante using the acoustic scintillation method.
3. Determine the relationship between the tidal oscillations and the vertical velocity and turbulent intensity of the plume.
4. Estimate the net heat flux of a sulfide structure using the vertical velocity measured by acoustic scintillation and its spatial scale measured by the SM2000 sonar.
5. Establish an integral model to simulate a hydrothermal plume's behavior in an environment with significant horizontal cross flows and ambient stratification. Use the model to investigate a tidally varying entrainment rate.
6. Quantify the effects of the turbulent plume on acoustic back scattering.

## 1.5 THESIS OUTLINE

Chapter 2 is an introduction to the experimental approach. This chapter includes a summary of the research cruises and the data collected. It contains a detailed introduction to the acoustic scintillation system as well as the configuration of its deployment at the MEF. It also introduces the SM2000 multi-beam sonar used for visualizing the plume's shape and spatial scales.

Chapter 3 addresses in detail the scattering effect on acoustic signals imposed by both the turbulent structures (temperature perturbations and turbulent velocity) and suspending particles within a hydrothermal plume. In the first section of this chapter, the contribution of suspending particles to the amplitude fluctuations observed in the received signal is quantified theoretically using the single scattering assumption and Rayleigh scattering approximation. In the second section, the effect of turbulence on the acoustic signal fluctuations is described in detail and a comparison between the theoretical spectrum of log-amplitude fluctuations ( $\chi$ ) and the measured spectrum will show the validity of the underlying theories and assumptions of the acoustic scintillation method. At the end of this chapter, a time series of the

log-amplitude fluctuation variance ( $\sigma_\chi^2$ ) and effective refractive index parameter ( $C_{eff}^2$ ) are shown. In addition, the temperature standard deviation measured using the acoustic scintillation method is compared with that calculated from Jason's CTD data to test the accuracy of the acoustic scintillation measurement.

In Chapter 4, a time series of the plume's vertical velocity above Dante (a major hydrothermal edifice in MEF) is calculated and an estimate of the total heat flux is given. Tidal signals which are observed in the vertical flow measurements are highlighted in this chapter and error induced by the skewness of the mooring system is quantified.

Chapter 5 discusses the interaction between the hydrothermal plume and horizontal cross flows within the axial valley. Characteristic mean flows and tidal oscillations are addressed based on previous current meter measurements (data courtesy of R. E. Thomson (Institute of Ocean Sciences, Sidney BC) ). An entrainment and tidal response hypothesis is posed to explain the tidal signals observed in the plume's vertical velocity and temperature fluctuations measured using the acoustic scintillation method.

In Chapter 6, an integral model, based on an entrainment velocity that is dependent on flows along and perpendicular the plume's axis, is established to examine the behavior of a hydrothermal plume under a significant horizontal cross-flow. The coincidence between the model results and real measurements supports the validity of a linear entrainment and tidal response hypothesis introduced in Chapter 5.

Chapter 7 discusses the back scattering of acoustic signals from the turbulent structures (using the measurements from forward scattering) and from suspending particles (using measured particle concentration densities) within the plume. Theoretical quantification of the back scattering cross section is given for both particles and turbulence to test which one is the dominant back scatterer within a hydrothermal plume.

Chapter 8 will summarize the significant findings of the research and suggest recommendations for future research.

## CHAPTER 2

### EXPERIMENTAL APPROACH

#### 2.1 SUMMARY OF ALL RESEARCH CRUISES

The data used in this thesis were collected during four cruises on the research vessel (RV) Atlantis. The dates and the deep submergence dives made during each cruise are summarized in Table 2.1.

During the cruise AT15-21, two dives were conducted using the remotely operated vehicle (ROV) Jason II to find a significant hydrothermal plume that is suitable for long-term monitoring using the acoustic scintillation system. Dante was chosen to be the proper vent to monitor because the plume emanating from it is strong and extensive. A vigorous high temperature vent was identified and experiments were focused on this vent and its surroundings (see Figure 2.1). The bottom bathymetry around Dante was mapped with Jason II using the SM2000 multi-beam sonar (see Figure 2.2). Note that, there is no data for the top of Dante's structure and its neighbors (shown as the white blank in the center of Figure 2.2) because Jason could not go over Dante's structure (roughly 25 m high) due to the limitation

Table 2.1: Cruises with the RV Atlantis using either the ROV Jason II or the HOV Alvin

Cruise	Dates	Dives					
AT15-21	Aug 3 - 20, 2007	J2-286 J2-287					
AT15-23	Sep 11 - 28, 2007	AL4348 AL4350					
AT15-34	Jul 4 - 23, 2008	AL4411	AL4414	AL4415	AL4416	AL4421	AL4422
AT15-36	Aug 18 - 7, 2008	AL4439 AL4441 AL4447 AL4452					

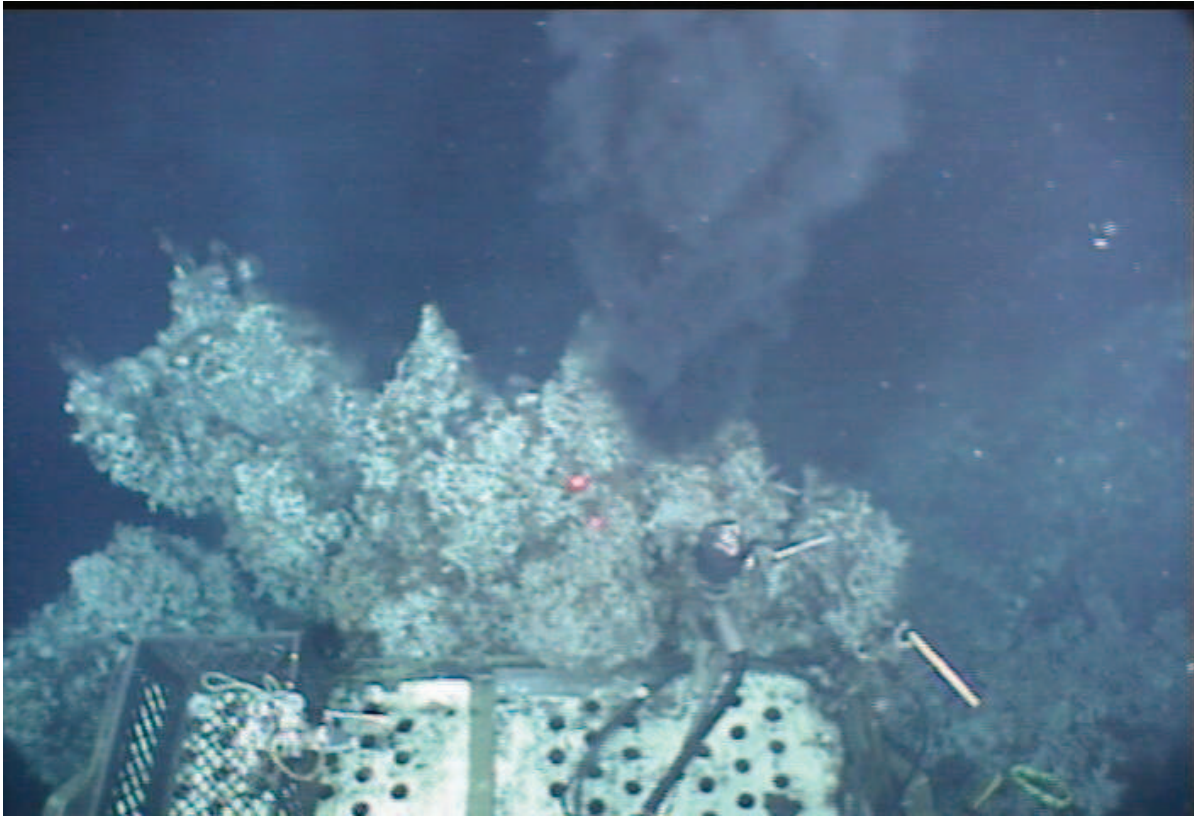


Figure 2.1: The vigorous hydrothermal vent on top of Dante on which the experiment is focused.

of the bottom tracking navigation system. The acoustic scintillation system (a transmitter TX and receiver RX mooring) was then deployed on the two flanks of Dante so that the acoustic line of sight was 20 m above Dante's structure. The horizontal distance between the transmitter and receiver was 91 m. The orientation of the transmitter/receiver line-of-sight was  $19^\circ\text{T}$  (along the Endeavour axis). In addition, vertical profiles of Dante's plume were imaged using an SM2000 multi-beam sonar to quantify the plume's characteristics at 20 m above the orifice (vertical expansion and diameter).

During the cruise AT15-23, the acoustic scintillation system deployed during the previous cruise was recovered and 24 hours of data was downloaded from it (battery failure

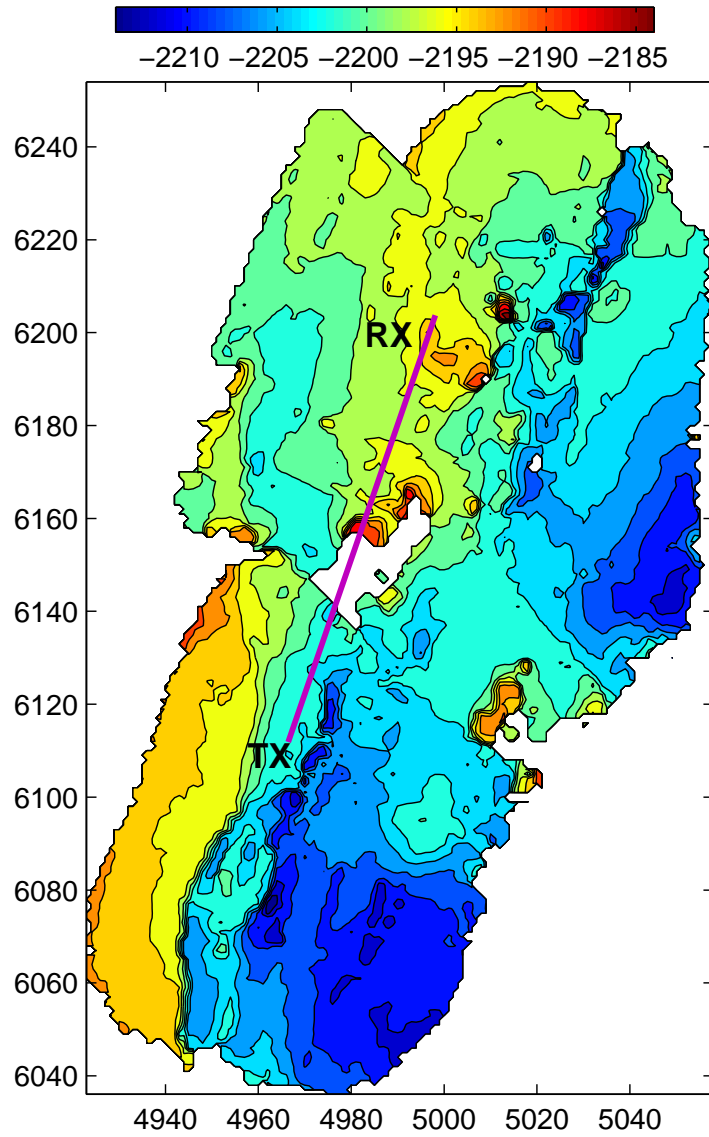


Figure 2.2: Bathymetry surrounding Dante and the placement of the acoustic scintillation transmitter (TX) and receiver (RX) array.

occurred and limited the amount of data collected). The acoustic scintillation system was then redeployed back to Dante at the previous mooring locations using the human occupied vehicle (HOV) Alvin of the Woods Hole Oceanographic Institution. Water samples of the plume produced by Dante at 20 m above were taken with Niskin bottles. From the ship, two conductivity, temperature and depth (CTD) towyo casts were conducted. The first CTD cast (AT1523001) transected from northeast to southwest along the Endeavour axis while the second one (AT1523002) transected from east to west across the Endeavour axis (see Figure 2.3).

During the cruise AT15-34, the acoustic scintillation system deployed during the previous cruise was recovered and 36 days of data was downloaded from it. The acoustic scintillation system was then redeployed back to its previous location. In addition, 4 CTD casts were conducted during this cruise. The first one (AT15-34-002) transected from east to west across the Endeavour axis near Hulk; the second one (AT15-34-003) transected from west to east across the Endeavour axis near Dante; the third one (AT15-34-004) transected from east to west across the Endeavour axis near Bastille; the last one (AT15-34-005) transected from southwest to northeast along the Endeavour axis (see Figure 2.4). During this cruise the exit velocity from hydrothermal vents on Hulk and Dante were also measured using a specialized flow meter developed by Dr L. Germanovich (Georgia institute of Technology). The analysis of these measurements are a separate study but an estimate of the exit velocity is used in this research. Hydrothermal vents from Hulk and Dante were sampled using Major water samplers operated by Alvin's robotic arms. The temperature of the plumes was also measured using Alvin's high temperature probe. Water samples at 20 m above Dante were also obtained with Niskin bottles.

During the cruise AT15-36, the acoustic scintillation system deployed previously at Dante was recovered. No data was logged because of a loose jumper cable located on one of the processing boards. The instrument was repaired and was then redeployed at Hulk for comparison purposes. The transmitter and receiver were anchored on the two flanks of Hulk at 20

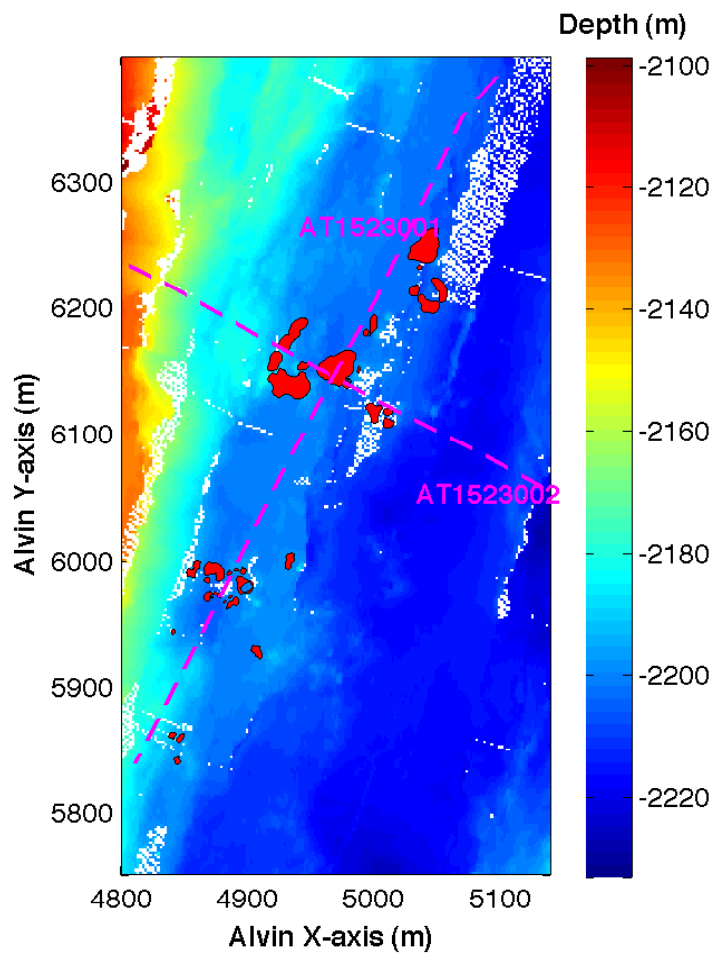


Figure 2.3: CTD transects during Cruise AT15-23 plotted in Alvin's UTM coordinates.

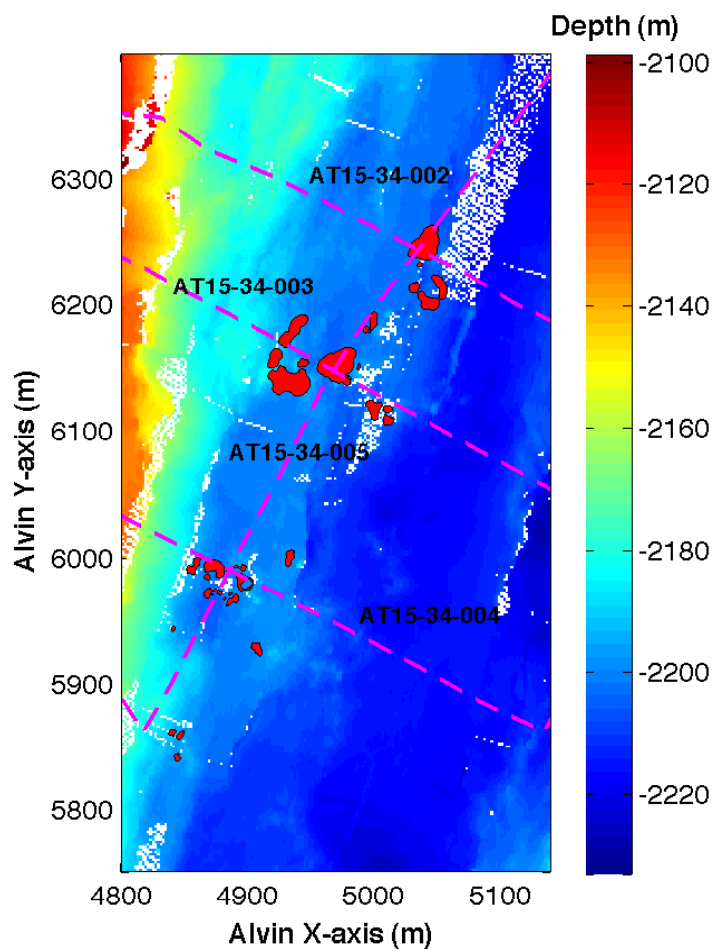


Figure 2.4: CTD transects during Cruise AT15-34 plotted in Alvin's UTM coordinates.

m above its sulfide structure in the same location as a previous deployment in 1991 (DiIorio et al., 2005). The transmitter/receiver line-of-sight was 107 m long and oriented  $37.8^{\circ}\text{T}$ . The system was recovered by the end of this cruise and 12 days of data was downloaded but are not analyzed as part of this thesis. In addition, water samples were taken from smokers at several major sulfide structures in MEF (Dante, Hulk and Grotto) at the orifice using Major water samplers and at 20 m above Dante and Hulk using Niskin bottles. Temperature at the orifices was measured using Alvin's high temperature probe and the exit velocities

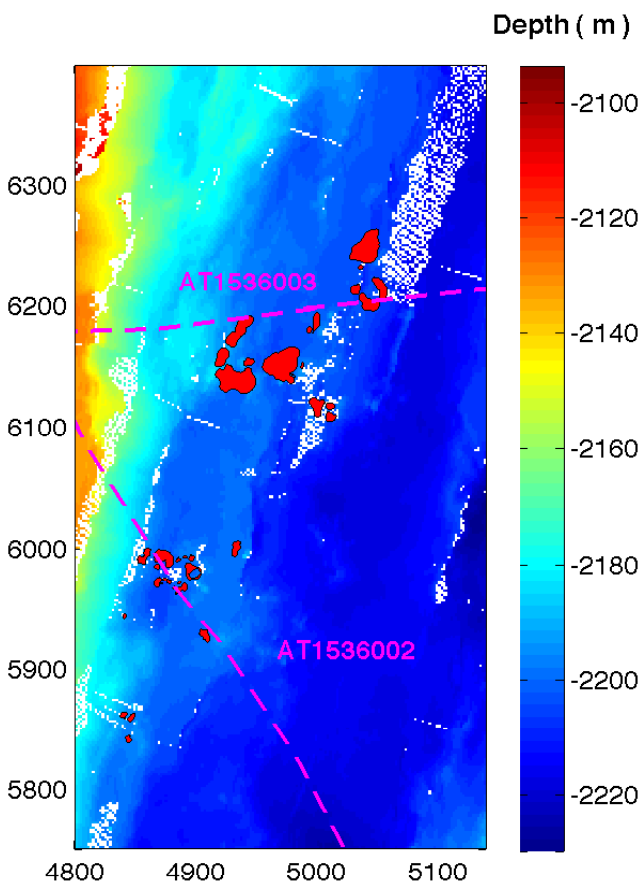


Figure 2.5: CTD transects during Cruise AT15-36 plotted in Alvin's UTM coordinates.

were gauged using the Germanovich flow meter. Three CTD casts were conducted during the cruise, two over the Main Endeavour field (AT1536002 and AT1536003; see Figure 2.5) and one background seawater vertical cast (AT1536001).

## 2.2 CTD RESULTS

The CTD tow-yos across and along the axial valley at the MEF are shown to demonstrate the spatial variability of the hydrothermal plumes in the ambient deep ocean environment. In order to calculate temperature anomalies from these tow-yos, a reference CTD cast was

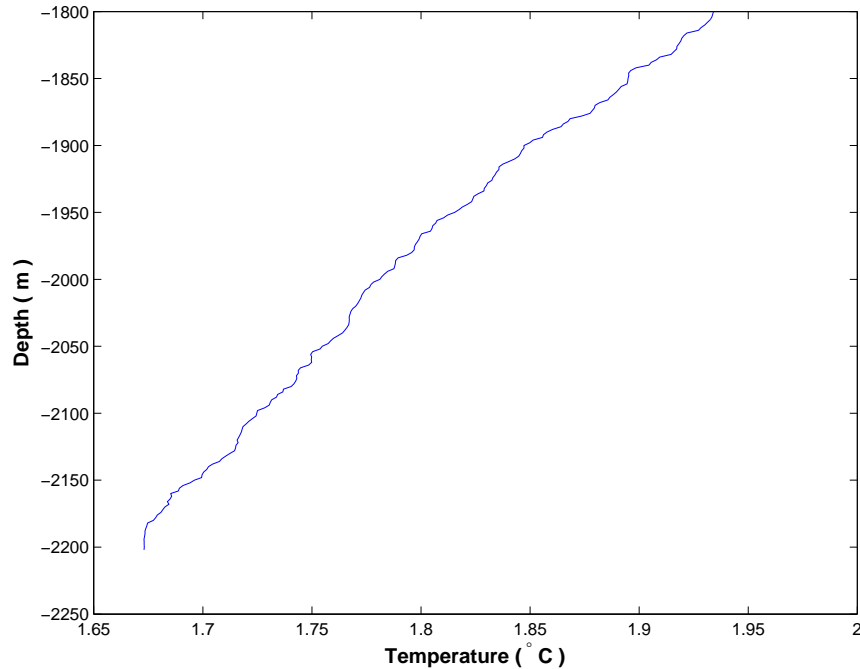


Figure 2.6: Background temperature measured from a CTD cast taken during AT1536001.

taken outside the axial valley and the profile of temperature from the ridge depth (1800 m) to the axial valley (2200 m) is plotted in Figure 2.6.

Figure 2.7 shows the transmissivity measured across the Endeavour valley in the vicinity of Dante during three CTD tows. Transmissivity reaches a minimum around 2000 m depth (200 m above the bottom) which defines the equilibrium level of the hydrothermal plume (where the plume stops rising and begins to spread laterally). Figure 2.8 shows the temperature anomalies ( $T - T_a$ ) measured across the Endeavour valley in the vicinity of Dante. The high temperature anomaly ( $> 0.1^\circ\text{C}$ ) indicates the existence of vigorous hydrothermal vents near that region.

The transmissivity and temperature anomaly measured along the axial valley during two CTD tows are shown in Figure 2.9 and Figure 2.10 respectively. As discussed, the low transmissivity observed at 2000 m depth along the axial valley confirms the height of the

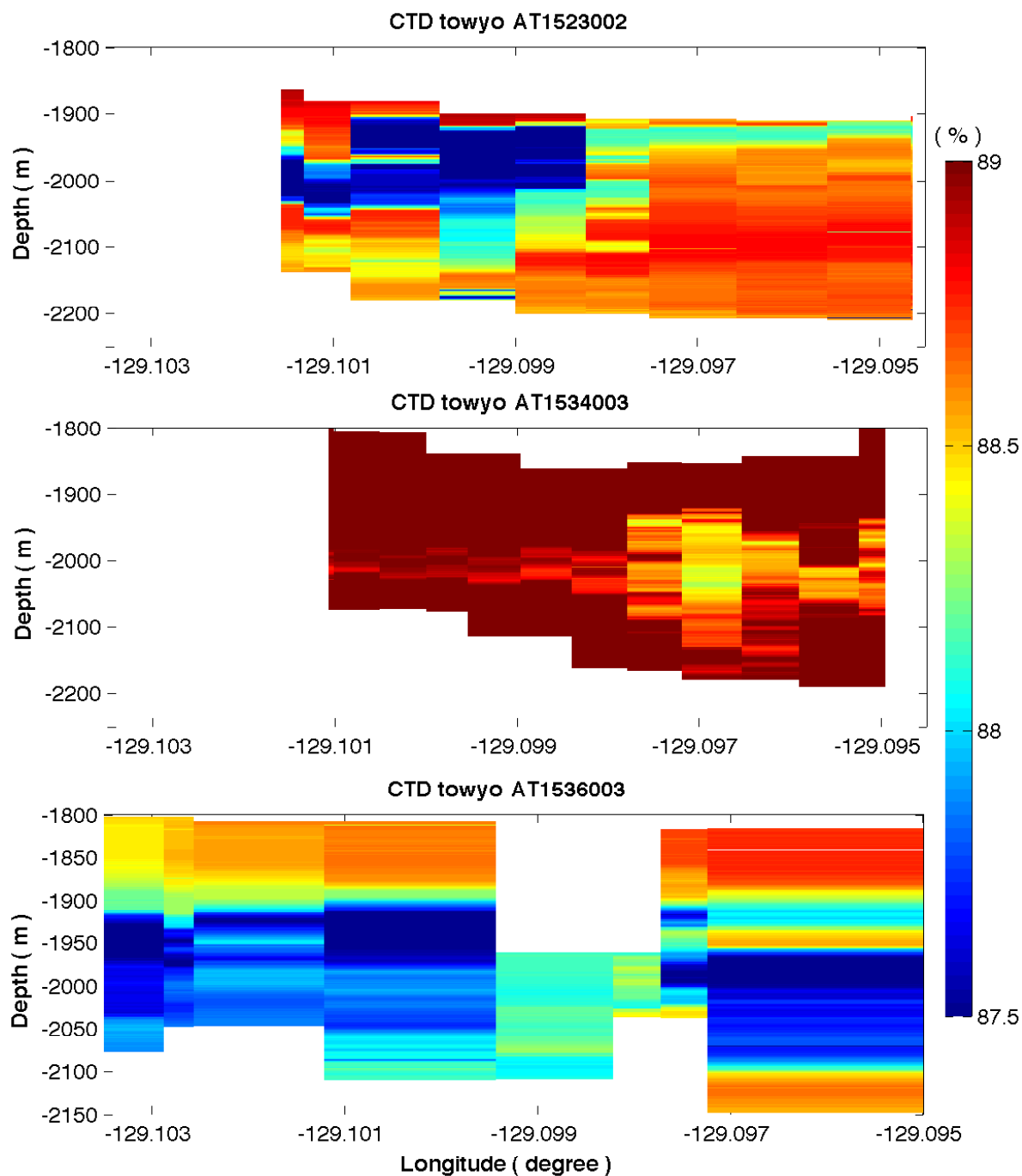


Figure 2.7: Transmissivity measured across Dante from CTD towyos during AT1523002, AT1534003 and AT1536003.

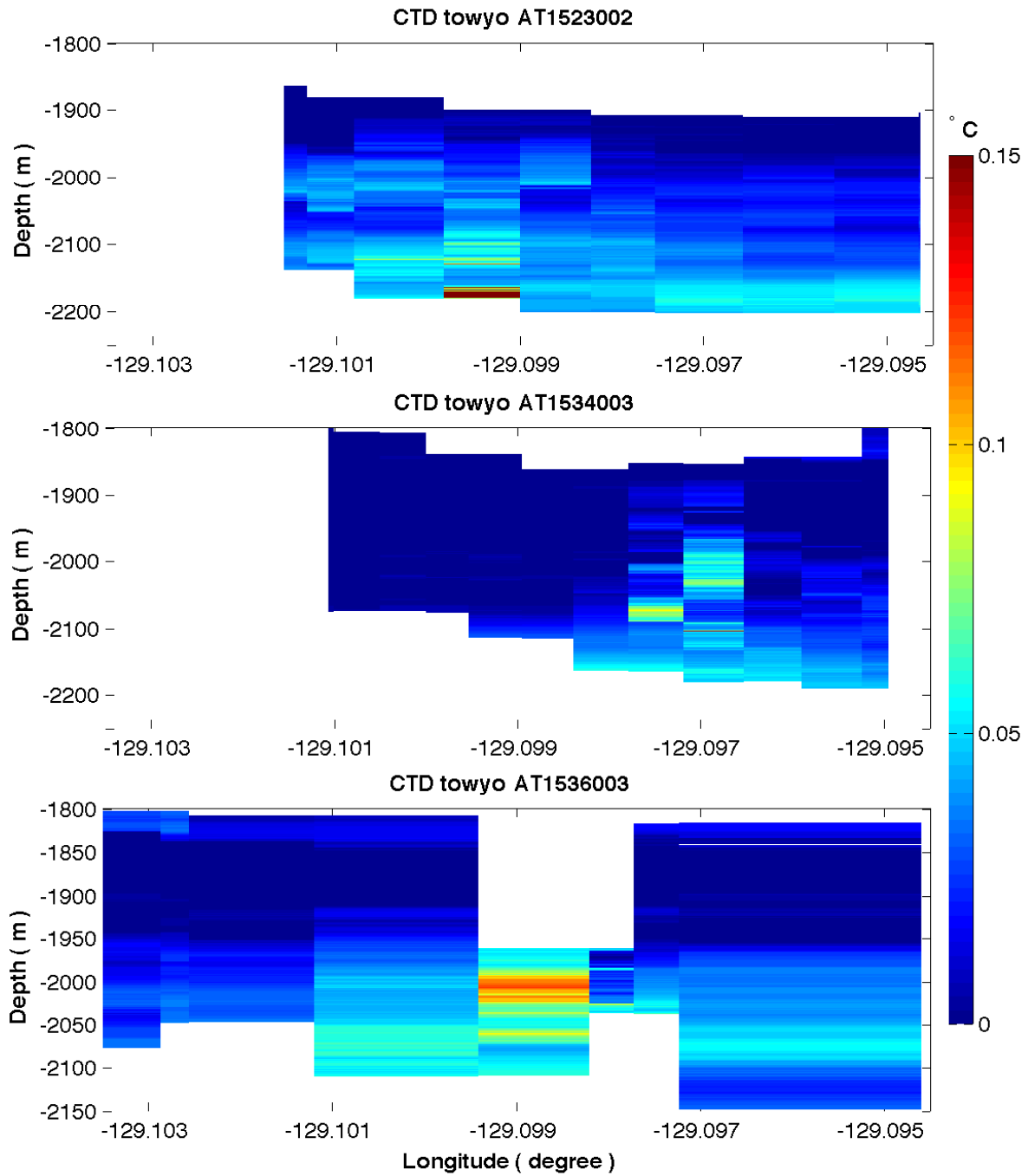


Figure 2.8: Temperature anomalies measured across Dante from CTD towyos during AT1523002, AT1534003 and AT1536003.

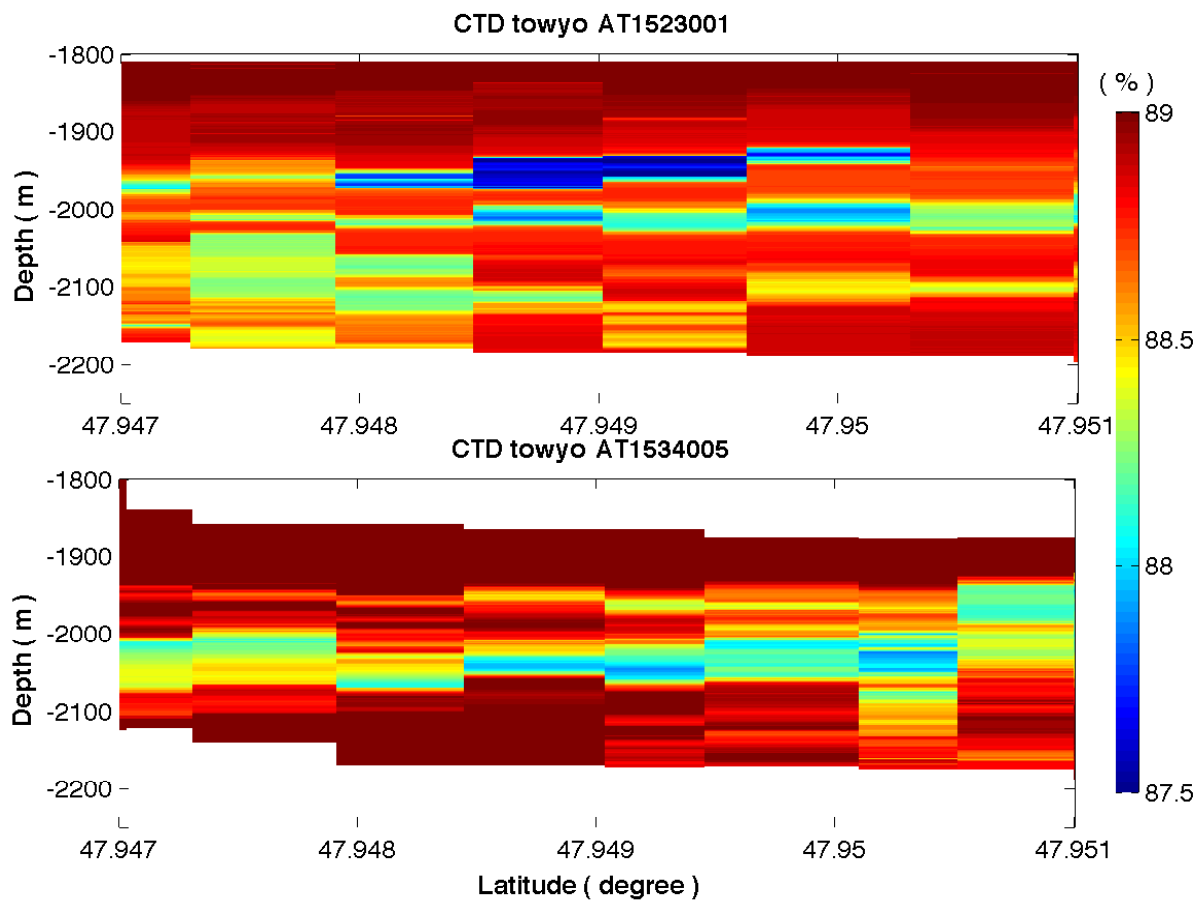


Figure 2.9: Transmissivity measured along the axial valley from CTD towys during AT1523001 and AT1534005.

equilibrium level of the hydrothermal plume. High temperature anomalies which indicate the existence of vigorous hydrothermal vents are observed at latitudes  $47.947^{\circ}\text{N}$  and  $47.949^{\circ}\text{N}$  (see the top panel in Figure 2.10) and  $47.9505^{\circ}\text{N}$  (see the bottom panel in Figure 2.10) which may correspond to the southern and northern vent fields respectively.

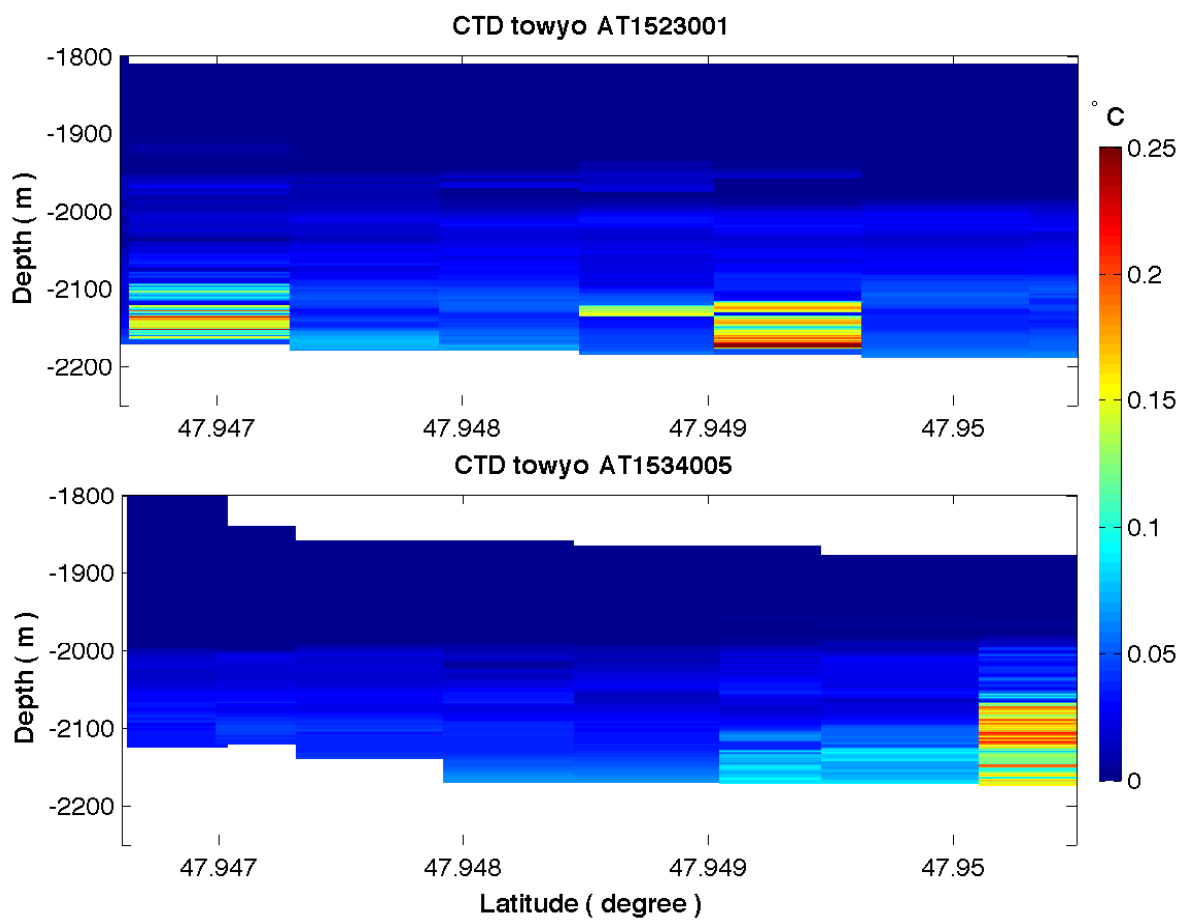


Figure 2.10: Temperature anomalies measured along the axial valley from CTD towyos during AT1523001 and AT1534005.

Table 2.2: Temperature Measurements on Dante

Vents	Dives	Dates (m/d/y)	Alvin Coordinates (x, y)	depth	Temperature (°C)
1	4422	7/20/08	4968.59, 6159.46	2185.28	328
2	4422	7/20/08	4957.43, 6158.01	2197.19	300
3	4422	7/20/08	4971.84, 6163.35	2181.63	333
4	4422	7/20/08	4970.93, 6162.41	2180.84	334
5	4422	7/20/08	4977.42, 6153.97	2179.48	310
6	4439	8/22/08	4972.55, 6162.27	2176.02	327.5
7	4439	8/22/08	4972.54, 6162.31	2176.11	327.5
8	4439	8/22/08	4940.28, 6150.86	2186.81	333
9	4441	8/24/08	4954.00, 6165.00	2185	328
10	4447	8/30/08	4986.00, 6166.00	2174	337.2
					$\bar{T} = 325.8^{\circ}\text{C}$

### 2.3 SAMPLING HYDROTHERMAL VENTS

Outflow temperatures from individual ‘black smokers’ were measured at the orifices during several Alvin dives (see Figure 2.11). Table 2.2 summarizes the temperature measurements conducted at approximately 10 high temperature focused vents on Dante. Temperature varies from 310 to 337 °C with an average of 325.8 °C. In addition to these instantaneous measurements, a Hobo high temperature probe was deployed in the orifice of the vigorous ‘black smoker’ on Dante (the one shown in Figure 2.1 and identified as vent 6 in Table 2.2) for a year to provide a long term time series of the vent’s temperature. The subsequent time series (see Figure 2.12) shows the temperature of the vent decreasing continuously from 331 °C to 321 °C, which implies that Dante may be cooling down through the year. However, the high magnitude of the temperature decrease (10 °C) is suspicious and has not been confirmed with other observations or with other investigations. The significant decrease could also be due to instrument drift or calibration issues with the Hobo probe over the deployment period of one year.

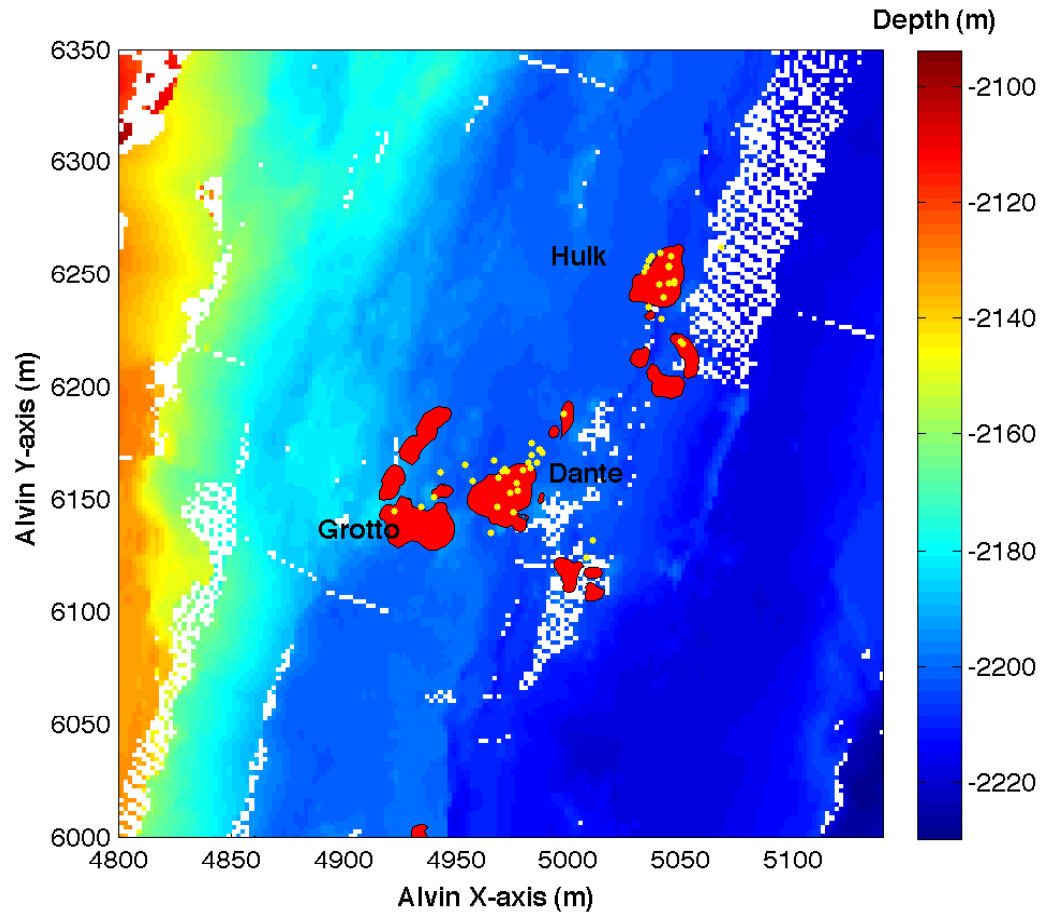


Figure 2.11: Sampling locations (yellow dots) plotted in Alvin's UTM coordinates.

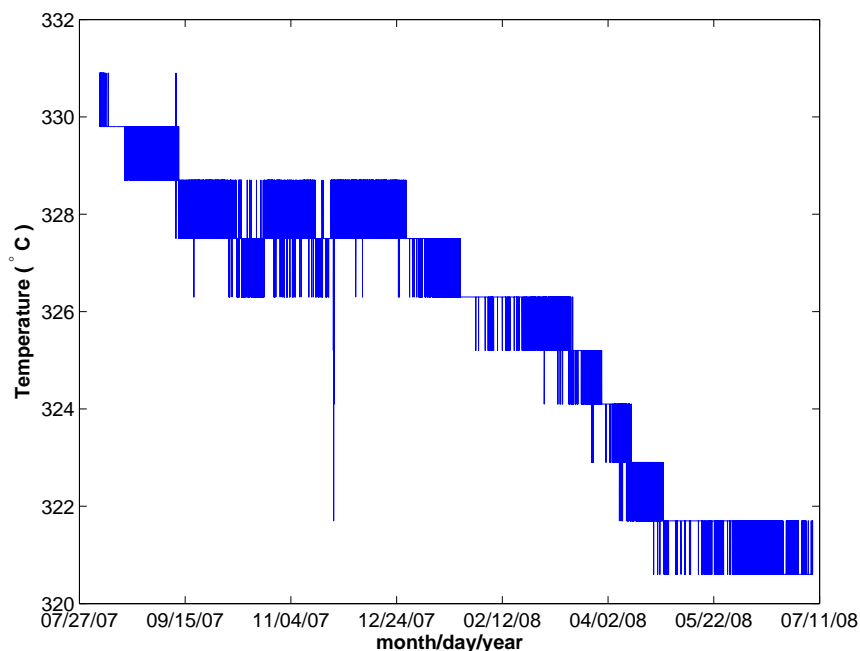


Figure 2.12: Temperature measured at a high temperature vent on Dante using a Hobo high temperature probe. The length of the time series is approximately one year with sampling interval of one hour. Note that, the comb-shape spikes in the time series are due to the Hobo probe's low resolution ( $1^{\circ}\text{C}$ ).

In addition to the temperature measurements, direct measurements of the concentration density of the suspending particles were made from the water samples collected from Dante and Hulk. Samples at approximately 6 inches above the orifice (where the fluid has turned black) were taken using the major samplers (see Figure 2.11 for locations). Samples at approximately 20 m above Dante were taken with Niskin water bottle samplers while Alvin was within the plume. All the samples were filtered with  $0.4\ \mu\text{m}$  membrane filter that was preweighed in an enclosed petri dish. The reference particle concentration density is also measured using water samples taken outside the axial valley. For this reference, the same particle size is used in order to obtain the particle number density. The results are summarized in Table 2.3 for both Dante and Hulk.

Table 2.3: Particle concentration and number density assuming a particle radius shown as  $a$ 

	N	Concentration (mg/ml)	particles/m <sup>3</sup> × 10 <sup>8</sup>	particles/m <sup>3</sup> × 10 <sup>4</sup>
			$a = 15 \mu\text{m}$	$a = 250 \mu\text{m}$
Dante orifices	12	0.0201 ± 0.0039	2.968 ± 0.572	6.404 ± 1.235
Dante at 20 m	14	0.0088 ± 0.0034	1.304 ± 0.505	2.814 ± 1.089
Hulk orifices	7	0.0188 ± 0.0055	2.776 ± 0.808	5.991 ± 1.745
Hulk at 20 m	11	0.0143 ± 0.0035	2.110 ± 0.509	4.555 ± 1.098
Reference	2	0.0017 ± 0.0006	0.246 ± 0.084	0.531 ± 0.180

## 2.4 ACOUSTIC SCINTILLATION SYSTEM

The self contained (battery operated and internally logging) acoustic scintillation system deployed during the cruises was developed by Dr. Di Iorio (University of Georgia) in collaboration with D. Lemon, R. Chave and M. Clarke (ASL Environmental Sciences) during the early 1990s. It was first used to investigate hydrothermal vent flow from Hulk within the Main Endeavour Field in 1991 (DiIorio et al., 2005). Since then, the receiver was completely rebuilt incorporating digital processing boards, increased memory and a faster central processing unit (CPU).

The transducers used are made of EC-97 piezoelectric ceramic which are horizontally omnidirectional and have a vertical beam width of 10 deg. The center frequency of the transducers is 307kHz with a bandwidth of 30kHz. Two transducers with a vertical separation of 15.5 cm make up the transmitter array. The receiver array consists of four transducers in the shape of a square. The transmitter and receiver configurations are shown in Figure 2.13. The two transmitters (T1 and T2) and four receivers (R1, R2, R3 and R5) make two pairs of parallel acoustic paths (channels (1,7) and (3,10); see Table 2.4). In addition, four different diverging paths can be created using channel pairs (1,2), (3,5), (6,7), and (8,10). Figure 2.14 shows the deployment configuration and Figure 2.2 shows the locations of the transmitter (TX) and receiver (RX) relative to Dante. The location and depth of the transmitter and

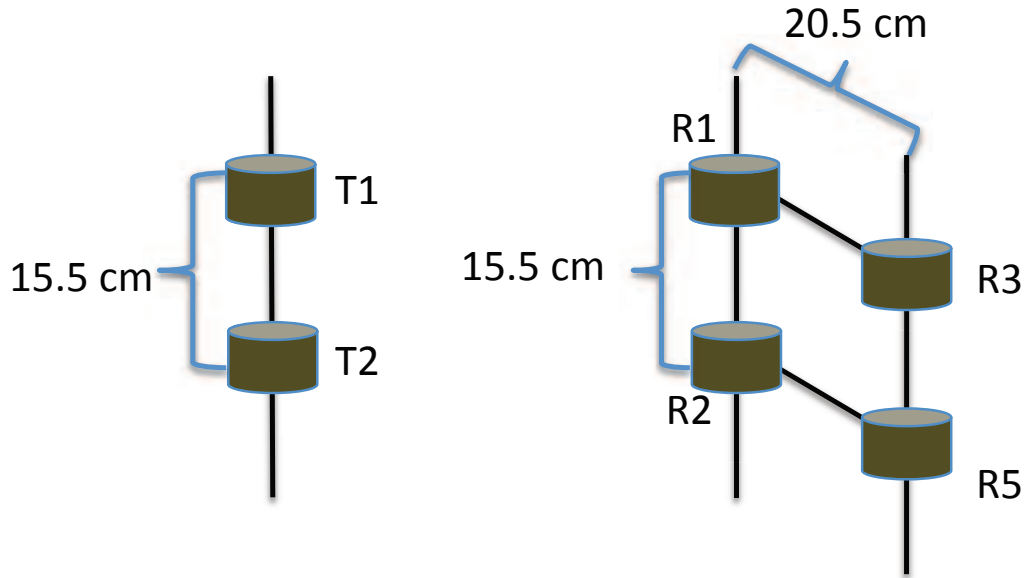


Figure 2.13: Configuration of the transducers showing vertical and horizontal separations.

Table 2.4: Channel identification for various transmitter and receiver combinations.

Channel	Transmitter	Receiver	Channel	Transmitter	Receiver
1	T1	R1	6	T2	R1
2	T1	R2	7	T2	R2
3	T1	R3	8	T2	R3
5	T1	R5	10	T2	R5

receiver mooring for the deployments at Dante and Hulk are summarized in Table 2.5. Figure 2.15 shows a photograph of the transmitter array as it is deployed off the ship.

The transmitter uses a pulsed monochromatic sinusoidal signal with a central frequency of 307200 Hz and a pulse width of 0.1 ms. The pulses are separated by 100 ms giving a pulse repetition rate of 10 Hz. The delay between the signals from the two transmitters is 25 ms (see Figure 2.16). The parameters of the system for 2007 and 2008 deployments are generalized in Table 2.6. In order to obtain a long term time series, the instrument was

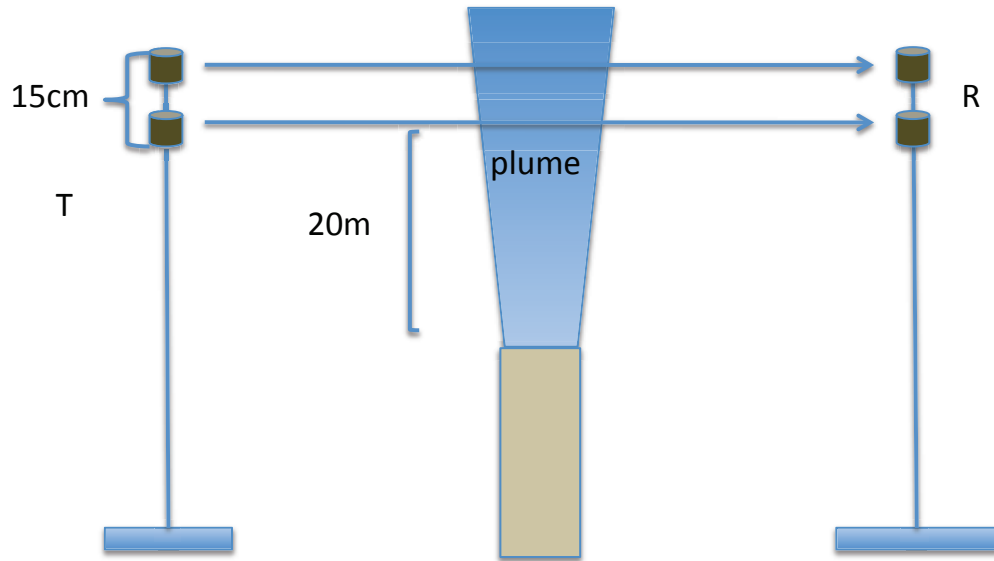


Figure 2.14: Configuration of the transmitter and receiver arrays relative to the hydrothermal plume.

Table 2.5: Location (Alvin coordinates) and depth of the transmitter and receiver deployments.

	Sulfide structure	X-axis (m)	Y-axis (m)	depth (m)
Transmitter	Dante	4979	6124	2202
Receiver	Dante	4998	6205	2204
Transmitter	Hulk	5063.3	6285.5	2210
Receiver	Hulk	4997	6200	2195



Figure 2.15: Photo showing the deployment of the Transmitter mooring from the RV Atlantis (photo courtesy of D. DiIorio).

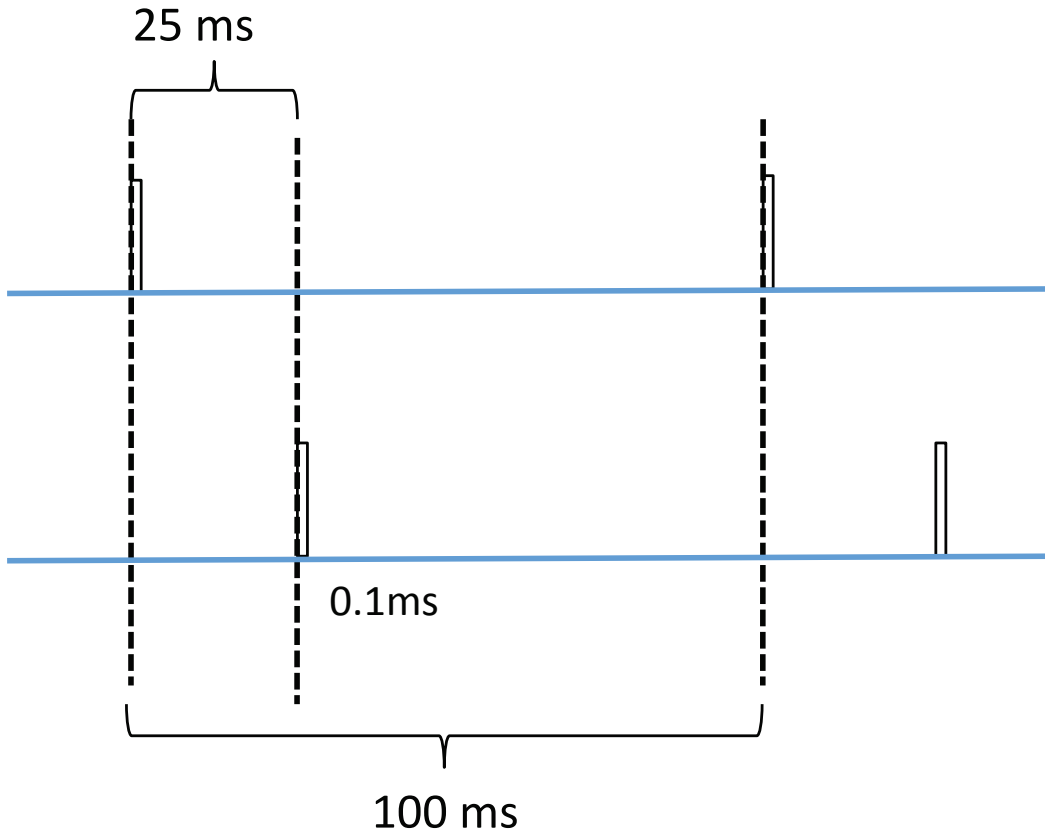


Figure 2.16: Configuration of the transmitted signal.

programmed for burst sampling with 15 min/hour (2007 on Dante) or 30 min/hour (2008 on Hulk) on the hour.

The in-phase (I) and quadrature (Q) components are obtained by sampling the received signal 1/4 carrier cycle apart every two cycles (150 kHz digitization rate) (DiIorio et al., 2005). The amplitude of the received pulse as a function of travel time is then calculated as  $A = \sqrt{I^2 + Q^2}$ . A window of 64 samples (0.43 ms) is used to capture the digitized pulses at a rate of 10 Hz (see Figure 2.17). The maximum amplitude above a noise threshold within each receiver window is detected and saved into the receiver's memory along with two adjacent samples on both sides of the maximum. In this way, each data ping contains

Table 2.6: Parameters of the acoustic scintillation system

Parameter	Quantity
Carrier frequency	307 kHz
Digitization rate	150 kHz
Recording interval	15 min h <sup>-1</sup> (2007) 30 min h <sup>-1</sup> (2008)
Transmission rate	10 Hz
Pulse width	0.1 ms
Signal delay	25 ms
Pulse separation	100 ms
Pathlength, orientation	91 m, 19°T (2007) 107 m, 37.8°T (2008)
Transducer separation	0.155 m

5 consecutive amplitude samples (as a function of travel time) with the maximum in the middle. A quadratic fit is then performed to pinpoint the amplitude ( $A_\tau$ ) as a function of arrival time ( $\tau$ ) of the received signal. A despiking routine was then developed in order to eliminate abrupt amplitude changes which may result from system noise or lost tracking of the received signal (see Figure 2.18). The log-amplitude fluctuation  $\chi$  is then calculated from the despiked amplitudes as  $\chi = \ln(A_\tau/\langle A_\tau \rangle)$  where  $\langle A_\tau \rangle$  is the mean amplitude averaged over 15 minutes of data (9000 data pings).

## 2.5 SM2000 MULTI-BEAM SONAR

Vertical profiles of the plume produced by Dante, was imaged with an SM2000 multi-beam sonar, manufactured by Kongsberg Mesotech Ltd., mounted in down looking mode on the ROV Jason (see Figure 2.19 for a schematic of the setup). During the experiment, Jason maintained its position within the plume above Dante (see Figure 2.20). The parameters of the sonar configuration are listed in Table 2.7. There is a circular sensor array consisting of 80 transducers inside the sonar, with a radius of 0.2 m, which form 128 separate beams of data after beam-forming is performed on the acoustic signal received by the sensor array.

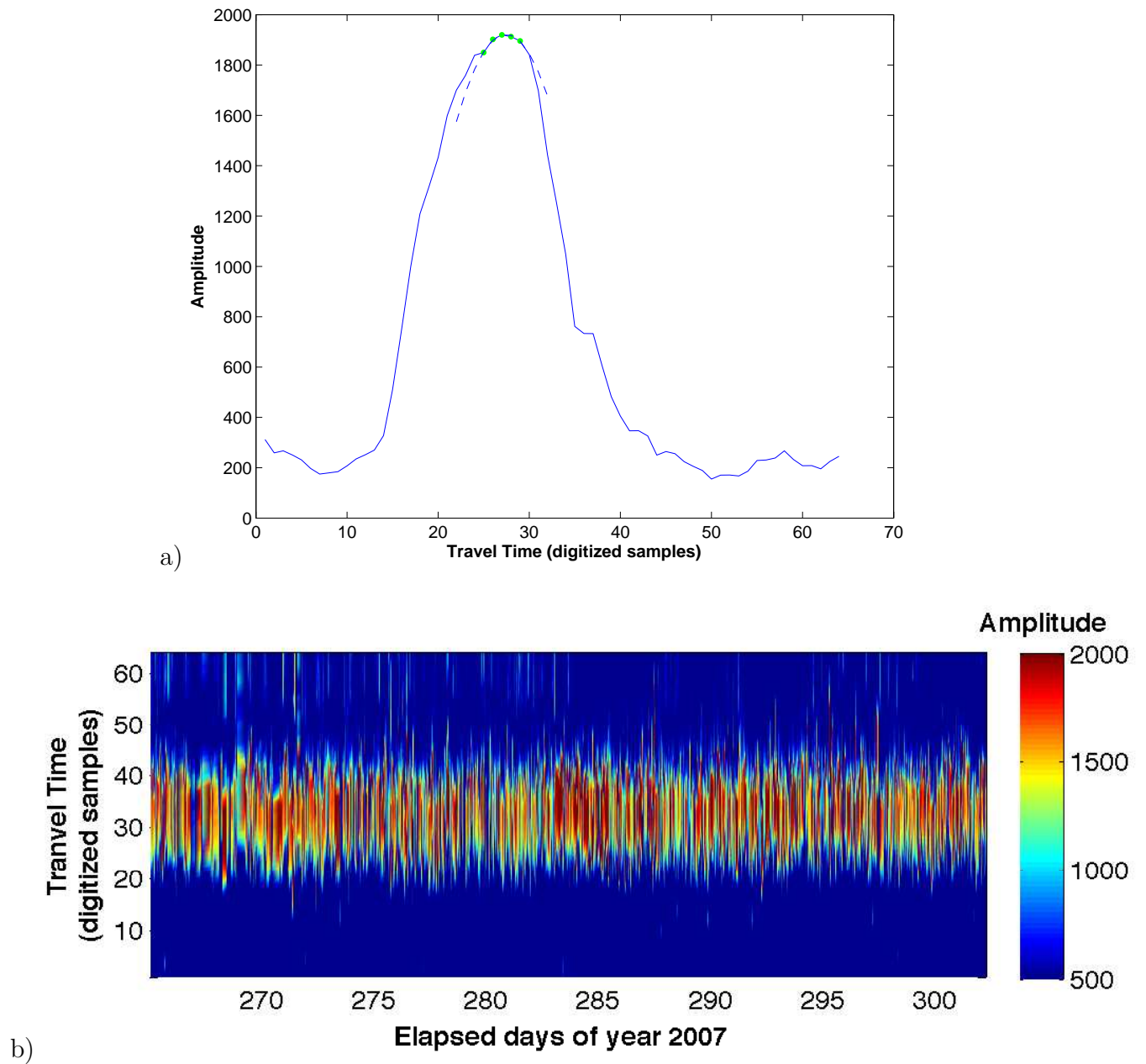


Figure 2.17: (a) Digitized amplitude captured by one sampling window where the green dots are the five points over which the quadratic fit is performed (dotted line). (b) Time series of the digitized amplitude as a function of travel time captured by the sampling window from Channel 1.

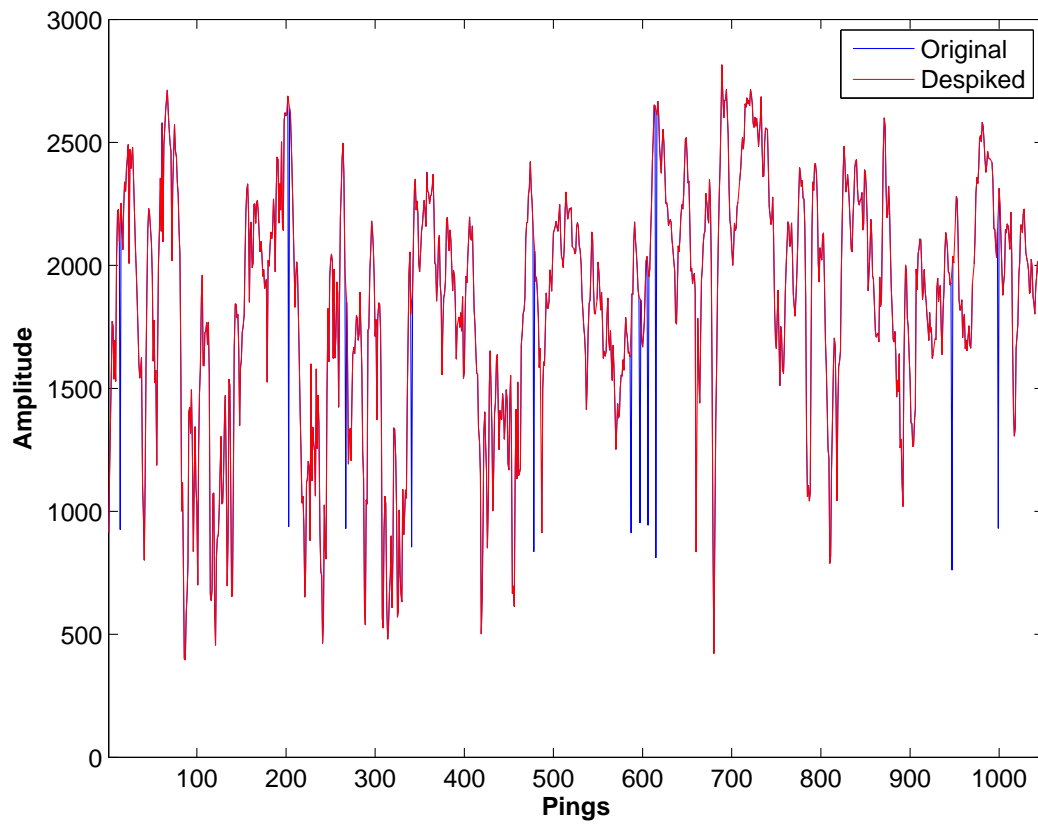


Figure 2.18: The original (blue) and despiked (red) amplitude time series of the received signal.

Table 2.7: Parameters of the SM2000 sonar system

Parameter	Quantity
number of elements	80
number of beams	128
frequency	20000 Hz
head radius	0.2 m
sound speed	1510 m/s
sample rate	19047 Hz
pulse width	75 $\mu s$
range meter	30 m

The acoustic frequency used by the sonar is 200 kHz while the digitization rate is 19047 Hz and the range of the detection is 30 m. Plumes produced by Dante can be visualized in the back-scattered images due to the reflection of the acoustic signals by the suspending particles and turbulent eddies within the plume.

Horizontal profiles of the plume from Dante were taken with Alvin using the SM2000 sonar in horizontal mode (see Figure 2.21) during cruises AT15-34 and AT15-36. The sonar parameters used were the same as listed in Table 2.7. Figure 2.22 shows the horizontal profile of the plume emanating from Dante imaged at 3 m above the sulfide structure.

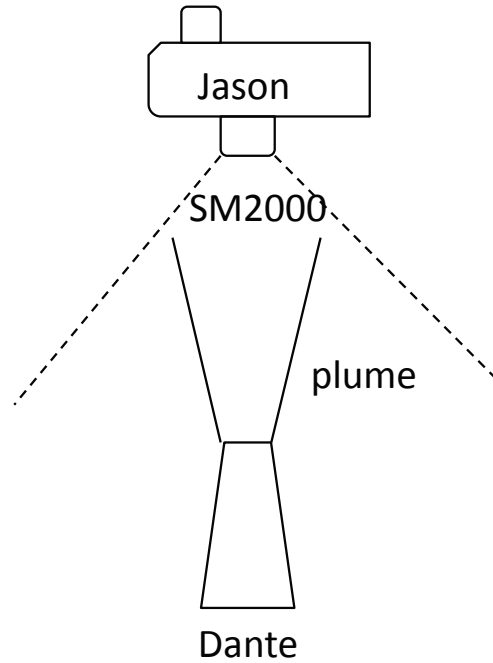


Figure 2.19: Vertical profiling with the SM2000 echosounder.

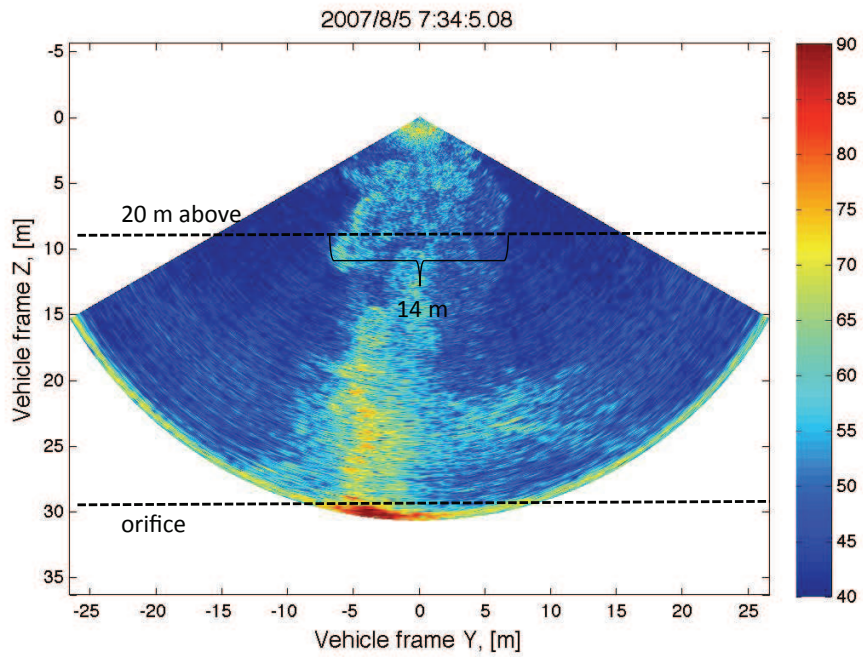


Figure 2.20: Back-scattered image of the plume from Dante.

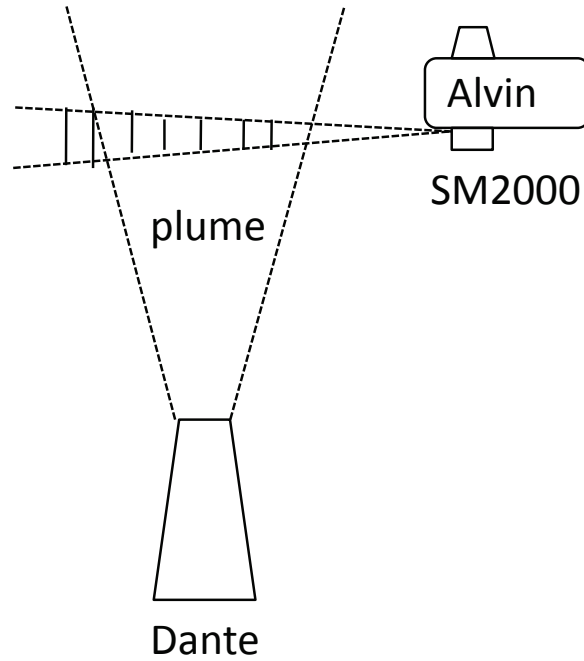


Figure 2.21: Horizontal mode of the SM2000 sonar.

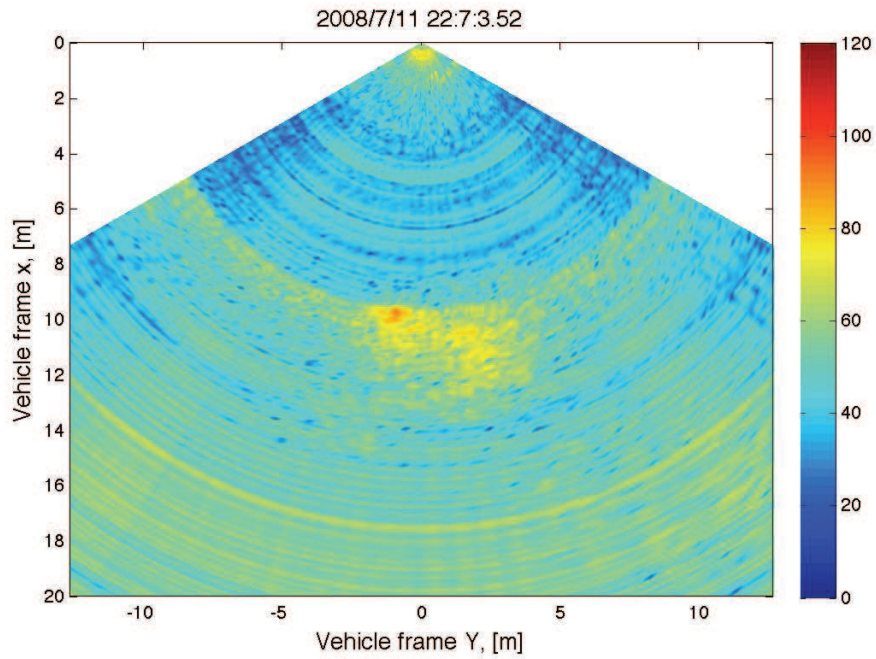


Figure 2.22: Horizontal profile of the plume 3m above Dante imaged by the SM2000 sonar.

## CHAPTER 3

### FORWARD SCATTERING FROM A HYDROTHERMAL PLUME

#### 3.1 THEORETICAL ESTIMATION FROM SUSPENDING PARTICLES

The underlying rationale for the scintillation method is based on the theory of wave propagation through a random medium generalized by Tatarskii (1961) and Ishimaru (1978a). In this theory, the medium is considered to be continuously filled with turbulent eddies. Turbulence of effective refractive index ( $n_{eff}$ ) is due to the fluctuation of current velocity and other passive properties like temperature and salinity. Suspending particles within the medium is assumed to be absent in this theory. However, the application of this theory to hydrothermal plumes remains dubious because hydrothermal plumes are a unique medium having both turbulence and suspending particles. Both could impose a major impact on the acoustic signal through scattering and absorption.

High temperature hydrothermal plumes are considered to be acidic, metal rich and reducing. As a result of entrainment, the plume mixes with the cold, alkaline and oxidizing seawater as soon as it leaves the orifice. Dissolved elements (i.e. metal sulfides and sulfates) within the plume precipitate out to form a suspension of particles which make the plume ‘black’. These suspending sulfide particles include pyrrhotite, pyrite, sphalerite and chalcopyrite (Feely et al., 1987, 1990). Direct measurements of the mass density of the suspending particles are made based on water samples retrieved from the plume on top of Dante (see Table 2.3).

The goal of this section is to quantify the effect of the particles on acoustic wave propagation, which in practice is to quantify their contribution to the variance of the log-amplitude

fluctuations ( $\sigma_\chi^2$ ) of the received signal. The theory used to quantify the effect of the suspending particles is generalized in Ishimaru (1978b) and Rytov et al. (1989), for which the single scattering approximation and Rayleigh scattering theory are applied. Based on the single scattering approximation (first Born approximation), the sound field at the receiver can be written as

$$u(\mathbf{r}) = \langle u(\mathbf{r}) \rangle + u_f, \quad (3.1)$$

where  $\langle u(\mathbf{r}) \rangle$  is the coherent sound field for the direct line of sight path connecting the transmitter and receiver, and  $u_f$  is the scattered field induced by the particles. Owing to the single scattering approximation,  $u_f$  can be regarded as the sum of the acoustic waves scattered once by the suspending particles (see Figure 3.1) while higher orders of scattering are omitted (waves scattered more than once before they reach the receiver).

In addition, acoustic waves are also attenuated because part of the energy (which is proportional to  $u^2$ ) is lost due to the scattering and absorption of suspending particles (denoted by  $\gamma$ ). Thus the sound field can be written as,

$$u(\mathbf{r}) = u_0 \exp(-\gamma/2), \quad (3.2)$$

where

$$\gamma = \int_{-D/2}^{D/2} \sigma_t \rho_n dr \quad (3.3)$$

and represents the attenuation caused by the particles lying in the part of the transmitter/receiver line-of-sight occupied by the plume with diameter  $D$  at the level of acoustic signal propagation,  $\sigma_t$  is the total scattering cross-section of an individual particle and  $\rho_n$  is the number concentration density (number of particles per unit volume). The single scattering approximation relies on the assumption that the amplitude of the coherent field  $\langle u(\mathbf{r}) \rangle$  is essentially constant within the scattering volume which will be the case if the particle concentration density  $\rho_n$  is small enough and if  $\gamma \ll 1$ . In such a case, waves scattered from different particles can be considered incoherent from each other.

The investigation of a hydrothermal plume using acoustic scintillation can be schematized as a spherical wave incident upon a cloud of suspending particles confined in a cylindrical volume (plume) located in the middle of the transmitter/receiver line-of-sight (see Figure 3.2). The distance between the transmitter and receiver is  $\sim 100$  m. The radius of the plume is taken as 7 m based on the back-scattered sonar images shown in Figure 2.20. The top and bottom of the cylinder are set to be 5 m above and below the acoustic line-of-sight due to the directivity of the transmitter and receiver (approximately  $10^\circ$  vertical beamwidth).

For an incident spherical wave, the coherent sound field can be written as

$$\langle u(\mathbf{r}) \rangle = \frac{A_0}{|\mathbf{r} - \mathbf{r}_0|} \exp(ik|\mathbf{r} - \mathbf{r}_0| - \gamma/2). \quad (3.4)$$

where  $r$  and  $r_0$  are the locations for the receiver and transmitter respectively and  $A_0$  is the amplitude of the incident wave. Based on the single scattering approximation, the sound wave scattered from a single particle can be written as

$$u_{fi}(\mathbf{r}) = A_0 f(\mathbf{i}, \mathbf{o}) \frac{\exp[ik(|\mathbf{r}' - \mathbf{r}_0| + |\mathbf{r} - \mathbf{r}'|) - \gamma_i/2 - \gamma_o/2]}{|\mathbf{r} - \mathbf{r}'||\mathbf{r}' - \mathbf{r}_0|}, \quad (3.5)$$

where  $\mathbf{r}'$  is the location of a single particle while  $\gamma_o = \int_{r'}^{r_o} \rho_n \sigma_t dr$  and  $\gamma_i = \int_{r_i}^{r'} \rho_n \sigma_t dr$  represent the attenuation of the sound waves scattered from (subscript o) and incident upon (subscript i) the particle respectively. The scattering amplitude of the  $i$ th particle  $f(\mathbf{i}, \mathbf{o})$  is a representation of the amplitude, phase, and polarization of the scattered wave in the far field in the direction  $\mathbf{o}$  when the particle is illuminated by an incident wave propagating in the direction  $\mathbf{i}$  (Ishimaru, 1978b). In general it is a complex function and can be written as

$$f(\mathbf{i}, \mathbf{o}) = |f(\mathbf{i}, \mathbf{o})| \exp(i\beta') \quad (3.6)$$

where  $\beta'$  is the phase shift caused by scattering from a particle at location  $r'$ . The scattered sound field is then a summation of all the scattered waves from each of the particles within the volume and thus can be written as

$$u_f(\mathbf{r}) = \sum_{r'} A_0 |f(\mathbf{i}, \mathbf{o})| \frac{\exp[ik(|\mathbf{r}' - \mathbf{r}_0| + |\mathbf{r} - \mathbf{r}'|) + i\beta' - \gamma_i/2 - \gamma_o/2]}{|\mathbf{r} - \mathbf{r}'||\mathbf{r}' - \mathbf{r}_0|}. \quad (3.7)$$

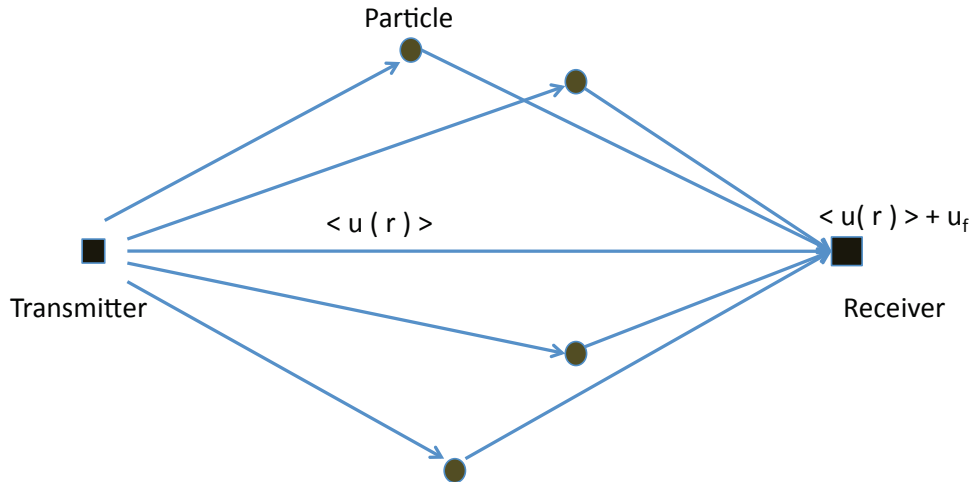


Figure 3.1: Single scattering approximation where  $\langle u(r) \rangle$  is the coherent line of sight path and  $u_f$  is the single scattering of the acoustic field.

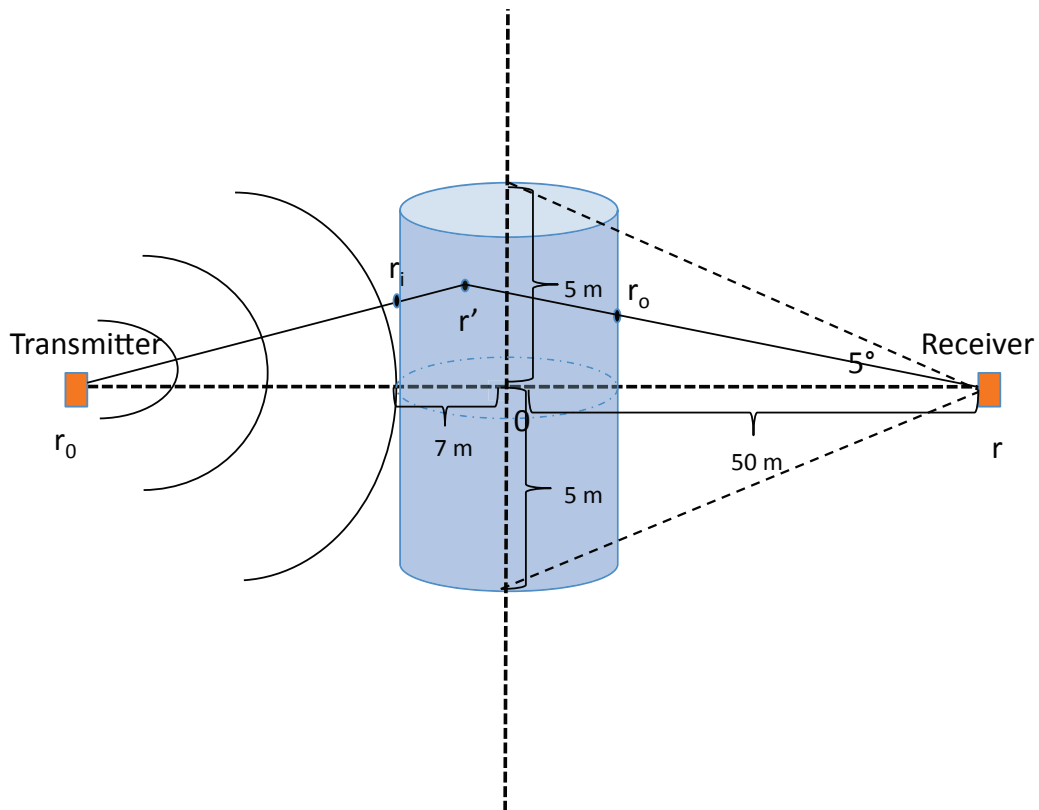


Figure 3.2: Particle scattering from a hydrothermal plume, in which  $\mathbf{r}_0/\mathbf{r}$  is the location of the transmitter/receiver,  $\mathbf{r}'$  is the location of a single particle within the plume and  $\mathbf{r}_i/\mathbf{r}_o$  is the location of the intercept between the line connecting the transmitter/receiver to the particle and the boundary of the plume.

In addition to the single scattering approximation, we implement Rytov's method of smooth perturbations to obtain a solution to the log-amplitude variance of the received signal caused by the suspending particles. Based on the Rytov solution, the sound field can be written as

$$u(\mathbf{r}) = A \exp(iS) = \exp(\Phi), \quad (3.8)$$

where  $\Phi$  is a 'complex phase' representing the fluctuations of both amplitude and phase of the received signal.  $\Phi$  can be expanded into a series:

$$\Phi = \Phi_0 + \sum \Phi_i, \quad (3.9)$$

where  $\Phi_0$  is the complex phase for the coherent field which can be written as

$$\langle u(\mathbf{r}) \rangle = \exp(\Phi_0) \quad (3.10)$$

and  $\sum \Phi_i = \Phi_1 + \Phi_2 + \Phi_3 + \dots$  is a series of the scattered sound field in which  $\Phi_1$  is the single scattering term and  $\Phi_i$  ( $i \geq 2$ ) represents multiple scattering effects. Given the smooth perturbation assumption ( $\Phi_1 \gg \Phi_i$  ( $i \geq 2$ )) then the multiple scattering terms are neglected in equation (3.9). Thus

$$\begin{aligned} \Phi_1 &= \Phi - \Phi_0 = \ln A + iS - (\ln A_0 + iS_0) \\ &= \ln(A/A_0) + i(S - S_0) \\ &= \chi + i\phi, \end{aligned} \quad (3.11)$$

in which  $\chi = \ln(A/A_0)$  is the log-amplitude fluctuation and  $\phi = S - S_0$  is the phase fluctuation. Therefore the sound field becomes

$$u(\mathbf{r}) = \exp(\Phi_0 + \Phi_1) = \langle u(\mathbf{r}) \rangle \exp(\Phi_1), \quad (3.12)$$

Expanding the exponent into a Taylor series gives,

$$u(\mathbf{r}) = \langle u(\mathbf{r}) \rangle (1 + \Phi_1 + \frac{\Phi_1^2}{2} + \dots). \quad (3.13)$$

Taking the first two terms of the series is then,

$$u(\mathbf{r}) = \langle u(\mathbf{r}) \rangle (1 + \Phi_1). \quad (3.14)$$

Comparing equation (3.14) and (3.1) leads to the relation:

$$\Phi_1 = \frac{u_f}{\langle u \rangle}, \quad (3.15)$$

which is the solution for  $\Phi_1$  based on the single scattering approximation. Substituting equation (3.15) into equation (3.12) gives the representation of the sound field assuming a Rytov solution and the single scattering approximation:

$$u(\mathbf{r}) = \langle u(\mathbf{r}) \rangle \exp\left(\frac{u_f}{\langle u \rangle}\right). \quad (3.16)$$

Inserting equation (3.4) and equation (3.7) into equation (3.15) gives

$$\Phi_1(\mathbf{r}) = |\mathbf{r} - \mathbf{r}_0| \sum_{r'} |f(\mathbf{i}, \mathbf{o})| \frac{\exp[ik(|\mathbf{r} - \mathbf{r}'| + |\mathbf{r}' - \mathbf{r}_0| - |\mathbf{r} - \mathbf{r}_0|) + i\beta' - \gamma_o/2 - \gamma_i/2 + \gamma/2]}{|\mathbf{r} - \mathbf{r}'||\mathbf{r}' - \mathbf{r}_0|} \quad (3.17)$$

and the complex conjugate is,

$$\Phi_1^*(\mathbf{r}) = |\mathbf{r} - \mathbf{r}_0| \sum_{r'} |f(\mathbf{i}, \mathbf{o})| \frac{\exp[-ik(|\mathbf{r} - \mathbf{r}'| + |\mathbf{r}' - \mathbf{r}_0| - |\mathbf{r} - \mathbf{r}_0|) - i\beta' - \gamma_o/2 - \gamma_i/2 + \gamma/2]}{|\mathbf{r} - \mathbf{r}'||\mathbf{r}' - \mathbf{r}_0|}. \quad (3.18)$$

Thus the log-amplitude fluctuation of the received signal is

$$\begin{aligned} \chi = \text{Re}(\Phi_1) &= \frac{\Phi_1 + \Phi_1^*}{2} \\ &= \frac{1}{2} |\mathbf{r} - \mathbf{r}_0| \sum_{r'} \left\{ \frac{|f(\mathbf{i}, \mathbf{o})| \exp[ik(|\mathbf{r} - \mathbf{r}'| + |\mathbf{r}' - \mathbf{r}_0| - |\mathbf{r} - \mathbf{r}_0|) + i\beta' - \gamma_o/2 - \gamma_i/2 + \gamma/2]}{|\mathbf{r} - \mathbf{r}'||\mathbf{r}' - \mathbf{r}_0|} \right. \\ &\quad \left. + \frac{|f(\mathbf{i}, \mathbf{o})| \exp[-ik(|\mathbf{r} - \mathbf{r}'| + |\mathbf{r}' - \mathbf{r}_0| - |\mathbf{r} - \mathbf{r}_0|) - i\beta' - \gamma_o/2 - \gamma_i/2 + \gamma/2]}{|\mathbf{r} - \mathbf{r}'||\mathbf{r}' - \mathbf{r}_0|} \right\}. \end{aligned} \quad (3.19)$$

According to the single scattering approximation, the wave scattered from different particles are assumed to be incoherent from each other. This assumption is supported by Palmer (2009) who found that the coherent component is less than 1% of the incoherent component

within the back scattering intensity from a hydrothermal plume. Thus, the variance of the log-amplitude fluctuation can be written as

$$\begin{aligned}\sigma_\chi^2 &= \langle \chi(\mathbf{r})\chi^*(\mathbf{r}) \rangle = \frac{1}{4}|\mathbf{r} - \mathbf{r}_0|^2 \int_{V'} \langle |f(\mathbf{i}, \mathbf{o})|^2 \rangle \exp(-\gamma_o - \gamma_i + \gamma) \times \\ &\frac{\{\exp[i2k(|\mathbf{r} - \mathbf{r}'| + |\mathbf{r}' - \mathbf{r}_0| - |\mathbf{r} - \mathbf{r}_0|)] + \exp[-i2k(|\mathbf{r} - \mathbf{r}'| + |\mathbf{r}' - \mathbf{r}_0| - |\mathbf{r} - \mathbf{r}_0|)] + 2\}}{|\mathbf{r} - \mathbf{r}'|^2 |\mathbf{r}' - \mathbf{r}_0|^2} \rho_n dV' \\ &= \frac{1}{2}|\mathbf{r} - \mathbf{r}_0|^2 \int_{V'} \langle |f(\mathbf{i}, \mathbf{o})|^2 \rangle \exp(-\gamma_o - \gamma_i + \gamma) \times \\ &\frac{\{\cos[2k(|\mathbf{r} - \mathbf{r}'| + |\mathbf{r}' - \mathbf{r}_0| - |\mathbf{r} - \mathbf{r}_0|)] + 1\}}{|\mathbf{r} - \mathbf{r}'|^2 |\mathbf{r}' - \mathbf{r}_0|^2} \rho_n dV'.\end{aligned}\quad (3.20)$$

where  $\rho_n$  is the constant particle concentration density and it is assumed that particles are distributed uniformly within the volume. The  $\langle \rangle$  denote averaging over all the particles in space. Note that an integral is implemented instead of the summation because the particles are assumed to be distributed continuously within the plume with the number concentration density  $\rho_n$ , therefore  $\rho_n dV'$  gives the number of the particles enclosed by an infinitesimal volume  $dV'$ .

In deriving equation (3.20), the imaginary part of the scattering amplitude  $f(\mathbf{i}, \mathbf{o})$  is omitted. This is true in the case of far field Rayleigh scattering theory which is applied when  $\lambda \gg a$  and  $kR \gg 1 \gg ka$  (Medwin and Clay, 1998) in which  $\lambda$  is the wave-length,  $a$  is the particle's grain size and  $R = |\mathbf{r} - \mathbf{r}'|$  is the distance from the particle to the receiver. According to Feely et al. (1987) and Feely et al. (1990), the grain size of the 'black-smoker' particles from active vents on the Endeavour segment ranges from less than  $10 \mu\text{m}$  to slightly larger than  $500 \mu\text{m}$ . The wave-length used in the acoustic scintillation measurement is  $\lambda = 4834 \mu\text{m}$  which is much larger than the upper bound of the grain size distribution. In addition, the receiver is approximately 45 m away from the plume and thus  $kR = (2\pi/\lambda)R = 5.87 \times 10^4 \gg 1$  while  $ka = 0.326 < 1$  ( $a = 250 \mu\text{m}$ ). Therefore the far field Rayleigh scattering approximation is applicable. Since according to Palmer (1996), the scattered sound is insensitive to the shape of the scatterer for Rayleigh scattering and for the purpose of estimating the maximum contribution of the suspending particles to  $\sigma_\chi^2$ , all the particles within the plume are assumed to be rigid spheres.

According to Medwin and Clay (1998), the square of the scattering amplitude for a rigid sphere is

$$|f(\mathbf{i}, \mathbf{o})|^2 = \frac{(ka)^4}{9} \left(1 - \frac{3}{2} \cos \theta\right)^2 a^2, \quad (3.21)$$

in which  $a$  is the grain size of the particle, and  $k$  is the wave-number of the acoustic signal and  $\theta$  is the scattering angle ( $\theta = 0$  is forward scattering and  $\theta = \pm 180$  is back scattering) (see Figure 3.3). The total scattering cross-section can be written as

$$\sigma_t = \int_0^{2\pi} d\phi \int_0^\pi \sin \theta d\theta |f(\mathbf{i}, \mathbf{o})|^2 = \frac{7}{9} \pi k^4 a^6. \quad (3.22)$$

The particle number concentration density  $\rho_n$  can be calculated from the mass concentration density listed in Table 2.3. First, the average grain size of an individual particle is assumed to be  $a \sim 250 \mu\text{m}$  (the median in the range given by Feely et al. (1990)). Then the volume of a single particle is

$$V_p = \frac{4\pi}{3} a^3 = 6.54 \times 10^{-11} \text{ m}^3. \quad (3.23)$$

Note that in Rayleigh scattering theory the shape of the particles is not important but for an estimate of the particle number concentration we assume spherically shaped particles. Since the particles in the plume are mainly iron and copper sulfide, the average density of a single particle can be taken as that of iron sulfide:  $\rho_p \sim 4.8 \times 10^3 \text{ kg/m}^3$ . Then the mass of a single particle is

$$m_p = \rho_p V_p = 3.14 \times 10^{-7} \text{ kg}. \quad (3.24)$$

For the case of Dante, the maximum particle concentration density at 20 m above the orifice is  $\rho_m = 0.0088 + 0.0034 = 0.012 \text{ kg/m}^3$  (see Table 2.3). Then the number concentration density can be estimated as

$$\rho_n = \frac{\rho_m}{m_p} = 3.88 \times 10^4 \text{ particles/m}^3. \quad (3.25)$$

Recall that, the key assumption underlying the application of single scattering approximation is that the particle concentration density is small enough so that  $\gamma \ll 1$ . For

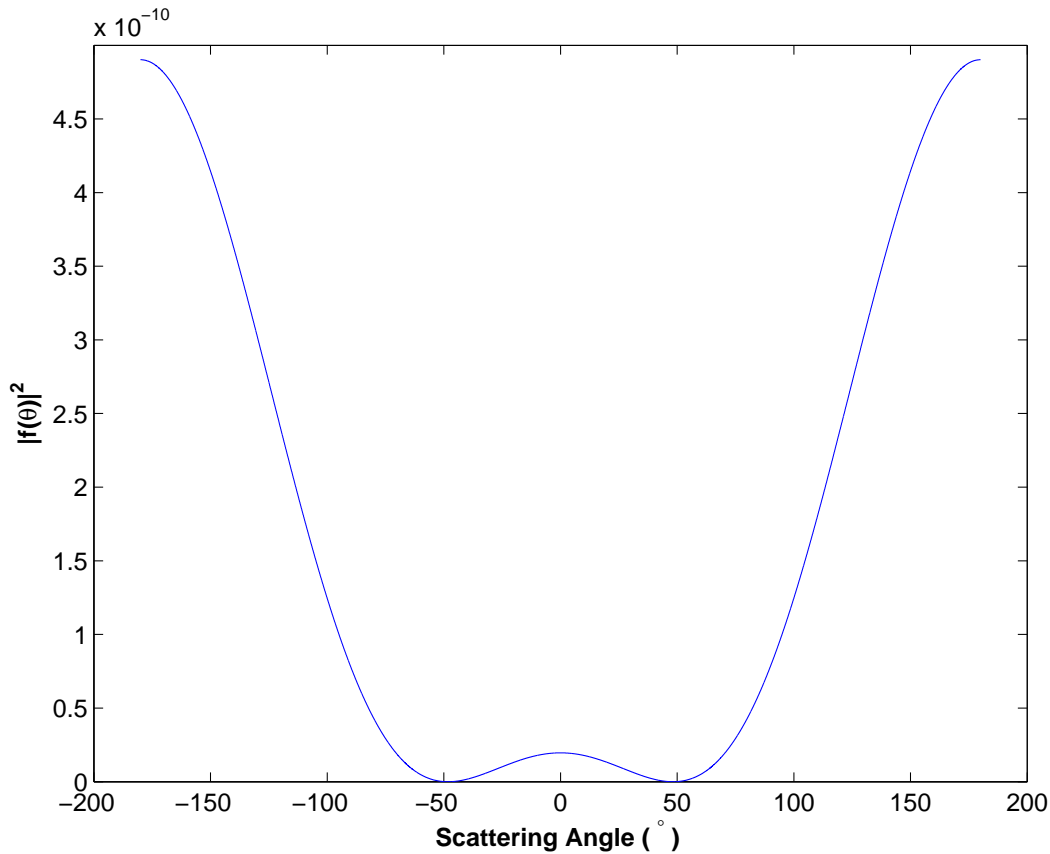


Figure 3.3: Square of the scattering amplitude  $|f(\mathbf{i}, \mathbf{o})|^2$  for a rigid sphere with  $a = 250\mu\text{m}$  ( $ka = 0.33$ ). Forward scattering is represented by  $\theta = 0^\circ$ .

the plume above Dante, substituting equation (3.22) into equation (3.3) and setting  $\rho_n = 3.88 \times 10^4$  particles/ $\text{m}^3$ ,  $a = 250 \mu\text{m}$ ,  $D = 14$  m and  $k = 1.30 \times 10^3$  rad/m gives

$$\begin{aligned}
 \gamma &= \int_{-D/2}^{D/2} \sigma_t \rho_n dr \\
 &= \frac{7}{9} \pi k^4 a^6 \rho_n D \\
 &= 9.26 \times 10^{-4} \ll 1,
 \end{aligned} \tag{3.26}$$

and thus the assumption is satisfied.

Substituting equation (3.21), equation (3.22) and  $\rho_n$  into equation (3.20) and calculating the integral numerically over the volume shown in Figure 3.2 gives  $\sigma_\chi^2 = 1.08 \times 10^{-6}$ , which

is much smaller than that measured by acoustic scintillation ( $\sigma_\chi^2 \sim 0.1$  as will be shown in Figure 3.6). This indicates the forward scattering from suspending particles within the plume has negligible effect on the fluctuation of the received signal and that turbulence may be the dominant scattering mechanism.

### 3.2 EFFECT OF TURBULENCE

According to Clifford (1971), Farmer et al. (1987), and DiIorio and Farmer (1994), the variance of the log-amplitude fluctuations ( $\sigma_\chi^2$ ) for wave propagation through a random medium assuming weak scattering and the Rytov method of smooth perturbations can be written as

$$\sigma_\chi^2 = 4\pi^2 k^2 \int_0^L dy \int_0^\infty d\kappa \kappa \Phi_n(\kappa) \sin^2 \left( \frac{\kappa^2 y(L-y)}{2kL} \right). \quad (3.27)$$

In this equation  $\Phi_n(\kappa)$  is the three dimensional spectral density for the effective refractive index fluctuations ( $n_{eff}$ ) caused by the perturbations of temperature and current velocity within the medium which are assumed to be isotropic and homogeneous in the plane perpendicular to the direction of acoustic propagation;  $\kappa$  is the magnitude of the two dimensional wave-number ( $\kappa = \sqrt{\kappa_x^2 + \kappa_z^2}$ ) in the plane  $y = \text{const}$ ;  $k = 2\pi f/c$  is the acoustic wave-number where  $f$  is the system frequency and  $c$  is the sound velocity;  $L$  is the length of the acoustic line-of-sight and  $y$  is the horizontal distance from the transmitter. The scale of sensitivity for amplitude fluctuations corresponds to the Fresnel scale  $\sqrt{\lambda L} = 0.7$  m located in the middle of the acoustic path. At this scale diffraction effects from the  $\sin^2$  term masks out the focusing potential of scales smaller than  $\sqrt{\lambda L}$ .

By virtue of the Kolmogorov spectrum for isotropic and homogeneous turbulence within the inertial subrange  $\ell_o \ll \sqrt{\lambda L} \ll L_o$  ( $L_o$  is the outer scale of the turbulence and  $\ell_o$  is the inner scale of the turbulence),

$$\Phi_n(\kappa) = 0.033 C_{eff}^2 \kappa^{-11/3}. \quad (3.28)$$

Due to the apparently different properties of the plume in comparison with the ambient ocean water,  $C_{eff}^2$  should be a spatially variable function of the path length  $y$ . Based on the results of laboratory experiments generalized by Papanicolaou and List (1988), the profile of the intensity of turbulence is a Gaussian distribution across a turbulent buoyant plume (turbulence intensity reaches maximum at the axis of the plume and attenuates exponentially toward its boundaries). Therefore, a Gaussian distribution is assumed to account for the variation of  $C_{eff}^2$  along the acoustic line-of-sight,

$$C_{eff}^2(y) = \tilde{C}_{eff}^2 \exp(-(y - L/2)^2/b_{eff}^2), \quad (3.29)$$

in which  $\tilde{C}_{eff}^2 = C_{eff}^2(y = L/2)$  is the value at the plume's axis and  $b_{eff}$  is the radius of the profile defined as the distance between the plume's axis and the point where  $C_{eff}^2$  attenuates to  $1/e$  of its axial value.

The radius of the plume can be estimated from the back-scattered images produced by the SM2000 sonar discussed in section 2.5. According to Figure 2.20, the radius of the plume emanating from Dante at 20 meter above the orifice ( $D/2$ ) is 7 m. According to Bemis et al. (2002) and Rona et al. (2002), the profile of the back-scattered intensity across the plume is of the same pattern as that of the particle concentration profile which also has a Gaussian distribution:

$$C_{particle}(r) = \tilde{C}_{particle} \exp(-(y - L/2)^2/b_{particle}^2), \quad (3.30)$$

where  $\tilde{C}_{particle}$  is the maximum concentration at the plume's axis and  $b_{particle}$  is the radius of the profile defined as the distance between the plume's axis and the point where the particle concentration decreases to  $1/e$  of its axial value. The radius measured in Figure 2.20 can be considered as the distance between the plume's axis and the point where the particle concentration decreases to its background level. Thus it is reasonable to assume  $D/2 \approx \sqrt{2}b_{particle}$ , which corresponds to the particle concentration at the edge of the plume as 13% of the center line value ( $C_{particle}(D/2) = 0.13\tilde{C}_{particle}$ ). By further assuming  $b_{particle} \approx b_{eff}$

(the profile of the particle concentration resembles that of  $C_{eff}^2$ ), one obtains

$$b_{eff} \approx \frac{D}{2\sqrt{2}} \approx 5 \text{ m.} \quad (3.31)$$

Inserting equation (3.31) and  $L = 91 \text{ m}$  (for 2007's deployment at Dante) into equation (3.29), one obtains

$$C_{eff}^2(y) = \tilde{C}_{eff}^2 \exp(-(y - 45.5)^2/25) \quad (3.32)$$

which is plotted in Figure 3.4. Substituting equation (3.32) into equation (3.28) gives

$$\Phi(\kappa, y) = 0.033 \tilde{C}_{eff}^2 \exp(-(y - L/2)^2/b_{eff}^2) \kappa^{-11/3}. \quad (3.33)$$

Inserting equation (3.33) into equation (3.27), one obtains

$$\sigma_\chi^2 = (0.033) 4\pi^2 k^2 \int_0^L dy \int_0^\infty d\kappa \kappa \tilde{C}_{eff}^2 \exp\left[-\left(\frac{y - L/2}{b_{eff}}\right)^2\right] \kappa^{-11/3} \sin^2\left(\frac{\kappa^2 y(L - y)}{2kL}\right). \quad (3.34)$$

Using the trigonometric identity  $\sin^2 \theta = \frac{1}{2}(1 - \cos 2\theta)$  and letting  $s = y/L$  and  $\gamma^2 = \frac{\kappa^2 L}{k}$ , equation 3.34 can be normalized as

$$\sigma_\chi^2 = (0.033) 2\pi^2 k^{7/6} L^{11/6} \tilde{C}_{eff}^2 \int_0^1 ds \int_0^\infty d\gamma \gamma^{-8/3} \exp\left[-\left(\frac{(s - 1/2)L}{b_{eff}}\right)^2\right] \times (1 - \cos(\gamma^2 s(1 - s))). \quad (3.35)$$

For the 2007 deployment at Dante, the constant parameters within the integrand are  $L = 91 \text{ m}$  and  $b_{eff} = 5 \text{ m}$ . The integral in equation (3.35) is calculated numerically ( $=0.026$ ) using the adaptive quadrature algorithm (Shampine, 2008) with the upper boundary of  $\gamma$  set as  $10^5$ . The log-amplitude variance is then quantified in terms of the center axis effective refractive index structure parameter,

$$\sigma_\chi^2 = 0.0169 L^{11/6} k^{7/6} \tilde{C}_{eff}^2. \quad (3.36)$$

A key assumption made here is that the turbulence with the scales of interest within the plume is adequately described by the Kolmogorov spectrum. The application of the

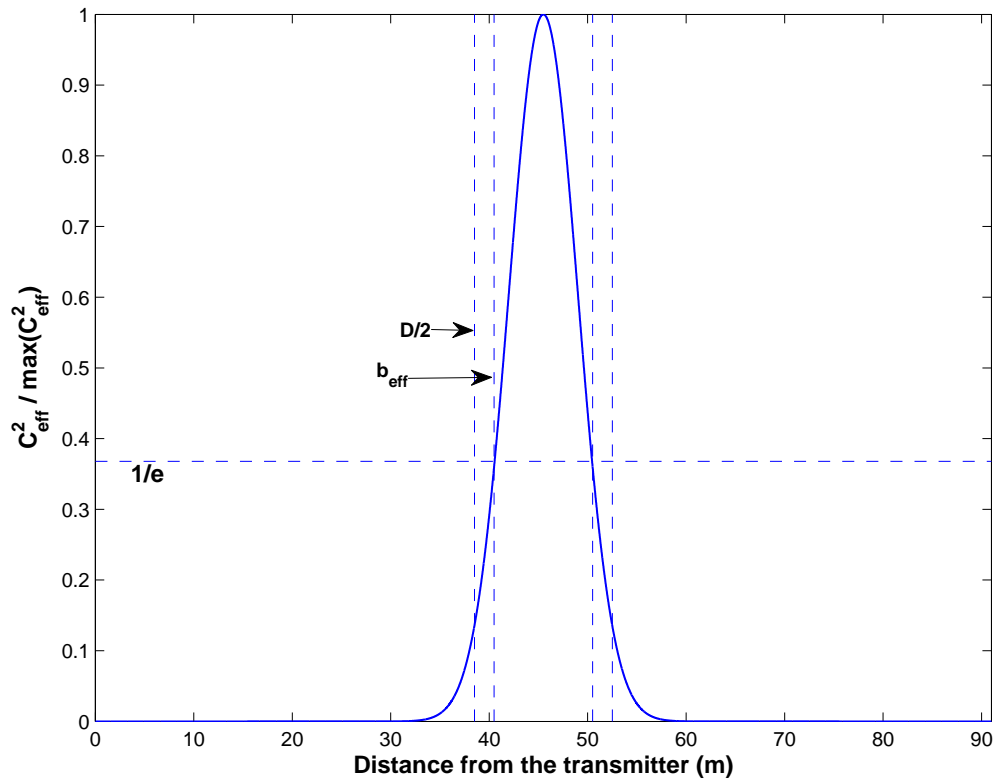


Figure 3.4: Variation of  $C_{eff}^2$  along the distance between transmitter and receiver.

Kolmogorov spectrum is shown to be valid by Wetzler et al. (1998) for temperature variability measured near the Pipe Organ vent field of Juan de Fuca Ridge. To test this assumption, we calculate the theoretical temporal power spectral density as given by DiIorio and Farmer (1994),

$$W_{\chi}(f) = 8\pi^2 k^2 \int_0^L dy \int_{\kappa > 2\pi f/W}^{\infty} \frac{d\kappa \kappa \Phi(\kappa, y)}{[(\kappa W)^2 - (2\pi f)^2]^{1/2}} \sin^2 \left( \frac{\kappa^2 y(L-y)}{2kL} \right), \quad (3.37)$$

which is modified for hydrothermal vent flow and path weighting on the turbulence. Within equation (3.37),  $W$  is the vertical velocity of the plume and  $\Phi(\kappa, y)$  is given by equation (3.33). Setting  $s = y/L$ ,  $\gamma^2 = (\kappa W/2\pi f)^2 - 1$  and  $f_0 = W/\sqrt{\lambda L}$  the integral in equation

(3.37) can be written as

$$\frac{fW_\chi(f)}{\sigma_\chi^2} = \frac{0.033(2\pi)^{1/6}2}{0.0169}(f/f_0)^{-5/3} \int_0^1 ds \int_{\gamma>0}^\infty \frac{d\gamma}{(\gamma^2 + 1)^{11/6}} \exp \left[ - \left( \frac{(s - 1/2)L}{b_{eff}} \right)^2 \right] \times \sin^2 \left[ \pi \left( \frac{f}{f_0} \right)^2 (\gamma^2 + 1)s(1 - s) \right], \quad (3.38)$$

in which  $\frac{fW_\chi(f)}{\sigma_\chi^2}$  is the normalized variance-preserved temporal power spectral density.

Figure 3.5 shows a comparison of the spectrum numerically calculated from equation (3.38) with that measured from the received signal. The range of the scales of turbulence presented by the spectrum is from 14 m to 3 cm. Such a range is taken based on the assumption that the largest turbulence within the plume is of the order the plume's diameter ( $\sim 14$  m at 20 m above the orifice according to the SM2000 image in Figure 2.20) and the smallest scale that can be resolved by the acoustic instrument that contributes to the effective refractive index fluctuation ( $n_{eff}$ ) is  $\sim 3$  cm. According to Figure 3.5, the calculated spectrum is a good fit to the measured spectrum (the deviation at the highest frequencies is due to noise) which suggests the validity of applying the Kolmogorov spectrum.

By measuring  $\sigma_\chi^2$  of the received signal,  $\tilde{C}_{eff}^2$  can be calculated from equation (3.36) (see Figure 3.6). A tidal oscillating pattern is observed in the  $\tilde{C}_{eff}^2$  result and will be discussed in detail in Chapter 5 and 6. The radially averaged value can then be calculated as

$$\begin{aligned} \langle C_{eff}^2 \rangle &= \frac{1}{\sqrt{2}b_{eff}} \int_{L/2}^{L/2+\sqrt{2}b_{eff}} \tilde{C}_{eff}^2 \exp(-(y - L/2)^2/b_{eff}^2) dy \\ &= 0.5981\tilde{C}_{eff}^2, \end{aligned} \quad (3.39)$$

for comparison to CTD data measured within the plume at random locations.

Generally speaking, the effective refractive index fluctuation ( $n_{eff}$ ) are caused by perturbations in both the velocity field and scalar properties (i.e. temperature) within the medium. According to (DiIorio and Farmer, 1998),  $C_{eff}^2$  can be separated into two parts:

$$C_{eff}^2 = C_{\eta_s}^2 + \frac{11}{6}C_{\eta_v}^2, \quad (3.40)$$

where  $C_{\eta_s}^2$  characterizes the level of the refractive index fluctuations from scalars (temperature, salinity and dissolved component concentration) and  $C_{\eta_v}^2 = C_v^2/c_0^2$  characterizes

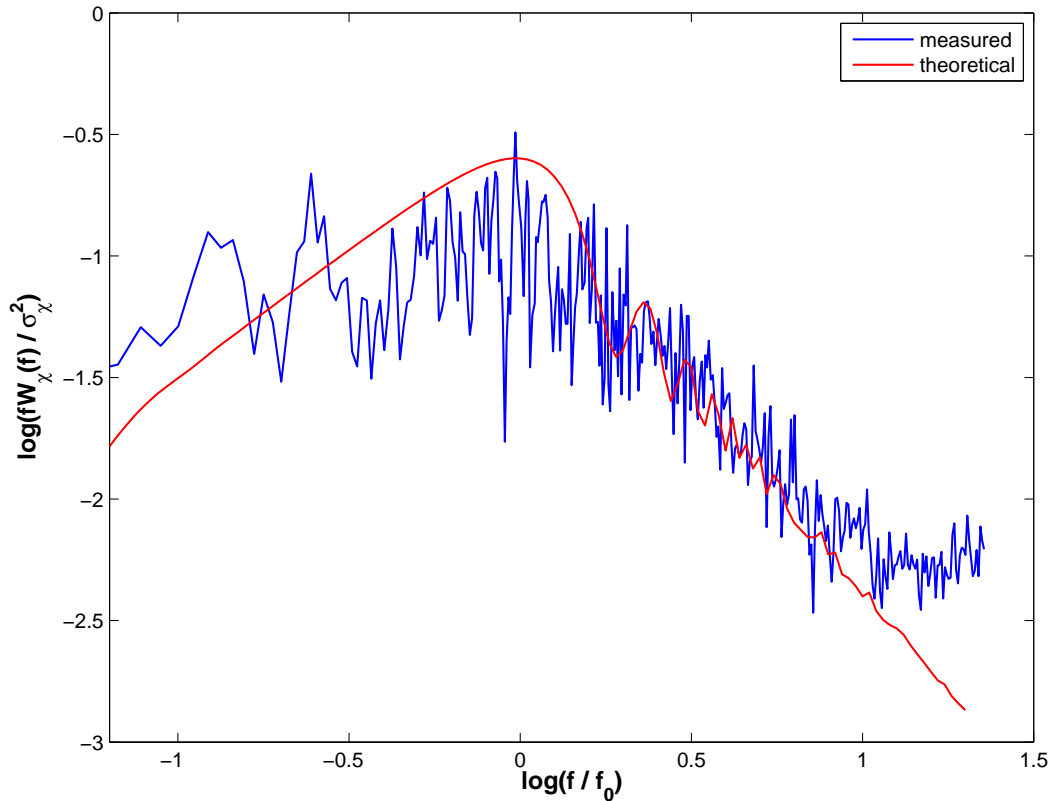


Figure 3.5: Normalized log-amplitude spectrum from measured data (blue) versus the theoretically calculated spectrum (red).

the contribution from the velocity field ( $C_v$  is the structure parameter for the turbulent velocity and  $c_0 \approx 1480$  m/s is the sound velocity in a quiescent medium). The plume from a hydrothermal vent can be regarded as a thermally driven buoyant plume. According to Oeschger and Goodman (1996) and DiIorio et al. (2005), the dominant scattering mechanism is the variation of the relative compressibility from temperature fluctuations.

To check the validity of this assumption, it is assumed that all the fluctuations observed in  $C_{eff}^2$  are induced by the turbulence of the velocity field. In such a case, equation (3.40) becomes

$$C_{eff}^2 = \frac{11}{6} C_{\eta_v}^2 = \frac{11}{6} \frac{C_v^2}{c_0^2}. \quad (3.41)$$

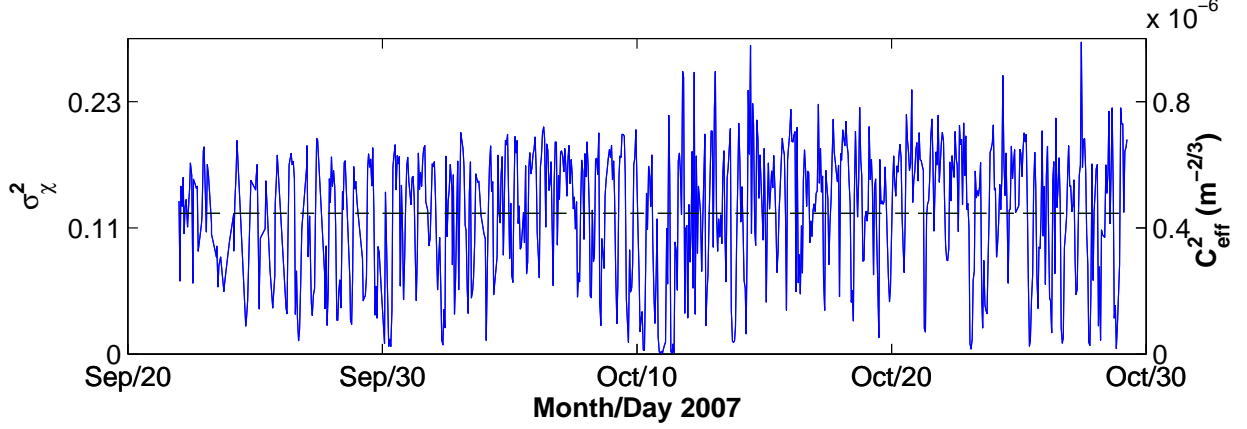


Figure 3.6:  $\sigma_\chi^2$  and  $\tilde{C}_{eff}^2$  calculated from 2007 deployment on Dante. The dashed line pinpoints the level of mean value.

The three dimensional turbulent kinetic energy spectrum  $E(\kappa)$  is defined by

$$\frac{1}{2}\overline{u_i(\mathbf{r})u_i(\mathbf{r})} = \int_0^\infty E(\kappa)d\kappa. \quad (3.42)$$

For isotropic and homogeneous turbulence within an inertial subrange ( $\ell_o \ll \ell \ll L_o$ ),  $E(\kappa)$  can be written as (Tatarskii, 1971; Ostashev, 1991),

$$E(\kappa) = 2\pi(0.033)\frac{11}{3}C_v^2\kappa^{-5/3} = 0.760C_v^2\kappa^{-5/3}. \quad (3.43)$$

Substituting equation (3.43) into equation (3.42) gives

$$\overline{u_i(\mathbf{r})u_i(\mathbf{r})} = 2 \int_0^\infty E(\kappa)d\kappa = 2.281C_v^2\kappa_0^{-2/3}, \quad (3.44)$$

which relates the variance of the turbulent velocity to the structure parameter of velocity fluctuations ( $C_v^2$ ). In deriving equation (3.44), the lower bound of the integral is replaced with  $\kappa_0$  which corresponds to the largest turbulence within the plume which is of the order the plume's diameter ( $\kappa_0 = \frac{2\pi}{14} = 0.449$  rad/m). Replacing  $C_v^2$  in equation (3.44) with  $C_{eff}^2$  based on equation (3.41) one obtains

$$\sigma_u^2 = 2.122c_0^2C_{eff}^2. \quad (3.45)$$

The mean vertical velocity of the plume from Dante at 20 m above the orifice is approximately 0.15 m/s (as will be shown in the next chapter). A maximum turbulent velocity is estimated to be 0.07 m/s (50% of the mean velocity). From this we can assume that the velocity variance  $\sigma_u^2 = 3\overline{u_3^2} \sim 0.015 \text{ m}^2/\text{s}^2$ . The  $C_{eff}^2$  caused by the turbulent velocity is then

$$C_{eff}^2 = \sigma_u^2 / (2.122c_0^2) \approx 3.2 \times 10^{-9} \text{ m}^{-2/3}. \quad (3.46)$$

Note that this value is two orders of magnitude smaller than the measured  $C_{eff}^2$  shown in Figure 3.6, the mean value of which is  $4.5 \times 10^{-7} \text{ m}^{-2/3}$ . This indicates that the fluctuation in the velocity field contributes little to the effective refractive index fluctuation and thus indicates that the temperature variability must be the dominant scattering mechanism within the plume.

With temperature fluctuations as the dominant contributor, equation (3.40) can be simplified as

$$C_{eff}^2 = C_{\eta_s}^2 = C_c^2 / c_0^2, \quad (3.47)$$

where  $C_c^2$  is the structure parameter of sound velocity fluctuation. According to Mackenzie (1981), the sound velocity in the ocean is a function of temperature, salinity and depth which can be written as

$$\begin{aligned} c = & 1448.96 + 4.591T - 5.304 \times 10^{-2}T^2 + 2.374 \times 10^{-4}T^3 \\ & + 1.340(S - 35) + 1.630 \times 10^{-2}D + 1.675 \times 10^{-7}D^2 \\ & - 1.025 \times 10^{-2}T(S - 35) - 7.139 \times 10^{-13}TD^3. \end{aligned} \quad (3.48)$$

Neglecting the fluctuation in salinity and depth and omitting the terms of second or higher order in equation (3.48), the sound speed fluctuation ( $c'$ ) can be put in term of the temperature fluctuation ( $T'$ )

$$c' \approx 4.591T' \quad (3.49)$$

and  $C_c^2$  is related to  $C_T^2$  as

$$C_c^2 = 4.591^2 C_T^2. \quad (3.50)$$

Substituting equation (3.50) into equation (3.47) gives

$$C_{eff}^2 = 4.591^2 C_T^2 / c_0^2. \quad (3.51)$$

For isotropic and homogeneous turbulence within the inertial subrange, the spectrum of temperature fluctuations is (Tennekes and Lumley, 1972),

$$E_T(\kappa) = 2\pi(0.033)C_T^2\kappa^{-5/3} = 0.207C_T^2\kappa^{-5/3}. \quad (3.52)$$

By definition

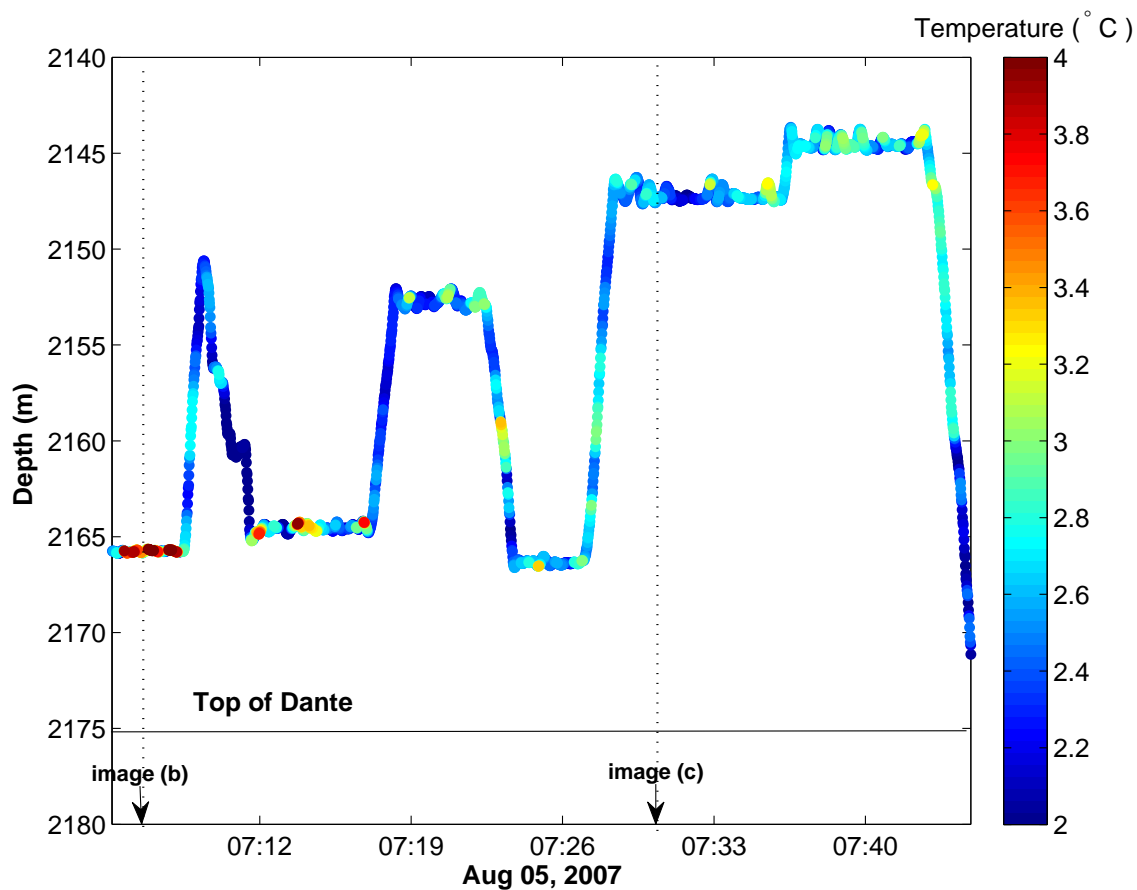
$$\sigma_T^2 = 2 \int_0^\infty E_T \kappa d\kappa = 0.622C_T^2\kappa_0^{-2/3}, \quad (3.53)$$

and substituting equation (3.51) and calculating the variance of temperature fluctuations bounded by the outer scale of turbulence ( $\kappa_0 = 0.449$  rad/m) gives,

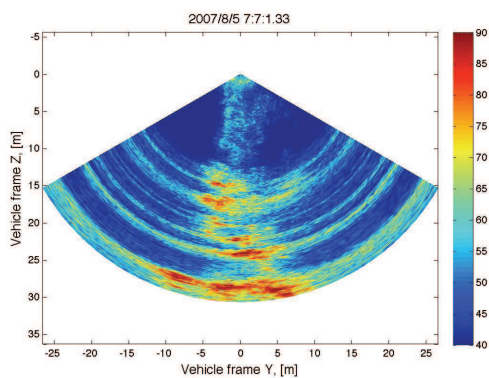
$$\sigma_T^2 = 0.050c_0^2C_{eff}^2. \quad (3.54)$$

Thus the variance of the temperature fluctuations within the plume can be estimated from the measured  $C_{eff}^2$  as shown in Figure 3.6.

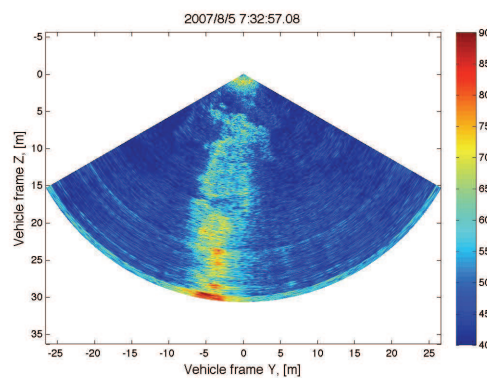
During the AT15-21 cruise, the temperature of the plume from Dante was measured using Jason's CTD (shown in Figure 3.7). The top of Dante is at 2175 m depth and Jason would hover 10 m above Dante and then ride the plume to 20-30 m above (see images in Figure 3.7b and c) The temperature measurements at 19 ~ 21 m above the orifice are extracted from this time series and are shown in Figure 3.8, of which the standard deviation is 0.16°C. Figure 3.9 shows the estimated standard deviation of temperature variation based on the radially averaged  $C_{eff}^2$  given by equation (3.39).  $\langle C_{eff}^2 \rangle$  is used instead of  $\tilde{C}_{eff}^2$  so that it can be compared with Jason's CTD data which is considered spatially averaged due to Jason's random position within the plume during the measurement. The average value shown in Figure 3.9 agrees with Jason's CTD result very well, which suggests the feasibility and accuracy of using acoustic scintillation to measure the temperature variability within a hydrothermal plume.



a)



b)



c)

Figure 3.7: (a) Temperature measurements of the plume above Dante from Jason's CTD data. SM2000 sonar images taken at the times pinpointed in figure (a) at 10 m above (b) and 30 m above (c).

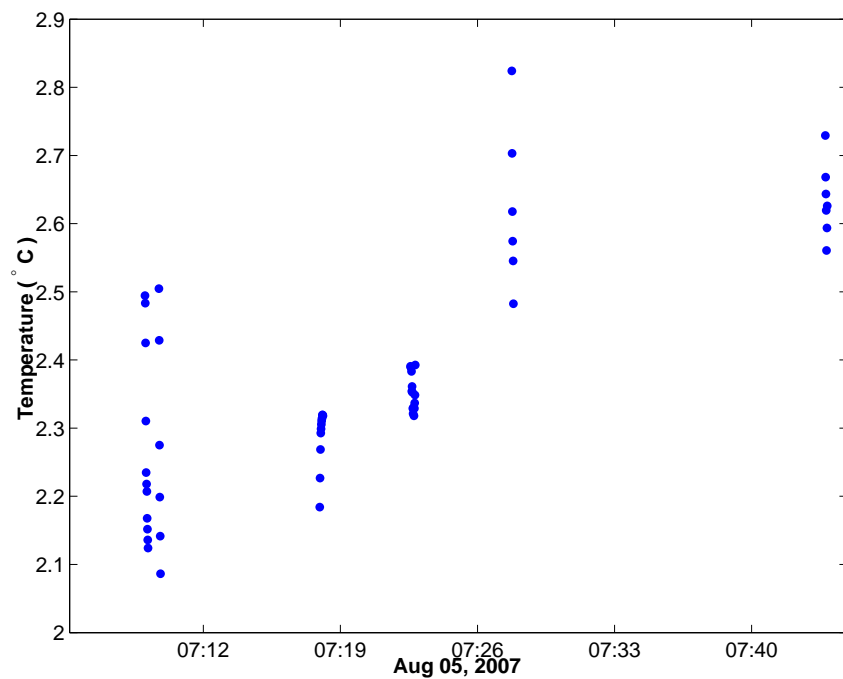


Figure 3.8: Temperature measurements of the plume from Dante between 19-21 m above the orifice.

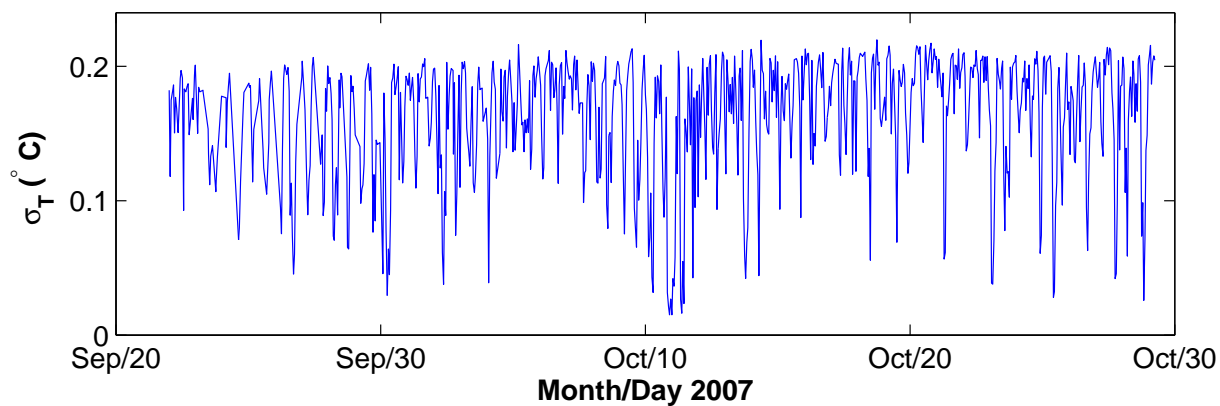


Figure 3.9: Standard deviation of the temperature variability within the plume from Dante at 20 m above the orifice. The dashed line pinpoints the level of mean value,

## CHAPTER 4

### VERTICAL VELOCITY OF HYDROTHERMAL PLUMES

#### 4.1 ACOUSTIC SCINTILLATION METHOD

Acoustic waves propagating through a turbulent medium are affected by absorption, refraction and diffraction. Refraction and diffraction are caused by the effective refractive index fluctuations ( $n_{eff}$ ) within the medium that takes into account velocity and temperature fluctuations. Acoustic scintillation refers to the phenomenon in which the pattern of the acoustic signal modulations are evolving constantly due to the turbulence inside the medium. By measuring the fluctuation of the received signal, properties of the medium can be recovered through an inverse approach. Generally speaking, acoustic scintillation technology is an approach to estimating mean and turbulent features of the medium from the measurement of the fluctuations of the acoustic signal passing through it. One major application of the acoustic scintillation technology is measuring the flow perpendicular to the acoustic propagation direction and parallel to the transducer line array using space time coherence methods.

Acoustic scintillation serves as a non-intrusive flow meter which is used to measure the mean vertical velocity of a hydrothermal plume, as depicted in Figure 4.1. During the measurement, two transmitters are located on one side of the plume while two receivers are located on the other side. In such a way, two parallel acoustic line-of-sights (T1/R1, T2/R2) are formed. In addition, one transmitter and two receivers can be used (e.g T1/R1,2) that defines diverging paths. In this case note that in the center of the propagation path the separation between the two diverging paths is 1/2 that for the parallel path case. The acoustic

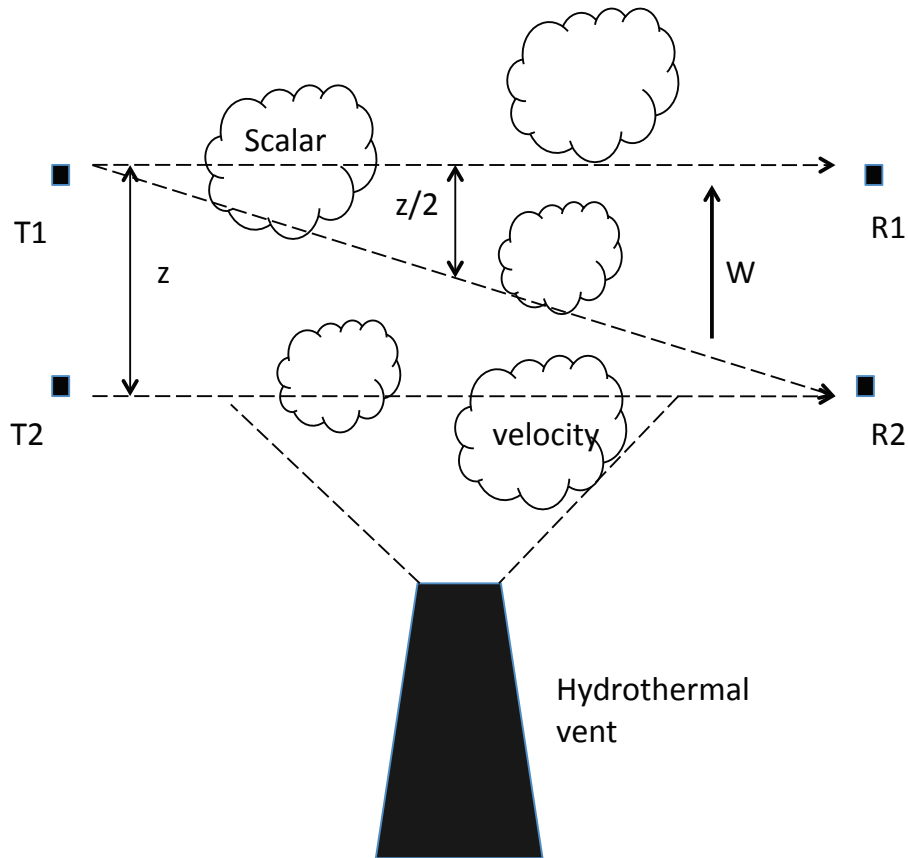


Figure 4.1: Measuring a hydrothermal plume’s vertical velocity with acoustic scintillation.

amplitude at the receivers fluctuates randomly due to the effective refractive index fluctuation ( $n_{eff}$ ) within the plume induced by perturbations of both scalar (temperature and salinity) and vector properties. If the two acoustic paths that form line-of-sights between the transmitter(s) and receivers are close enough, the fluctuation pattern observed at the downstream receiver (R1) will be nearly identical to that of the upstream receiver (R2), except it will be shifted in time by a lag  $\tau$  (see Figure 4.2 a). This is because the turbulent eddies are embedded in the mean flow and their evolution during the time they cross the two line-of-sights is negligible (‘frozen turbulence’).

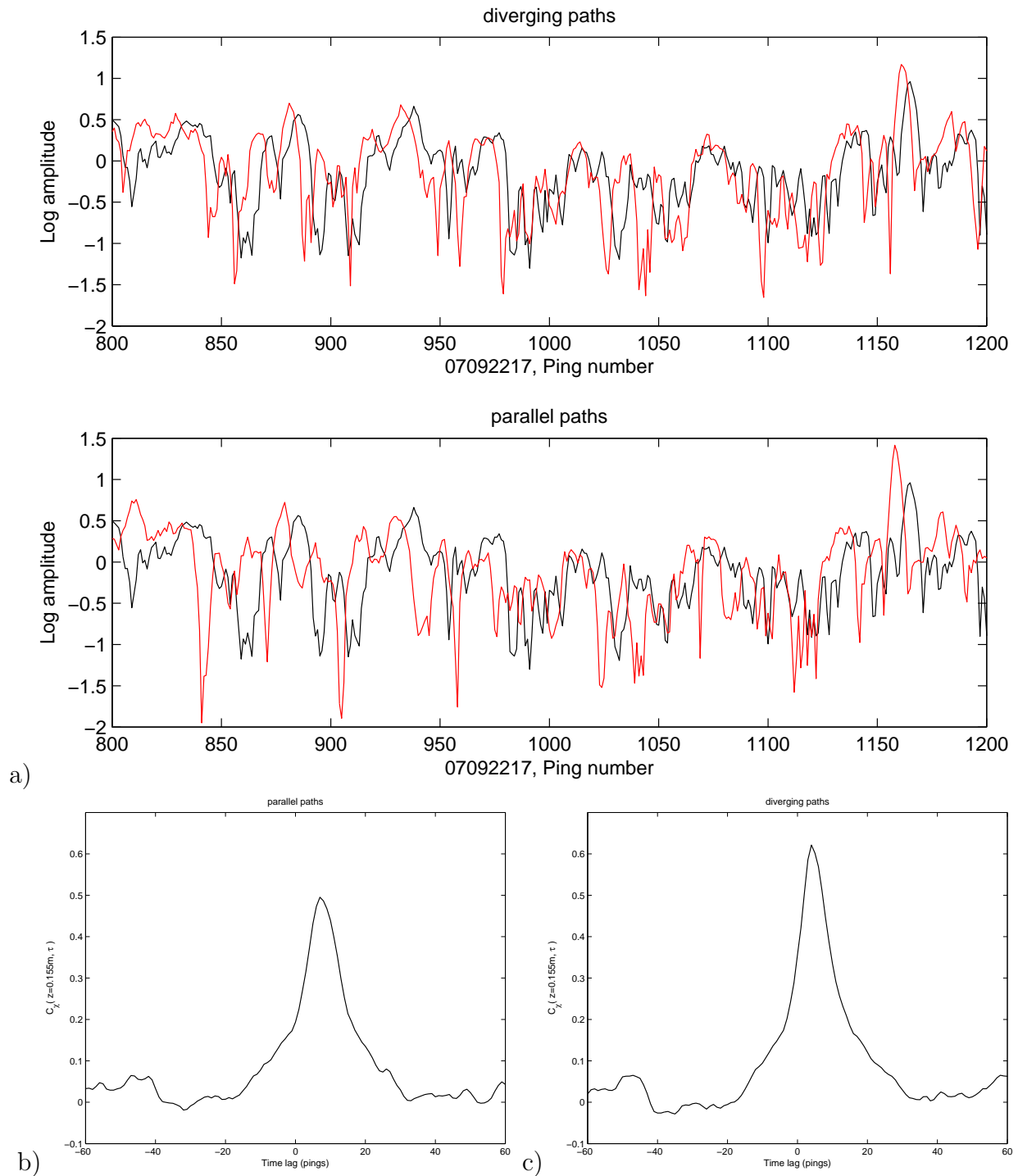


Figure 4.2: (a) Log-amplitude time series for parallel paths (top panel) and diverging paths (bottom panel). (b) Cross-covariance function for parallel paths. (c) Cross-covariance function for diverging paths.

The time lag  $\tau$  can be measured by analyzing the space-time cross-covariance function of the received log-amplitude signals shown in Figure 4.2 b and c. The space-time cross covariance function of the received signals for weak scattering is given by Clifford and Farmer (1983):

$$C_\chi(\varrho, \tau) = 4\pi^2 k^2 \int_0^L dy \int_0^\infty d\kappa \kappa \Phi_{eff}(\kappa, y) J_0(\kappa|\varrho - W(y)\tau|) \sin^2\left(\frac{\kappa^2 y(L-y)}{2kL}\right), \quad (4.1)$$

which is maximum when  $|\zeta - W\tau| = 0$ . In this equation:  $W$  is the mean vertical velocity of the plume;  $\zeta$  is the path averaged vertical separation of the two line-of-sights and according to Figure 4.1,  $\zeta = z$  for parallel paths and  $\zeta = \frac{1}{L} \int_0^L zy/L dy = z/2$  for diverging paths with  $z=15.5$  cm;  $\chi$  is the log-amplitude fluctuation ( $\chi = \ln \frac{A}{A_0}$  where  $A_0$  is the mean amplitude of the received signal);  $\Phi_{eff}(\kappa, y)$  is the three dimensional isotropic and homogeneous effective refractive index spectral density at the plane  $y = \text{const}$  where  $\kappa$  is the magnitude of the spatial wave number ( $\kappa = \sqrt{\kappa_x^2 + \kappa_z^2}$ );  $k = w/c$  is the system's acoustic wave number where  $w$  is the system's radian frequency and  $c$  is the sound velocity;  $L$  is the length of the transmitter/receiver line-of-sight;  $J_0$  is the zero order Bessel function.

The derivation of equation (4.1) is based on the validity of the Taylor hypothesis which is also known as Taylor's 'frozen turbulence' hypothesis stating that all the temporal variations within the field are determined only by the spatial perturbations advected along the mean flow. Based on this hypothesis, the temporal coherence between the signals is caused by the advection of 'frozen' spatial patterns past the two parallel line-of-sights. The validity of this hypothesis is proven by the significant correlation between the signals shown in Figure 4.2 from which the time lag  $\tau$  can be calculated as the delay to the peak ( $\tau_p$ ).

The vertical velocity of the plume is then calculated as

$$W = \frac{z}{\tau_p}, \quad (4.2)$$

for parallel paths and

$$W = \frac{z}{2\tau_p}, \quad (4.3)$$

for diverging paths. According to DiIorio (1994) and Tatarskii (1961), the acoustic system is most sensitive to turbulent structures having scale sizes the radius of the first Fresnel zone ( $\sqrt{\lambda L} \approx 0.7 \text{ m}$ ) lying in the middle of the acoustic line-of-sight (as shown in Chapter 3.2). Therefore for highly turbulent environments, diverging paths may have an advantage over parallel paths due to the reduced path averaged vertical separation  $\zeta$  which leads to enhanced coherence between the signals (see Figure 4.2).

## 4.2 VERTICAL VELOCITY OF THE PLUME FROM DANTE

The vertical velocity of the hydrothermal plume of Dante (measured at 20 m above the orifice) during the 2007 deployment is shown in Figure 4.3 using diverging paths. Each 15 min burst of data each hour was broken up into three 5 min intervals from which the cross correlation was derived. A quadratic fit to the peak then gives the delay  $\tau_p$  from which the velocity is calculated from equation (4.3). The average vertical velocity measured at Dante is 0.14 m/s. Tidal oscillations can be observed in the vertical velocity result, of which the power spectral density is shown in Figure 4.4. Oscillations are forced at two frequencies: M2 tidal constituent and the 4-day oscillations observed by Cannon and Thomson (1996) in the current meter measurements around the Endeavour segment.

Figure 4.5 shows an expanded section with tidal heights (blue line) superimposed on the plume's vertical velocity (green line). The tidal height estimation is derived from a regional tidal model for the west coast based on the tidal inversion solutions developed by Egbert et al. (1994) and Egbert and Erofeeva (2002). The Oregon State University (OSU) Tidal Inversion Software is available at <http://volkov.oce.orst.edu/tides/otis.html>. The tidal periodicity (dominated by the M2 tidal harmonic) is observed in the vertical velocity measurement. Vertical velocity reaches a maximum when water is moving from high level to low level (during ebbing tide) and reaches a minimum when water is moving from low level to high level (during flooding tide). This phenomenon suggests a certain interaction between

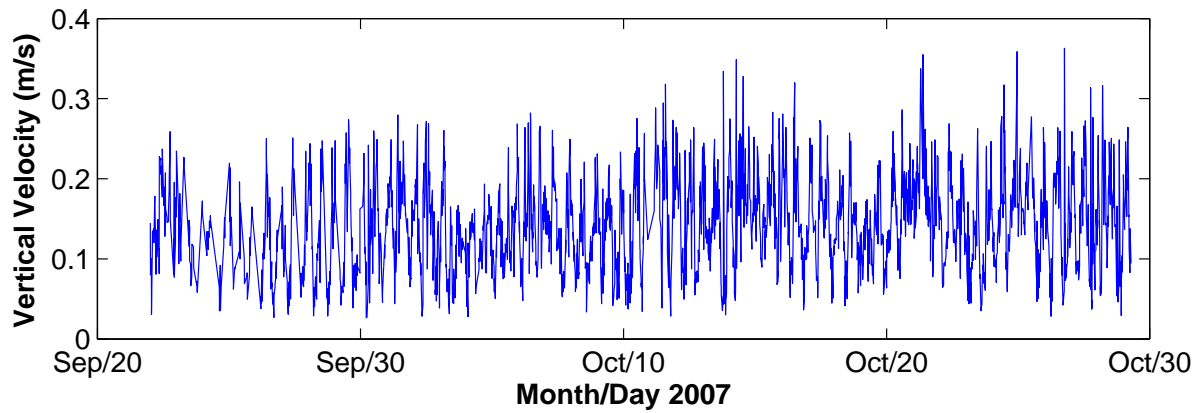


Figure 4.3: Vertical velocity of the plume from Dante at 20 m above the orifice measured in 2007.

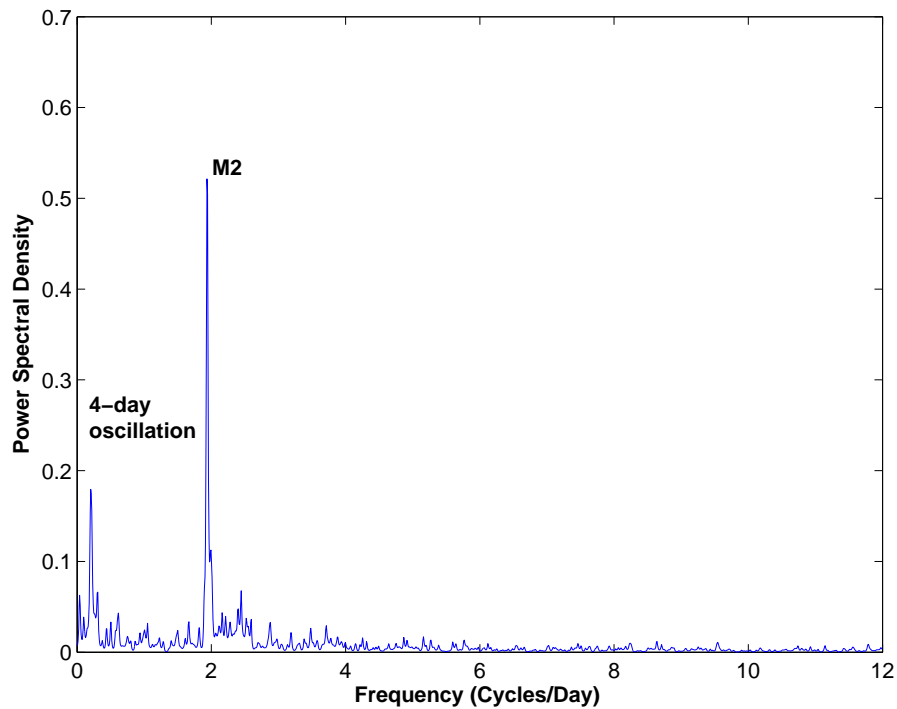


Figure 4.4: Power spectral density of the plume's vertical velocity measured at 20 m above Dante.

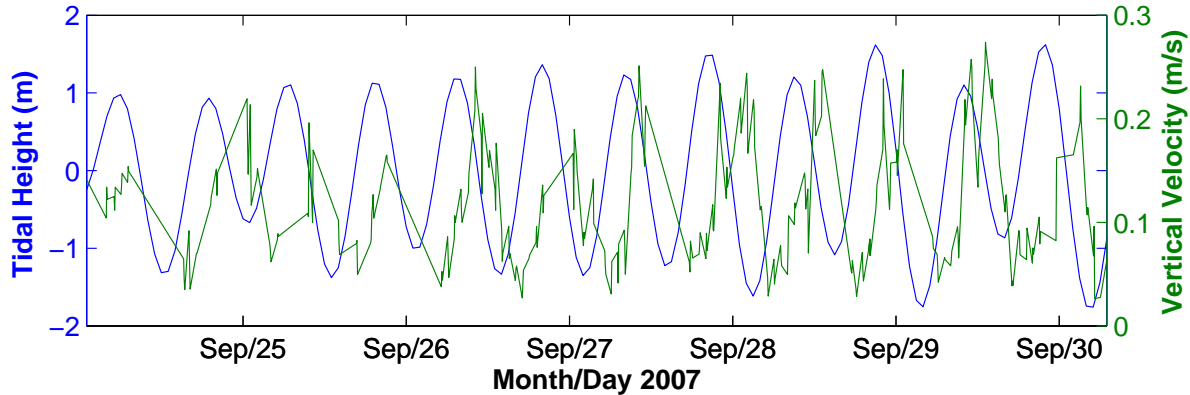


Figure 4.5: Tidal height vs the plume’s vertical velocity.

the tidal currents and the vertical velocity of the hydrothermal plume which will be further investigated in Chapters 5 and 6.

During the experiment, the ambient ocean current may introduce errors into the acoustic scintillation measurement of vertical velocity. This is because the horizontal current will tilt the transmitter and receiver array away from their vertical position by a certain angle. Such a swing could diminish the vertical separation between the parallel or diverging line-of-sights and make the acoustic scintillation measurement an overestimate of the actual vertical current velocity. An estimate of this error induced by the ambient current is given as follows. The deviation of the transmitter and receiver caused by the horizontal current can be estimated using the Mooring Design and Dynamics (MDD) model developed by Dewey (1999) (see <http://canuck.seos.uvic.ca/rkd/mooring/moordyn.html>). The maximum horizontal flow observed within the axial valley is of the order of 10 cm/s (as will be discussed in Chapter 5). According to the MDD model, the deviation angle of the transmitter and receiver under such a horizontal current is approximately  $\theta = 1.85^\circ$  and the transmitter and receiver are assumed to move in the same way. In such a case, the path-averaged vertical separation of the parallel line-of-sight becomes  $z_{\perp p} = z \cos \theta = 15.492$  cm and for diverging paths

$z_{\perp d} = z \cos \theta / 2 = 7.746$  cm. If the average vertical velocity measured at Dante is 0.14 m/s (the mean value in Figure 4.3), then the actual time lag is  $\tau_p = z_{\perp p} / 0.14 = 1.107$  s for parallel paths and  $\tau_d = z_{\perp d} / 0.14 = 0.553$  s. Uncertainty caused by the mooring tilt can thus be calculated as  $\Delta U_{\perp} = z / \tau_p - 0.14 \sim 8 \times 10^{-5}$  m/s for both diverging and parallel paths. Based on this estimation, the error induced by the ambient flow is negligible and therefore mooring oscillations do not affect the vertical velocity measurements. Also mooring oscillations do not affect amplitude fluctuations because path length variations are small. In the spectrum for log-amplitude fluctuations as shown in Figure 3.5, no variability in the amplitude is seen to be the result of mooring oscillations.

According to Figure 4.3 and Figure 3.8, the mean vertical velocity and temperature of the plume from Dante at 20 m above the orifice is  $W_{20} = 0.14$  m/s and  $T_{20} = 2.4^{\circ}\text{C}$  respectively. The ambient temperature at 20 m above the orifice is obtained from the Jason CTD data as  $T_{a20} = 1.9^{\circ}\text{C}$ . Taking the specific heat of the plume as  $c_p = 4000$  J/(kg $^{\circ}\text{C}$ ) and the density as  $\rho = 1027$  kg/m $^3$ , the heat flux is calculated as,

$$F = c_p \rho W_{20} (T_{20} - T_{a20}) = 2.88 \times 10^5 \text{ W/m}^2. \quad (4.4)$$

The radius of the plume at 20 m above the orifice is  $R_{20} = 7$  m (see Figure 2.20) and thus the heat transport of the plume from Dante is

$$H = \pi R_{20}^2 F \cong 44 \text{ MW} \quad (4.5)$$

which represents the minimum. The heat output could be much higher if the plume is hotter and faster but it is difficult to parameterize the radius under specific heat flow conditions.

## CHAPTER 5

### HYDROTHERMAL PLUMES IN HORIZONTAL CROSS FLOWS

#### 5.1 HORIZONTAL FLOW WITHIN THE AXIAL VALLEY

The tidal characteristics observed in the turbulence and vertical velocity of the hydrothermal plume shown in Chapters 3 and 4 respectively indicate a significant interaction between horizontal flows and hydrothermal plumes within the Main Endeavour vent Field (MEF). During the past two decades, currents within the axial valley have been studied and documented extensively (Thomson et al., 1990; Allen and Thomson, 1993; Thomson et al., 2003, 2005; Berdeal et al., 2006), among which, Thomson's measurements in 2000 and 2001 along with Berdeal's measurements in 2002 and 2003 are the latest. The location of their deployments are shown in Figure 5.1. The 2000 deployment was in the southern axial valley to the southwest of the MEF at a depth of 2187 m while the 2001 deployment was in the central axial valley to the northeast of the MEF at a depth of 2193 m. The 2002 deployment was at 2217 m depth to the south of MEF on smooth topography while the 2003 deployment was at depth 2202 m in the southern MEF but close to a steep valley wall on the west. The results obtained from these four deployments indicate that currents in the axial valley are highly baroclinic (currents within the axial valley differ significantly from those above the valley).

According to Thomson et al. (2003) and Allen and Thomson (1993), the mean flow within the axial valley is near-steady and convergent. At the southern and central parts of the valley, the mean flow is predominantly northward and strongest (5 cm/s) while at the northern part of the valley, the mean flow becomes southward and weakest (1 cm/s). The convergent mean flow within the axial valley is believed to be induced by turbulent entrainment of the hydrothermal plumes (Thomson et al., 2003, 2005). The northward mean

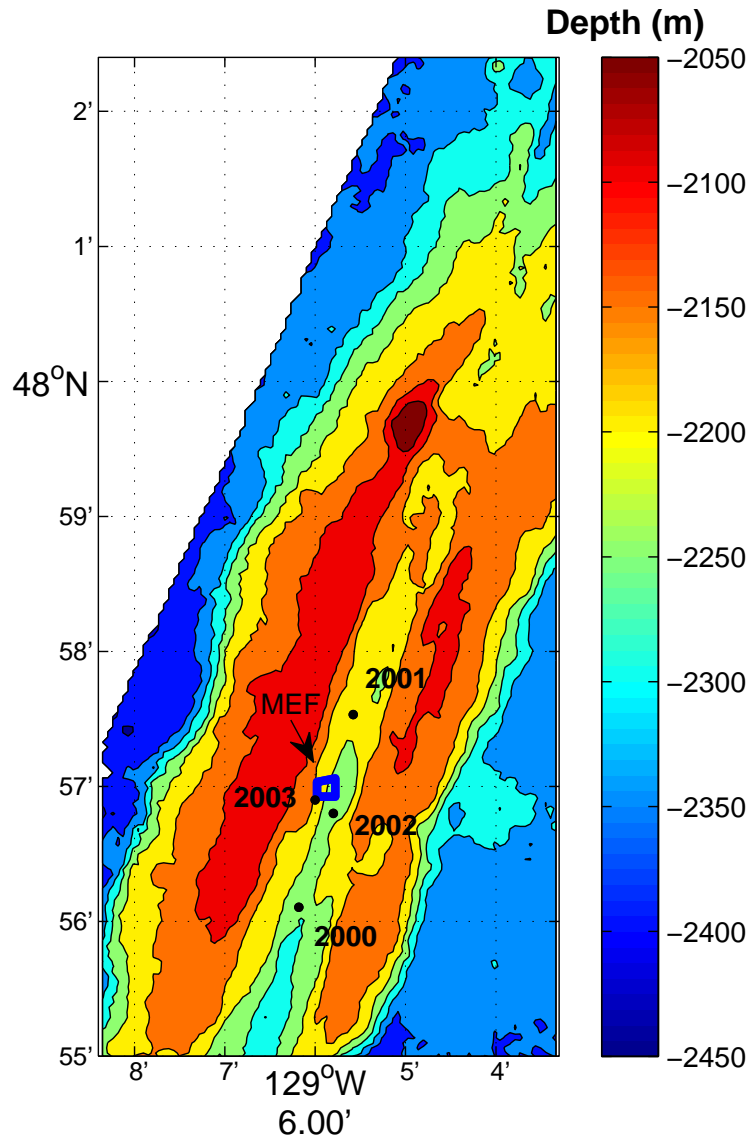


Figure 5.1: Locations of the current meter deployments by Thomson in 2000 and 2001 and by Berdeal in 2002 and 2003.

flow extends to the central valley due to the shallow topographic saddle at the northern end of the valley and more intensive hydrothermal activity within the southern and central valley (Thomson et al., 2003).

The vertical structure of the mean horizontal flow within the axial valley was recorded in detail by Berdeal et al. (2006) with a high vertical resolution (4 m). Based on the result of the 2002 deployment, the mean flow amplifies with depth and reaches a maximum of 5 cm/s at 15 m above the bottom. With regard to the 2003 deployment, the measured mean flow decreases with depth and reaches a minimum of 1 cm/s at 20 m above the bottom. Below this level, the mean flow increases rapidly and reaches a maximum of 4 cm/s at 7 m above the bottom. The sulfide structures are typically 10-20 m tall and could affect the flow 0-10 m from the bottom. The mean flow measured from the second deployment is much different from that of the first deployment because the first deployment is in an area with relatively smooth bathymetry and further away from the hydrothermal vent field while the latter one is in the vicinity of the west valley wall and closer to the hydrothermal vent field (see Figure 5.1).

Figure 5.2 shows the daily averaged current measurements from the 2000 deployment (data courtesy of R. Thomson IOS). The upper panel shows the current vectors recorded at 200 m above the bottom (above the axial valley at 1974 m depth) while the lower panel shows those recorded at 50 m above the bottom (within the axial valley at 2124 m depth). With regard to the 200 m data, the mean flow was primarily southwesterly for most of the time, but on Sep 08 and Sep 20 the flow reversed to the north. In contrast, current vectors at 50 m above the bottom were universally northerly with no inversion during the measurement. The dramatic discrepancy between the two depths demonstrates the baroclinicity of the mean currents at the axial valley, which is believed to be caused by the confinement of the valley and the circulation induced by the hydrothermal activity (Thomson et al., 2003, 2005).

Figure 5.3 (a) is a scatter plot of the mean residual flow within the central valley using 36 hr low-pass filtered data from the 2001 deployment (data courtesy of R. Thomson IOS). The

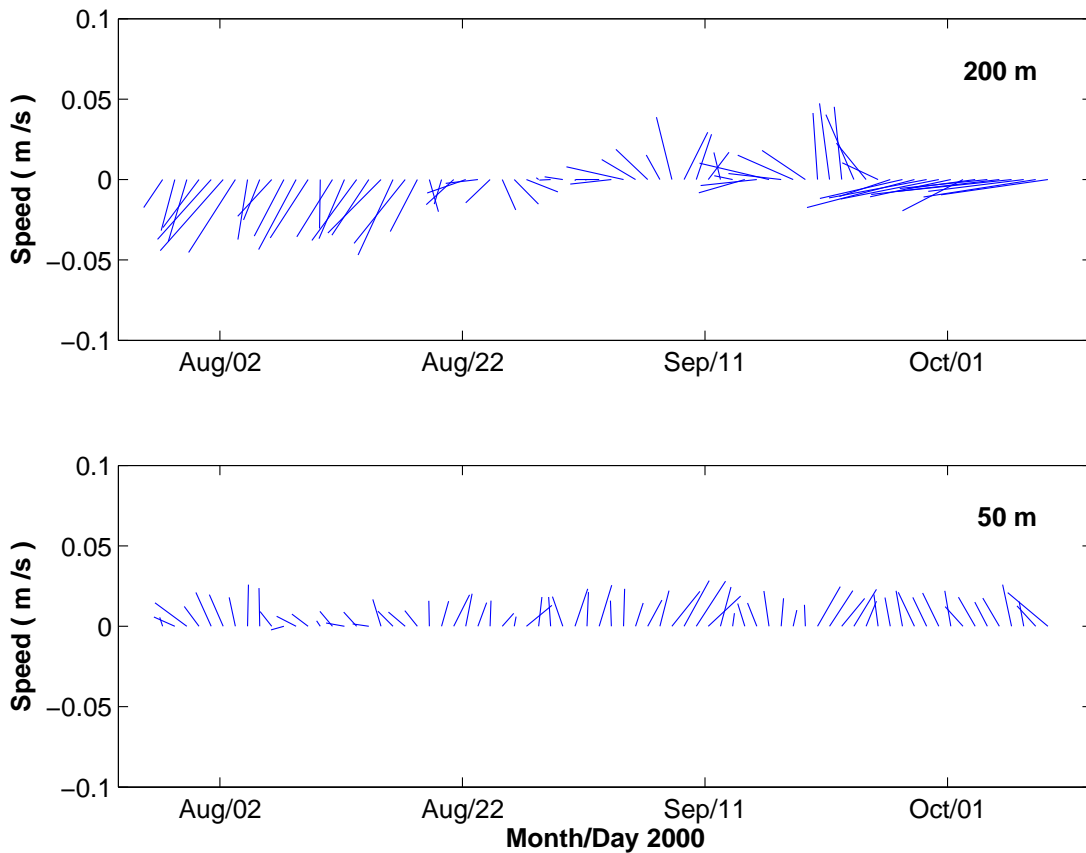
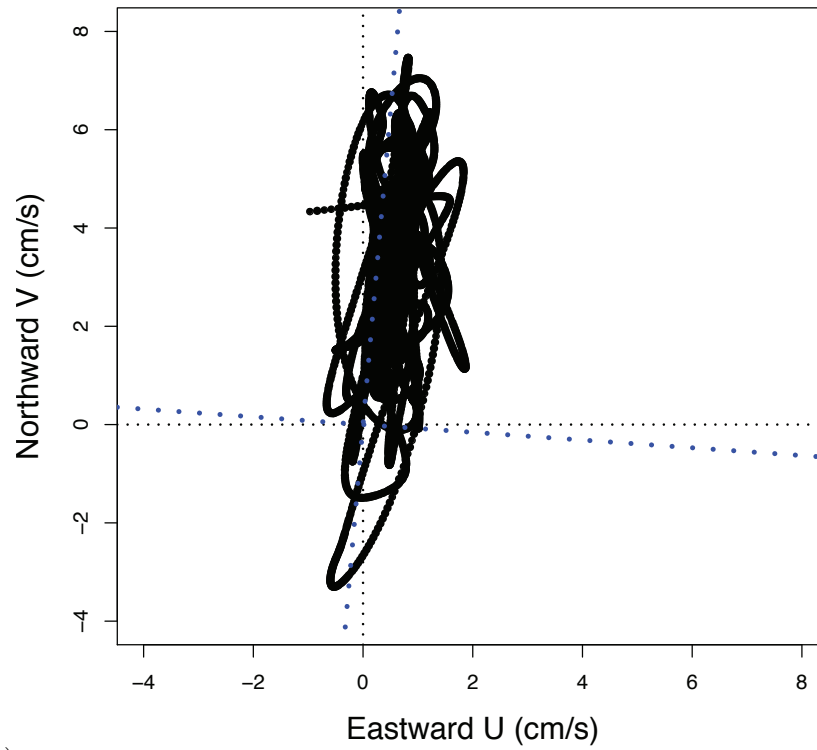
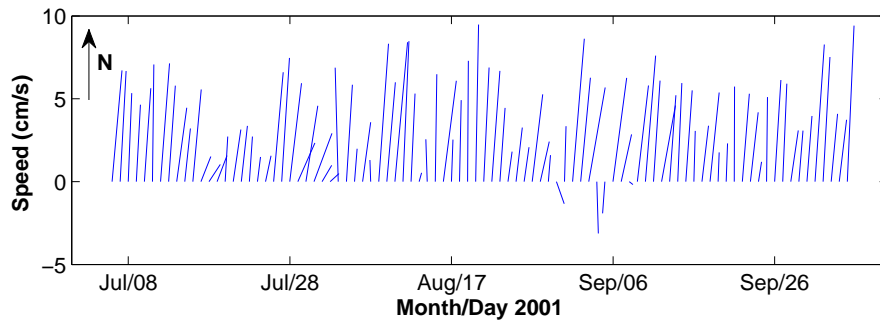


Figure 5.2: Daily averaged current vectors measured during the 2000 deployment (data courtesy of R. Thomson) within the axial valley at 200 m (upper panel) and 50 m (lower panel) above the bottom which correspond to depths of 1974 and 2124 m respectively.

depth of the current meter was 2174 m (19 m above the bottom at a depth that corresponds to the top of Dante) and three months of data with a sampling interval of 20 min is shown. The blue dotted lines are the directions of the major and minor axes calculated using principle component analysis, from which it can be seen that the mean flow is nearly meridional within the central valley. In addition, the mean flow is toward the north with an average velocity of 4 cm/s in most cases and rarely reverses to the south as can be seen in Figure 5.3 (b).



a)



b)

Figure 5.3: Daily averaged mean flow within the central valley measured during the 2001 deployment (data courtesy R. Thomson) at 19 m above bottom at 2175 m depth. (a) scatter plot and (b) stick plot.

In addition to the near-steady convergent mean flow, tidal oscillations are also prevalent within the axial valley. According to Allen and Thomson (1993) and Thomson et al. (2003), the oscillatory currents are nearly rectilinear above the valley but become amplified and clockwise rotary as they approach the valley's crests. Within the valley, tidal oscillations are attenuated and nearly rectilinear due to the rectification of the steep topography and the M2 oscillation is the most dominant frequency. Figure 5.4 is the scatter plot of the tidal oscillations within the central valley extracted from 2001 data using the tidal harmonic analysis program T-Tide developed by Pawlowicz et al. (2002) which follow the tidal harmonic methods developed by Foreman (1978, 1977) and Foreman and Henry (1979). In Figure 5.4, the blue dotted lines define the direction of the major and minor axes derived through principal component analysis, from which it can be seen that tidal oscillations within the central valley are nearly meridional. From T-Tide results, tidal oscillations account for nearly 45 percent of the total variance in the 2001 data. Figure 5.5 shows the rotary spectrum of the tidal oscillations within the central valley, from which it can be seen that, M2 is the most dominant frequency and is nearly rectilinear.

Figure 5.6 shows a comparison between the measured pressure and the northward component of the horizontal flow within the central valley. According to Figure 5.6, the horizontal flow is enhanced during the flooding tide and suppressed during the ebbing tide due to the northward mean residual flow which adds to the northward flooding tide and reduces the southward ebbing tide.

## 5.2 COMPARISON WITH ACOUSTIC SCINTILLATION MEASUREMENTS

Tidal currents within the axial valley during the acoustic scintillation deployment in 2007 can be extrapolated from the 2001 current meter data using the harmonic analysis program T-Tide. The total horizontal flow can thus be estimated by adding the northward mean residual flow calculated from the current meter data to the extrapolated tidal currents. Figure 5.7 shows a comparison between the tidal height predicted by the OSU tidal inverse model and

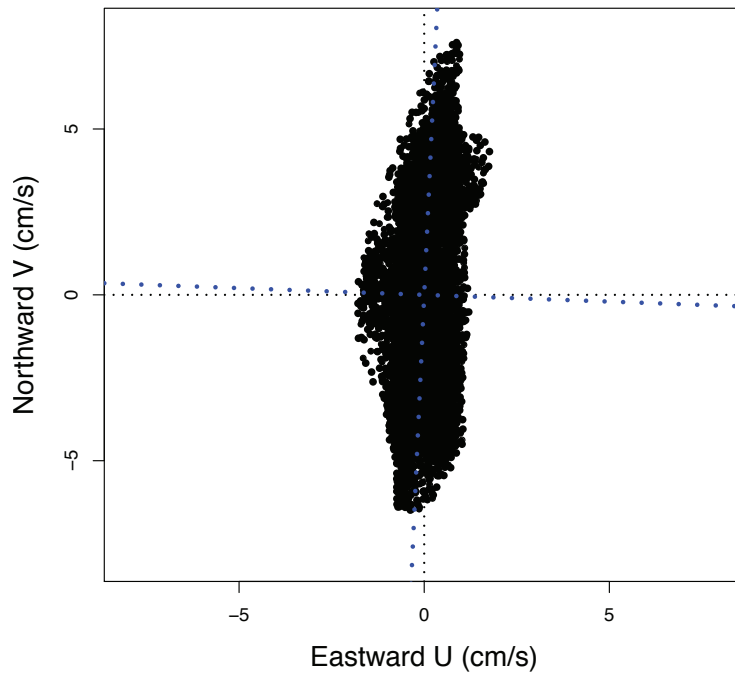


Figure 5.4: Tidal oscillations within the central valley measured during the 2001 deployment (data courtesy R. Thomson) at 19 m above bottom at 2175 m depth.

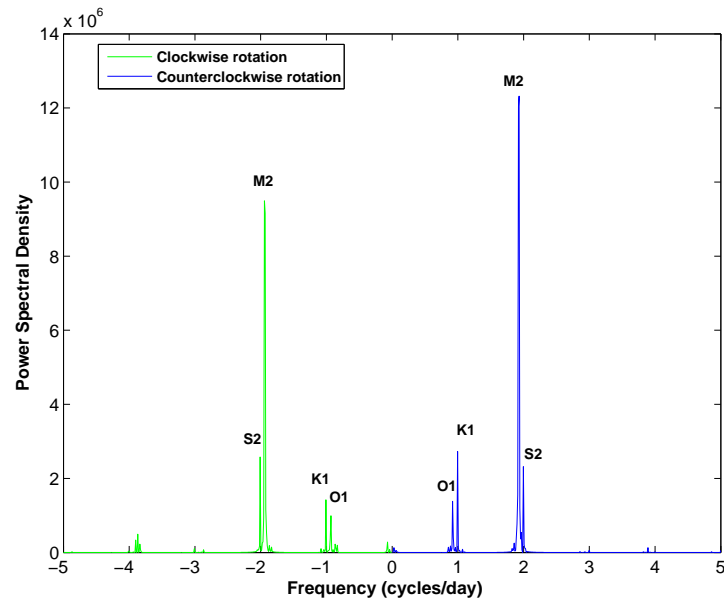


Figure 5.5: Rotary spectrum of the tidal oscillations measured during the 2001 deployment (data courtesy R. Thomson) at 19 m above bottom at 2175 m depth.

the estimated horizontal flow in 2007. Similar to that in 2001 (see Figure 5.6), the horizontal flow reaches a maximum during flooding tide and reaches a minimum during ebbing tide.

Figure 5.8 shows an expanded comparison between the horizontal flow and the measured vertical velocity of the plume from Dante during the 2007 deployment. A significant negative correlation ( $r \sim -0.55$ ) is observed. The plume's vertical velocity reaches a minimum when the horizontal flow is a maximum and vice versa. This phenomena indicates that there is an the interaction between the plume's vertical velocity and the high frequency tidal oscillation (M2 periodicity) within the horizontal flow.

Figure 5.9 shows a comparison between the centerline effective refractive index structure parameter ( $\tilde{C}_{eff}^2$ ) measured during the 2007 deployment from the plume emanating from Dante and the horizontal flow. A significant negative correlation ( $r \sim -0.53$ ) is also evident:  $\tilde{C}_{eff}^2$  reaches a maximum when the horizontal flow is at a minimum and vice versa. Such a phenomena indicates an interaction between the turbulence within the plume (parameterized by  $\tilde{C}_{eff}^2$ ) and the high frequency tidal oscillation (M2 periodicity) within the horizontal flow.

### 5.3 SYNOPSIS

From this analysis, the plume's interaction with the horizontal flow within the Main Endeavour Field can be generalized as follows:

1. Plume's vertical velocity reaches a maximum when the horizontal flow is weakest (during the ebbing tide) while it reaches a minimum when the horizontal flow is strongest (during the flooding tide);
2. The turbulence within the plume reaches a maximum when the horizontal flow is weakest (during the ebbing tide) while it reaches a minimum when the horizontal flow is strongest (during the flooding tide).

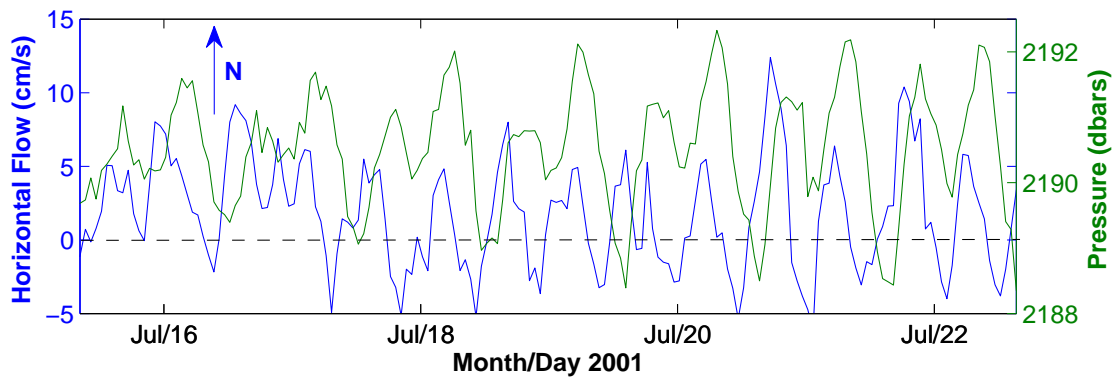


Figure 5.6: Pressure vs horizontal flow measured during the 2001 deployment (data courtesy R. Thomson ).

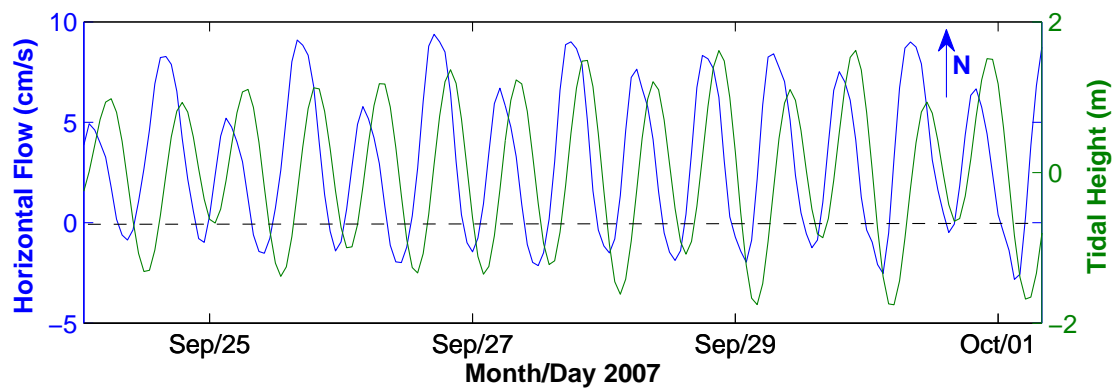


Figure 5.7: Tidal height from the OSU tidal inversion model versus horizontal flow extrapolated from T-TIDE.

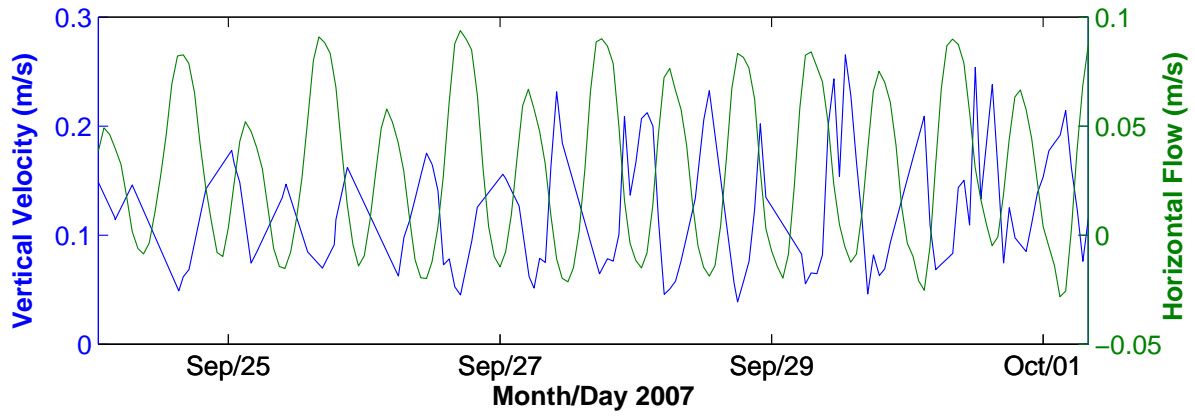


Figure 5.8: Vertical velocity vs horizontal flow

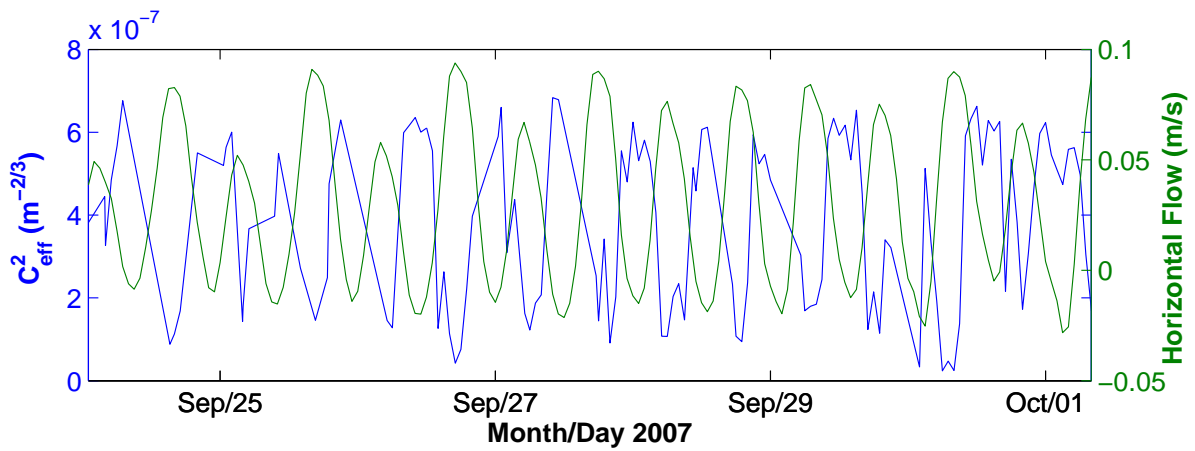


Figure 5.9:  $\tilde{C}_{eff}^2$  vs horizontal flow

Such characteristics can be explained by an entrainment and tidal response hypothesis. According to the laboratory experimental results carried out by Fan (1967), entrainment can be enhanced by the ambient horizontal cross-flow for a turbulent buoyant plume. When the horizontal flow is weak (during the ebbing tide), less ambient ocean water is entrained into the plume. In such a case, the plume is faster and hotter thus temperature fluctuations increase which lead to a stronger turbulent intensity within the plume thus the higher  $\tilde{C}_{eff}^2$  measured by the acoustic scintillation system. When the horizontal flow is strong (during the flooding tide), more ambient ocean water is entrained into the plume. In such a case, the plume is slower and cooler with reduced temperature fluctuations which lead to the weaker turbulent intensity within the plume thus the smaller  $\tilde{C}_{eff}^2$  measured by the acoustic scintillation system.

## CHAPTER 6

### INTEGRAL MODEL OF HYDROTHERMAL PLUMES

Deep sea hydrothermal plumes can be regarded as turbulent buoyant plumes and jets. Driven by the gravitational buoyancy force, hydrothermal plumes may rise up to hundreds of meters above the orifice (McDuff, 1995). Ambient ocean water is entrained into the plume through its ascent which makes the plume diluted and cooled. Finally, an equilibrium level is reached when the density deficit between the plume and ambient environment is offset by the entrainment. The plume overshoots the equilibrium level owing to its remaining momentum and then falls back and spreads laterally at its neutral buoyancy level (Turner, 1986). Direct measurements of physical and chemical properties of hydrothermal plumes (i.e. radii and terminal height, vertical velocity, temperature and salinity anomalies) are limited and such properties are of crucial importance for the study of volcanic-tectonic-hydrothermal systems and the transport of mineral and heat from the oceanic crust to the deep ocean. Therefore, the goal of this chapter is to establish an integral model to estimate the mean physical properties of the hydrothermal plume emanating from the sulfide edifice Dante within the Main Endeavour Field. Furthermore, an entrainment rate proportional to the ambient horizontal flow is used to test the validity of a tidally varying entrainment rate.

#### 6.1 INTEGRAL MODEL

The integral model used to describe the time-averaged plume behavior was first developed by Morton et al. (1956) (MTT model). The MTT model is derived from the conservation equations for volume, momentum and density deficit. The essence of the MTT model is Taylor's entrainment hypothesis which states that the velocity of the inflow of diluting water

into any turbulent, buoyant jet/plume would be proportional to the characteristic velocity in the jet/plume at the level of the inflow. The proportionality constant ( $\alpha$ ) is defined as the entrainment coefficient. In the case of a hydrothermal plume emanating into a quiescent environment (without horizontal cross-flows), the characteristic velocity is taken as the plume's axial velocity. Therefore the relation,

$$\frac{d}{ds}(\pi b^2 U_s) = 2\pi b(s)\alpha U_p(s) \quad (6.1)$$

is satisfied. The left hand side of equation (6.1) is the gradient of the plume's volume transport along its axis. As for the right hand side,  $b(s)$  is the radius of the plume's cross-section perpendicular to its axis and  $U_p(s)$  is the plume's axial velocity (Fan, 1967).

The effect of the horizontal crossflow, however, is not incorporated into the MTT model. According to the discussion made in the previous chapter, the mean horizontal flow within the axial valley can reach an order of 10 cm/s and a tidal oscillation of the same order of magnitude was also observed. Due to the existence of the horizontal cross-flow, the trajectory of the plume will bend toward the downstream direction of the flow because of both the low-pressure wake-like region established behind the plume and the entrainment of horizontal momentum from the cross-flow (Fan, 1967). In addition to the horizontal cross-flow, stratification of the ambient environment also has an important influence on the plume's behavior (a hydrothermal plume will eventually reach its terminal height where neutral buoyancy is reached in a stratified environment). Therefore, an extension to the MTT model is needed to make it suitable for modeling the rise of a hydrothermal plume in a stratified medium under significant horizontal cross-flows.

## 6.2 DIMENSIONAL ANALYSIS

In general, the behavior of a hydrothermal plume can be schematized as the problem of a turbulent, buoyant jet/plume in a stratified medium with uniform horizontal cross-flows. The reason why the term 'jet/plume' is used here is because a hydrothermal plume is affected by

both the initial momentum transport and the initial buoyancy transport. Thus it should be considered as a combination of a purely momentum driven jet and a purely buoyancy driven plume, and therefore the mean properties of a hydrothermal plume should be functions of the initial volume transport  $Q$ , initial specific momentum transport  $M$ , initial specific buoyancy transport  $B$ , mean horizontal cross-flow  $U$  and ambient relative stratification  $\epsilon$ , which are defined as follows:

$$Q = \frac{1}{4}\pi D^2 W \quad (6.2)$$

$$M = QW = \frac{1}{4}\pi D^2 W^2 \quad (6.3)$$

$$\epsilon(z) = \frac{\rho_{a0} - \rho_a(z)}{\rho_{a0}} = \frac{\Delta\rho_a}{\rho_{a0}} \quad (6.4)$$

$$B = \frac{\Delta\rho}{\rho_{a0}}gQ = -\frac{1}{\rho_{a0}}\frac{\partial\rho}{\partial T}\Delta TgQ = g\alpha_t\Delta TQ \quad (6.5)$$

in which  $D$  is the diameter of the vent's orifice,  $W$  is the plume's exit velocity,  $\Delta T = T_0 - T_{a0}$  is the plume's temperature anomaly at the orifice,  $\rho_a$  is the ambient density,  $\rho_{a0}$  and  $T_{a0}$  are the ambient density and temperature at the depth of the orifice ( $z = 0$ ) and  $\alpha_t$  is the thermal expansion coefficient for water ( $\alpha_t = -\frac{1}{\rho_{a0}}\frac{\partial\rho}{\partial T} \sim 10^{-4} \text{ }^\circ\text{C}^{-1}$ , Turner and Campbell (1987)). The physical units of  $Q$ ,  $M$  and  $B$  are then:  $\text{m}^3/\text{s}$ ,  $\text{m}^4/\text{s}^2$  and  $\text{m}^4/\text{s}^3$  respectively.

Based on these four initial conditions, several characteristic length scales are derived (see Figure 6.1 for a schematic drawing following Fischer et al. (1979)):

1.  $L_Q = Q/M^{1/2}$  : for  $z \gg L_Q$ , the turbulence along the plume's axis reaches stationary decay (momentum is more important than volume transport); for  $z \ll L_Q$  the flow establishment zone is where the turbulence is at a non-stationary state due to the existence of large scale eddies and the mean properties of the buoyant jet/plume are influenced by the geometry of the orifice ( $Q$  more important than  $M$ ).
2.  $L_M = M^{3/4}/B^{1/2}$ : for  $z \gg L_M$  (plume zone), the buoyant jet/plume acts like a purely buoyancy driven plume; for  $z \ll L_M$  (jet zone), the buoyant jet/plume behaves like a purely momentum driven jet.

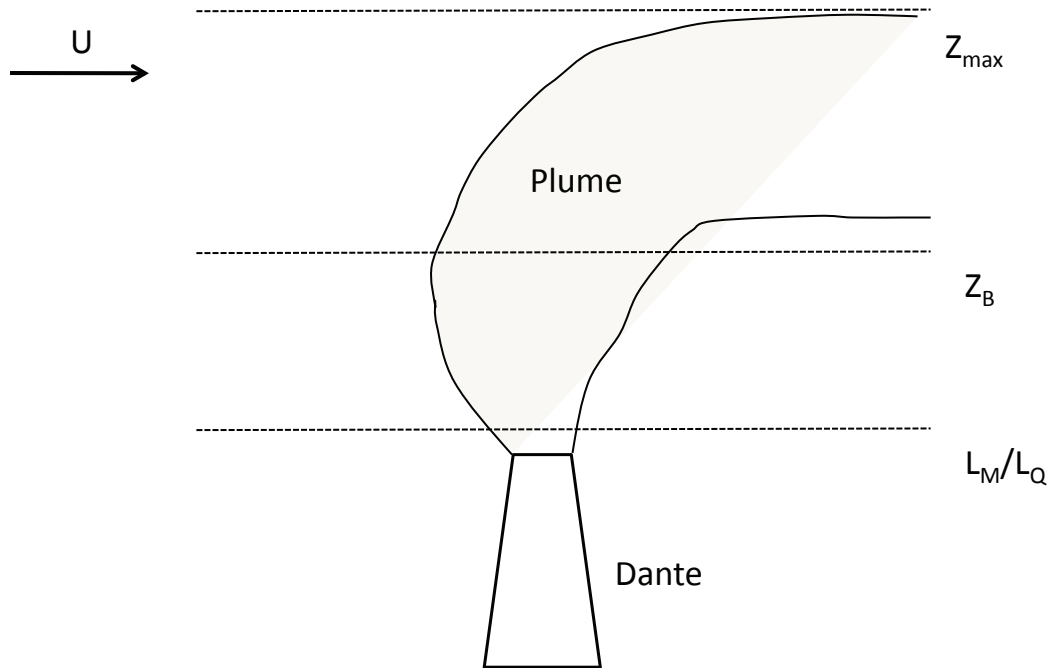


Figure 6.1: Characteristic length scales of a hydrothermal plume in a stratified environment with a uniform horizontal cross-flow.

3.  $z_B = B/U^3$  : for  $z \gg z_B$  (bent over zone), the plume is bent horizontally under the effect of the horizontal cross-flow; for  $z \ll z_B$  (vertical zone), the horizontal current has not yet imposed an appreciable effect on the plume and the plume still maintains its vertical shape.
4.  $z_{max} = 3.8B^{1/4}/N^{3/4}$  (Turner and Campbell, 1987): Terminal height of the plume in a stratified quiescent environment in which  $N = \sqrt{\frac{-g}{\rho_{a0}} \frac{d\rho_a}{dz}}$  is the BruntVäisälä frequency of the ambient water column.

In the case of Dante, the initial temperature measured using Alvin's high temperature probe is  $T_0 = 327.5^\circ\text{C}$  and the initial salinity is  $S_0 = 29.3$  (Butterfield et al., 1994). Dante has approximately 10 major high temperature vents (Delaney et al., 1992) (see Table 2.2) from which the plumes coalesce into a single integrated plume at several meters above the

edifice (based on the video records from Jason and the SM2000 images). The average radius of the major orifices is 3 cm and the exit velocity of the black smoker vents is  $W \sim 0.5$  m/s (measured by Dr. L. N. Germanovich (Georgia Institute of Technology)). The total cross sectional area of the orifices is then used to represent the base cross-section of the integrated plume of which the radius  $b(0) \sim 10$  cm ( $D = 20$  cm).

The horizontal cross-flow is  $U \sim 5$  cm/s (mean value of the northward flow measured by R. Thomson in 2001 within the central axial valley). The stratification is calculated by a linear regression on the CTD data from the background seawater vertical cast during cruise AT15-36 in 2008. The vertical structure of ambient temperature, salinity and density (as shown in Figure 6.2), are then,

$$T (\text{°C}) = 1.673 + 6.666 \times 10^{-4}z, \quad (6.6)$$

$$S (\text{pss} - 78) = 34.612 - 1.135 \times 10^{-4}z, \quad (6.7)$$

$$\rho_a (\text{kg/m}^3) = 1027.685 - 1.247 \times 10^{-4}z, \quad (6.8)$$

where  $z$  is the height above the edifice of Dante (at a depth of 2175 m). Therefore,  $d\rho_a/dz = -1.247 \times 10^{-4}$  kg/m<sup>4</sup> and according to equation (6.4),

$$\frac{d\epsilon}{dz} = -\frac{1}{\rho_{a0}} \frac{d\rho_a}{dz} = 1.213 \times 10^{-7} \text{ m}^{-1} \quad (6.9)$$

and

$$N = \sqrt{gd\epsilon/dz} = 0.0011 \text{ s}^{-1}. \quad (6.10)$$

According to Bischoff and Rosenbauer (1985), density of seawater with 3.2% NaCl at pressure 220 bars and temperature 350 °C is 667 kg/m<sup>3</sup>, which can be regarded as the density of the plume at the orifice ( $\rho_0$ ). Substituting  $T_0$ ,  $T_{a0}$ ,  $D$ ,  $\rho_{a0}$  and  $W$  into equation (6.2) to (6.5) gives

$$Q = 0.0157 \text{ m}^3/\text{s},$$

$$M = 0.0079 \text{ m}^4/\text{s}^2,$$

$$B = 0.0050 \text{ m}^4/\text{s}^3.$$

From these values, characteristic length scales  $L_Q$ ,  $L_M$  and  $z_{max}$  are calculated as follows,

$$L_Q = 0.1772 \text{ m}$$

$$L_M = 0.3725 \text{ m}$$

$$z_B = 40.1257 \text{ m}$$

$$z_{max} = 168.521 \text{ m}$$

$L_M \approx L_Q$  indicates that the plume becomes solely buoyancy driven right after it reaches stationary state. It needs to be noted that, the terminal height  $z_{max}$  calculated here may not be an accurate estimation due to the omission of the ambient horizontal cross-flow which can reduce the terminal height of a plume (Rona et al., 2006). Furthermore, the vertical recirculation induced by the confinement of topography (so called ‘filling box effect’ Baines and Turner (1969)) as well as the rotation of the plume (Helfrich and Speer, 1995) can increase the terminal height of a plume. In contrast,  $z_B$  calculated here is likely an overestimate due to the omission of ambient stratification. With the existence of ambient stratification, a hydrothermal plume will continue entraining ambient sea water and carry it upward against the ambient stratification. In such a way, the plume will slow down and bend over more quickly than in an environment with a homogeneous density distribution.

From these characteristic length scales, at 20 m above the orifice (where the acoustic scintillation measurement was conducted), the plume becomes purely buoyancy driven ( $20 \text{ m} \gg L_M$ ) but still maintains a vertical shape ( $20 \text{ m} < z_B$ ) while the turbulence within plume reaches stationary decay ( $20 \text{ m} \gg L_Q$ ).

### 6.3 GOVERNING EQUATIONS OF THE INTEGRAL MODEL

The integral model is developed based on the conservation equations of mass, momentum, density deficit and dissolved tracers. Fundamental assumptions that are made during the derivation are listed as follows:

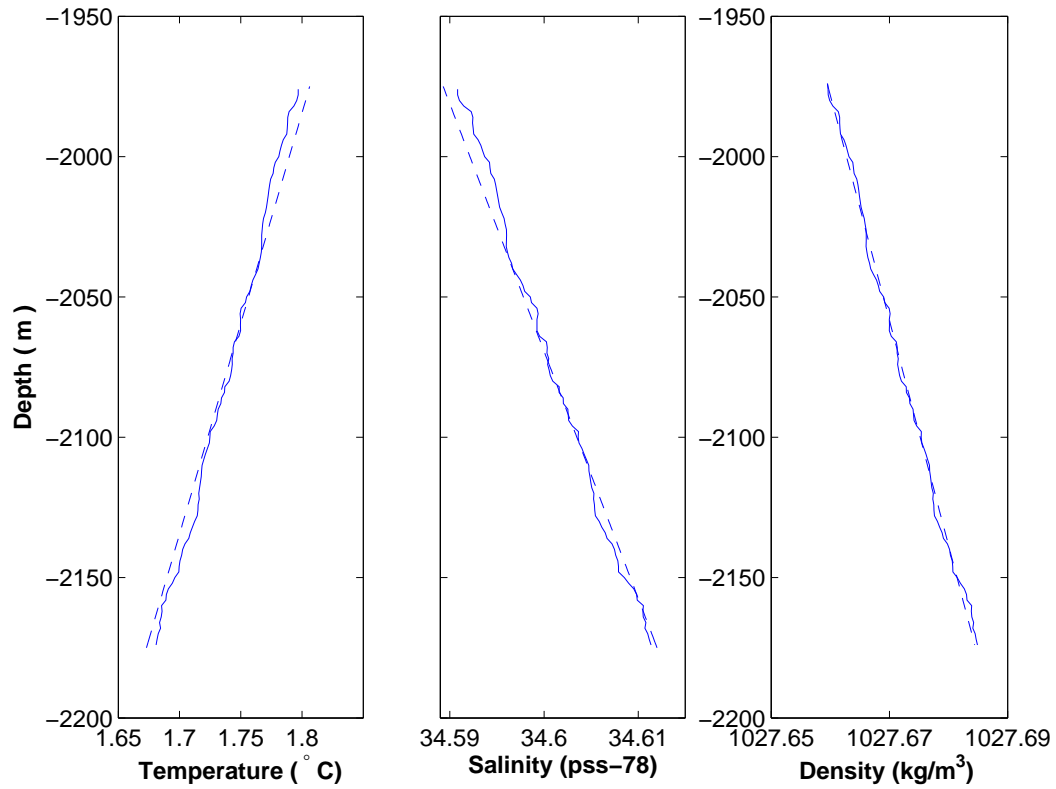


Figure 6.2: Linear fits performed on the ambient temperature, salinity and density measured from CTD cast AT1536001. The solid lines are the CTD data while the dashed lines are the linear fits shown in equations (6.6) to (6.8).

1. Within the range of variation, the density of the fluid is assumed to be a linear function of salinity and temperature above the reference level.
2. The flow is fully turbulent and molecular transport can be neglected (molecular viscosity and diffusion are neglected). This assumption is valid as the Reynolds number ( $WL/\nu$ ) at the orifice of a typical high temperature focused vent (diameter of 6 cm and exit velocity of 0.5 m/s) on Dante reaches  $3 \times 10^4$ .
3. Axial turbulent transport is small compared with axial convective transport. According to Papanicolaou and List (1988), turbulence adds approximately 16% to the specific momentum transport. For this reason, turbulent fluxes can be ignored.
4. The curvature of the plume's trajectory is small.
5. The mean properties of the plume are axisymmetric.
6. The velocity and dissolved tracer concentration profiles are a similar Gaussian function at all cross sections normal to the plume's axis within the region  $z \gg L_Q$  (self-similarity).
7. The Taylor entrainment hypothesis is applied, which relates the inflow velocity at the edge of the plume to the axial velocity within the plume and to the ambient cross-flow.
8. The plume is in steady state. As will be shown, this assumption is valid because the rise-time (the time taken by the plume to reach its terminal height) is much shorter than the dominant tidal period.

A schematic plot of a plume in a uniform cross-flow is shown in Figure 6.3, in which a curvilinear coordinate system is used where  $s$  is the axial distance above the orifice along the plume's trajectory and  $r$  is the radial distance away from the axis in a perpendicular cross-section. In addition,  $U_s$  is the axial velocity of the plume,  $U_a$  is the ambient horizontal cross-flow,  $U_0$  is the plume's exit velocity and  $U_p(s)$  is the plume's residual axial velocity

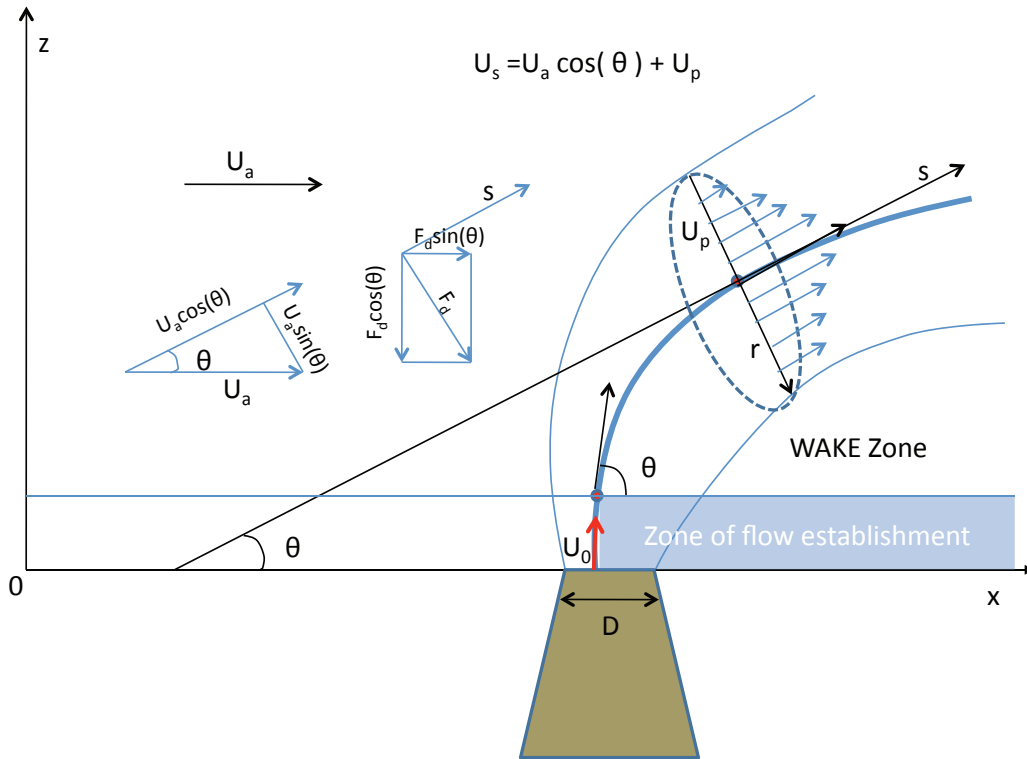


Figure 6.3: A hydrothermal plume is a stratified environment with uniform horizontal flow.

( $U_p = U_s - U_a \cos \theta$ ). The diameter of the orifice is  $D$  and  $F_d$  is the drag force imposed by the horizontal flow on the plume and acts perpendicular to the plume's axis (as will be discussed).

The conservation of mass for the plume is

$$\frac{\partial \rho}{\partial t} + \frac{\partial \rho U}{\partial x} + \frac{\partial \rho W}{\partial z} = 0, \quad (6.11)$$

where  $U$  and  $W$  are the horizontal and vertical components of the velocity vector  $\mathbf{U}$  (the component in  $y$ -direction  $V$  is assumed to be zero). A Reynold's decomposition on the flow ( $U$ ,  $W$ ), density ( $\rho$ ) and reduced pressure ( $P$ ) of the plume, in terms of a time averaged mean (overbar) and turbulent quantity (prime), is defined as

$$U = \bar{U} + u',$$

$$W = \overline{W} + w',$$

$$\rho = \overline{\rho} + \rho'.$$

$$P = \overline{P} + p'$$

Substituting these parameters and then time-averaging equation (6.11) gives

$$\frac{\partial \overline{\rho U}}{\partial x} + \frac{\partial \overline{\rho W}}{\partial z} = 0. \quad (6.12)$$

The turbulent fluxes are negligible and it is assumed that the plume is in steady state. Because the plume is axisymmetric, equation (6.12) is transformed into cylindrical coordinates

$$\frac{1}{r} \frac{\partial}{\partial r}(r \overline{\rho U}) + \frac{\partial \overline{\rho W}}{\partial z} = 0. \quad (6.13)$$

Multiplying by  $2\pi r$  and integrating along the plume's radial cross section gives

$$\int_0^{b(z)} \frac{\partial}{\partial r}(2\pi r \overline{\rho U}) dr = - \int_0^{b(z)} \frac{\partial}{\partial z} 2\pi r \overline{\rho W} dr. \quad (6.14)$$

Applying Leibniz integral rule gives

$$\frac{d}{dz} \int_0^{b(z)} 2\pi r \overline{\rho W} dr = -2\pi r \overline{\rho U}|_{r=b(z)} + \frac{db(z)}{dz} 2\pi r \overline{\rho W}|_{r=b(z)}, \quad (6.15)$$

The second term on the right hand side goes to zero because the mean vertical velocity ( $\overline{W}$ ) evaluated at  $r = b(z)$  is at the edge of the plume where ambient water starts, and thus  $\overline{W}|_{r=b(z)} = 0$ . Equation (6.15) can be further transformed into a curvilinear coordinate system shown in Figure 6.3, assuming small curvatures and the following geometric relationship,

$$\begin{aligned} \sin \theta &= dz/ds \\ \frac{d}{dz} &= \frac{d}{ds} \frac{ds}{dz} = \frac{1}{\sin \theta} \frac{d}{ds}, \\ \overline{W} &= U_s \sin \theta. \end{aligned}$$

Thus, the vertical distance  $z$  can be replaced by an axial distance  $s$  and  $\overline{W}$  can be replaced by axial velocity  $U_s$  giving

$$\frac{d}{ds} \int_0^{b(s)} 2\pi r \overline{\rho U}_s dr = -2\pi r \overline{\rho U}|_{r=b(s)}, \quad (6.16)$$

in which the left hand side is the axial gradient of the mass transport passing the cross-section perpendicular to the plume's axis. The right hand side represents the entrainment from the ambient environment where  $\bar{\rho}\bar{U}|_{r=b(s)}$  represents the horizontal mass flux through the perimeter of the plume toward the center.

The conservation of vertical momentum (per unit volume) as defined by the Navier-Stokes equation, is

$$\frac{\partial}{\partial t}\rho W + \mathbf{U} \cdot \nabla \rho W = -\frac{\partial P}{\partial z} + g(\rho_a - \rho) + \mu \nabla^2 \rho W \quad (6.17)$$

where the terms on the right hand side are the reduced pressure gradient, buoyancy and viscous forces. Using the Reynold's decomposition listed previously and time-averaging gives:

$$\frac{\partial}{\partial x}(\bar{\rho}\bar{U}\bar{W}) + \frac{\partial}{\partial z}\bar{\rho}\bar{W}^2 = -\frac{\partial \bar{P}}{\partial z} + (\rho_a - \bar{\rho})g. \quad (6.18)$$

Note that the turbulent fluxes and viscous effects have been omitted and steady state is assumed. Because the plume is axisymmetric, equation (6.18) is transformed into cylindrical coordinates

$$\frac{\partial}{\partial z}\bar{\rho}\bar{W}^2 + \frac{1}{r}\frac{\partial}{\partial r}r\bar{\rho}\bar{U}\bar{W} = -\frac{\partial \bar{P}}{\partial z} + g(\rho_a - \bar{\rho}) \quad (6.19)$$

as previously done. Multiplying by  $2\pi r$  and integrating along the plume's radial cross section gives

$$\int_0^{b(z)} 2\pi r \frac{\partial}{\partial z} \bar{\rho}\bar{W}^2 dr + \int_0^{b(z)} 2\pi \frac{\partial}{\partial r} (r\bar{\rho}\bar{U}\bar{W}) dr = \int_0^{b(z)} -2\pi r \frac{\partial \bar{P}}{\partial z} dr + \int_0^{b(z)} 2\pi r g(\rho_a - \bar{\rho}) dr. \quad (6.20)$$

Applying Leibniz integral rule gives

$$\begin{aligned} \frac{d}{dz} \int_0^{b(z)} 2\pi r \bar{\rho}\bar{W}^2 dr &= -2\pi r \bar{\rho}\bar{U}\bar{W}|_{r=b(z)} + \frac{db(z)}{dz} 2\pi r \bar{\rho}\bar{W}^2|_{r=b(z)} \\ &\quad - \int_0^{b(z)} \frac{\partial}{\partial z} (2\pi r \bar{P}) dr + \int_0^{b(z)} 2\pi r g(\rho_a - \bar{\rho}) dr. \end{aligned} \quad (6.21)$$

Transforming into the curvilinear coordinate system and given that  $\bar{W}|_{r=b(z)} = 0$  gives,

$$\frac{d}{ds} \int_0^{b(s)} 2\pi r \bar{\rho} U_s (U_s \sin \theta) dr = - \int_0^{b(s)} \frac{1}{\sin \theta} \frac{\partial}{\partial s} (2\pi r \bar{P}) dr + \int_0^{b(s)} 2\pi r g(\rho_a - \bar{\rho}) dr. \quad (6.22)$$

Equation (6.22) is the conservation of vertical momentum transport. The left hand side is the change of the transport of vertical momentum along the axial direction. The first term on the right hand side is the pressure gradient force acting along the axis of the plume, and the second tem is the buoyancy force.

The conservation equation for horizontal momentum can be derived in a similar way. The Navier-Stokes equation for the time rate of change of horizontal momentum per unit volume is

$$\frac{\partial \rho U}{\partial t} + \mathbf{U} \cdot \nabla \rho U = -\frac{\partial P}{\partial x} + \mu \nabla^2 \rho U. \quad (6.23)$$

As before, we apply the Reynold's decomposition, time average and then transform to cylindrical coordinates giving,

$$\frac{1}{r} \frac{\partial}{\partial r} (r \bar{\rho} \bar{U}^2) + \frac{\partial}{\partial z} (\bar{\rho} \bar{W} \bar{U}) = -\frac{1}{r} \frac{\partial}{\partial r} (r \bar{P}). \quad (6.24)$$

Recall that steady state is assumed and that molecular viscosity and turbulent fluxes are omitted. Multiplying by  $2\pi r$  and then integrating over the cross sectional area taking into account Leibniz integral rule gives,

$$\frac{d}{dz} \int_0^{b(z)} 2\pi r \bar{\rho} \bar{W} \bar{U} dr = \frac{db(z)}{dz} 2\pi r \bar{\rho} \bar{W} \bar{U}|_{r=b(z)} - 2\pi r \bar{\rho} \bar{U} \bar{U}|_{r=b(z)} - 2\pi r \bar{P}|_{r=b(z)} \quad (6.25)$$

in which the first term on the right hand side goes to zero as  $\bar{W}|_{r=b(z)} = 0$ . Transforming equation (6.25) into the curvilinear coordinate system gives

$$\frac{d}{ds} \int_0^{b(s)} 2\pi r \bar{\rho} U_s \bar{U} dr = -2\pi r \bar{\rho} \bar{U} \bar{U}|_{r=b(s)} - 2\pi r \bar{P}|_{r=b(z)}. \quad (6.26)$$

which is the conservation equation of horizontal momentum. In equation (6.26), the left hand side is the change of the axial transport of horizontal momentum along the axial direction. On the right hand side, the first term describes the entrainment (or transport) of ambient horizontal momentum into the plume per unit height since  $\bar{\rho} \bar{U} \bar{U}|_{r=b(s)}$  is the horizontal momentum flux on the boundary of the plume. The last term is the pressure acting on the plume from the ambient ocean.

Using the advection-diffusion equation, the conservation of a dissolved tracer  $C$  is

$$\frac{\partial \rho C}{\partial t} + \mathbf{U} \cdot \nabla \rho C = K_c \nabla^2 \rho C, \quad (6.27)$$

in which  $C$  is for example heat per unit mass ( $c_p T$ ) or salinity (S) defined as grams of salt per kg of water and  $K_c$  is the molecular diffusion coefficient for the tracer. As before the Reynold's decomposition is applied and then time-averaged. Transforming to cylindrical coordinates (turbulent fluxes and molecular diffusion are neglected) gives

$$\frac{1}{r} \frac{\partial}{\partial r} (r \bar{\rho} \bar{U} \bar{C}) + \frac{\partial}{\partial z} (\bar{\rho} \bar{W} \bar{C}) = 0. \quad (6.28)$$

Integrating over the cross sectional area and using the Leibniz integral rule gives

$$\frac{d}{dz} \int_0^{b(z)} 2\pi r (\bar{\rho} \bar{W} \bar{C}) dr = -2\pi r \bar{\rho} \bar{U} \bar{C} |_{r=b(z)} + \frac{db(z)}{dz} 2\pi r \bar{\rho} \bar{W} \bar{C} |_{r=b(z)}, \quad (6.29)$$

in which the last term on the right hand side goes to zero as previously discussed. Transforming equation (6.29) into the curvilinear coordinate system gives

$$\frac{d}{ds} \int_0^{b(s)} 2\pi r (\bar{\rho} U_s \bar{C}) dr = -2\pi r \bar{\rho} \bar{U} \bar{C} |_{r=b(s)} \quad (6.30)$$

The left hand side of equation (6.30) is the change of concentration transport along axial direction while the right hand side describes the entrainment of the tracer from the ambient environment into the plume.

An equation for the transport of dissolved tracer concentration anomalies is obtained by first multiplying equation (6.13) by the ambient dissolved tracer concentration  $C_a$  (which is independent of  $r$ )

$$\frac{\partial (2\pi r \bar{\rho} \bar{U} C_a)}{\partial r} = -\frac{\partial (2\pi r \bar{\rho} \bar{W} C_a)}{\partial z} + \frac{\partial C_a}{\partial z} 2\pi r \bar{\rho} \bar{W}. \quad (6.31)$$

Integrating over the cross sectional area, applying Leibniz integral rule and transforming into curvilinear coordinates gives

$$\frac{d}{ds} \int_0^{b(s)} 2\pi r (\bar{\rho} U_s C_a) dr = -2\pi r \bar{\rho} \bar{U} C_a |_{r=b(s)} + \frac{dC_a}{ds} \int_0^{b(s)} 2\pi r U_s \bar{\rho} dr \quad (6.32)$$

Subtracting (6.32) from (6.30) gives,

$$\frac{d}{ds} \int_0^{b(s)} 2\pi r \bar{\rho} U_s (\bar{C} - C_a) dr = -\frac{dC_a}{ds} \int_0^{b(s)} 2\pi r \bar{\rho} U_s dr \quad (6.33)$$

and noting that  $\bar{C}|_{r=b(s)} = C_a$ .

Replacing  $\bar{C}$ ,  $C_a$  in equation (6.33) with  $\bar{T}$ ,  $T_a$  and  $\bar{S}$ ,  $S_a$  respectively leads to the conservation equations for temperature and salinity anomalies.

$$\frac{d}{ds} \int_0^{b(s)} 2\pi r \bar{\rho} U_s (\bar{T} - T_a) dr = -\frac{dT_a}{ds} \int_0^{b(s)} 2\pi r \bar{\rho} U_s dr. \quad (6.34)$$

$$\frac{d}{ds} \int_0^{b(s)} 2\pi r \bar{\rho} U_s (\bar{S} - S_a) dr = -\frac{dS_a}{ds} \int_0^{b(s)} 2\pi r \bar{\rho} U_s dr. \quad (6.35)$$

The left hand side represents the change of tracer transport along the axial direction and the right hand side represents the axial advective transport of the ambient stratification.

Multiplying (6.34) and (6.35) with  $-\alpha_t$  (thermal expansion coefficient) and  $\beta_s$  (haline contraction coefficient) respectively and summing gives,

$$\begin{aligned} & \frac{d}{ds} \int_0^{b(s)} 2\pi r \bar{\rho} U_s [-\alpha_t (\bar{T} - T_a) + \beta_s (\bar{S} - S_a)] dr = \\ & \alpha_t \frac{dT_a}{ds} \int_0^{b(s)} 2\pi r \bar{\rho} U_s dr - \beta_s \frac{dS_a}{ds} \int_0^{b(s)} 2\pi r \bar{\rho} U_s dr. \end{aligned} \quad (6.36)$$

The linear form of the equation of state, which defines the density deficit between the plume and ambient water, is

$$\frac{\bar{\rho} - \rho_a}{\rho_a} = -\alpha_t (\bar{T} - T_a) + \beta_s (\bar{S} - S_a) \quad (6.37)$$

and between the ambient water and a reference density is,

$$\frac{\rho_a - \rho_{a0}}{\rho_{a0}} = -\alpha_t (\bar{T}_a - T_{a0}) + \beta_s (\bar{S}_a - S_{a0}). \quad (6.38)$$

where  $\alpha_t = -\frac{1}{\rho_{a0}} \frac{\partial \rho_a}{\partial T_a} = -\frac{1}{\rho_0} \frac{\partial \rho}{\partial T}$  and  $\beta_s = \frac{1}{\rho_{a0}} \frac{\partial \rho_a}{\partial S_a} = \frac{1}{\rho_a} \frac{\partial \rho}{\partial S}$ . Taking the derivative of equation (6.38) with respect to  $s$  gives

$$\frac{1}{\rho_{a0}} \frac{d\rho_a}{ds} = -\alpha_t \frac{dT_a}{ds} + \beta_s \frac{dS_a}{ds}. \quad (6.39)$$

Substituting equation (6.37) and (6.39) into equation (6.36) gives

$$\frac{d}{ds} \int_0^{b(s)} \frac{2\pi r \bar{\rho} U_s (\bar{\rho} - \rho_a)}{\rho_a} dr = -\frac{1}{\rho_{a0}} \frac{d\rho_a}{ds} \int_0^{b(s)} 2\pi r \bar{\rho} U_s dr. \quad (6.40)$$

Assuming a linear stratification of the ambient environment

$$\rho_a = \rho_{a0}(1 - \epsilon(s)), \quad (6.41)$$

then

$$\frac{d\rho_a}{ds} = -\rho_{a0} \frac{d\epsilon(s)}{ds}. \quad (6.42)$$

Substituting equation (6.42) into equation (6.40) and letting  $\eta = \rho_a - \bar{\rho}$  gives

$$\frac{d}{ds} \int_0^{b(s)} \frac{2\pi r \bar{\rho} U_s \eta}{\rho_a} dr = -\frac{d\epsilon(s)}{ds} \int_0^{b(s)} 2\pi r \bar{\rho} U_s dr. \quad (6.43)$$

which is the conservation equation for density deficit. This equation states that any changes along the plume's axis is due to the axial advection.

Thus, the conservation equations for mass, vertical and horizontal momentum, temperature and salinity anomalies as well as density deficit have been derived (see equations (6.16), (6.22), (6.26), (6.34), (6.35) and (6.43) respectively).

#### 6.4 SIMPLIFYING THE CONSERVATION EQUATIONS

The conservation equations given above can be simplified using Taylor's entrainment hypothesis given in equation (6.1). Equation (6.16) can then be parameterized as

$$\frac{d}{ds} \int_0^{b(s)} 2\pi r \bar{\rho} U_s dr = 2\pi b(s) \rho_a E \quad (6.44)$$

where  $E$  is the entrainment velocity and for the case of no cross-flows  $E = \alpha U_p$  where  $\alpha$  is the entrainment coefficient (typically  $\sim 0.1$ ).

According to Devenish et al. (2010), Webster and Thomson (2002) and Hoult and Weil (1972), the entrainment velocity should include the relative velocity components tangential and normal to the plume's axis when cross-flows exist. Therefore, the entrainment velocity  $E$  should be written as a function of both the relative velocity components:  $E = E(\alpha U_p, \beta U_\perp)$ , in which  $\alpha$  and  $\beta$  are the entrainment coefficients in the tangential and normal directions

respectively. According to Figure 6.3,

$$U_{\perp} = U_a \sin \theta \quad (6.45)$$

$$U_p = U_s - U_a \cos \theta \quad (6.46)$$

A linear additive form of the entrainment velocity can be applied following Webster and Thomson (2002) and Hoult and Weil (1972),

$$E = \alpha U_p + \beta U_{\perp} \quad (6.47)$$

In this context the ambient cross flow ‘blows’ water into the plume and the plume itself ‘breathes’ water in. With this entrainment velocity, the conservation equation for mass can be rewritten as

$$\frac{d}{ds} \int_0^{b(s)} 2\pi r \bar{\rho} U_s dr = 2\pi b(s) \rho_a(s) E. \quad (6.48)$$

According to Fan (1967), the pressure terms in the conservation equations for momentum can be represented by a drag force  $F_D$  perpendicular to the plume’s axis (see Figure 6.3), which is given by Webster and Thomson (2002) as

$$F_D = \pi b(s) \rho_a C_d (U_a \sin \theta)^2, \quad (6.49)$$

where the velocity component ( $U_a \sin \theta$ ) is perpendicular to the plume’s axis on the boundary and  $C_d$  is the drag coefficient.

The conservation equations for vertical and horizontal momentum (equations (6.22) and (6.26)) can be rewritten respectively as,

$$\frac{d}{ds} \int_0^{b(s)} 2\pi r \bar{\rho} U_s (U_s \sin \theta) dr = \int_0^{b(s)} 2\pi r g \eta dr - F_D \cos \theta \quad (6.50)$$

and

$$\frac{d}{ds} \int_0^{b(s)} 2\pi r \bar{\rho} U_s (U_s \cos \theta) dr = 2\pi \rho_a b(s) U_a E + F_D \sin \theta \quad (6.51)$$

where  $\bar{U} = U_s \cos \theta$ .

In summary, the conservation equations based on the Taylor's entrainment hypothesis can be listed as follows

$$\begin{aligned}
\frac{d}{ds} \int_0^{b(s)} 2\pi r \bar{\rho} U_s dr &= 2\pi b(s) \rho_a E && \text{Mass,} \\
\frac{d}{ds} \int_0^{b(s)} 2\pi r \bar{\rho} U_s (U_s \sin \theta) dr &= \int_0^{b(s)} 2\pi r g \eta dr - F_D \cos \theta && \text{Vertical Momentum,} \\
\frac{d}{ds} \int_0^{b(s)} 2\pi r \bar{\rho} U_s (U_s \cos \theta) dr &= 2\pi b(s) U_a \rho_a E + F_D \sin \theta && \text{Horizontal Momentum,} \\
\frac{d}{ds} \int_0^{b(s)} 2\pi r \bar{\rho} U_s (\bar{T} - T_a) dr &= -\frac{dT_a}{ds} \int_0^{b(s)} 2\pi r \bar{\rho} U_s dr && \text{Temperature Anomaly,} \\
\frac{d}{ds} \int_0^{b(s)} 2\pi r \bar{\rho} U_s (\bar{S} - S_a) dr &= -\frac{dS_a}{ds} \int_0^{b(s)} 2\pi r \bar{\rho} U_s dr && \text{Salinity Anomaly,} \\
\frac{d}{ds} \int_0^{b(s)} \frac{2\pi r \bar{\rho} U_s \eta}{\rho_a} dr &= -\frac{d\epsilon(s)}{ds} \int_0^{b(s)} 2\pi r \bar{\rho} U_s dr && \text{Density Deficit.}
\end{aligned}$$

Together with the geometric equations

$$\frac{dx}{ds} = \cos \theta, \quad (6.52)$$

$$\frac{dz}{ds} = \sin \theta, \quad (6.53)$$

there are eight equations with eight unknown variables ( $\theta$ ,  $U_s$ ,  $\eta$ ,  $T$ ,  $S$ ,  $x$ ,  $z$  and  $b(s)$ ).

Moreover, the conservation equations shown above can be further simplified based on the 'self-similarity' assumption which states that the radial distribution profiles of the plume's mean properties all have similar Gaussian distributions within the region where  $z \gg L_Q$  (way above the flow establishment zone). A circular cross-section is used due to the axisymmetric assumption and the radial profiles can thus be written as

$$U_s = U_a \cos \theta + U_m \exp(-r^2/b_u^2), \quad (6.54)$$

$$\bar{C} - C_a = C_m \exp(-r^2/(1.44b_u^2)), \quad (6.55)$$

$$\rho_a - \bar{\rho} = \eta = \eta_m \exp(-r^2/(1.44b_u^2)). \quad (6.56)$$

in which  $U_m$ ,  $C_m$  and  $\eta_m$  are the maximum values of the mean properties at the plume's axis ( $r = 0$ ) and are functions of  $z$ . The radius  $b_u$  is defined as the distance between the point where the axial velocity  $U_s$  decreases to  $1/e$  of its maximum at the plume's axis. Based

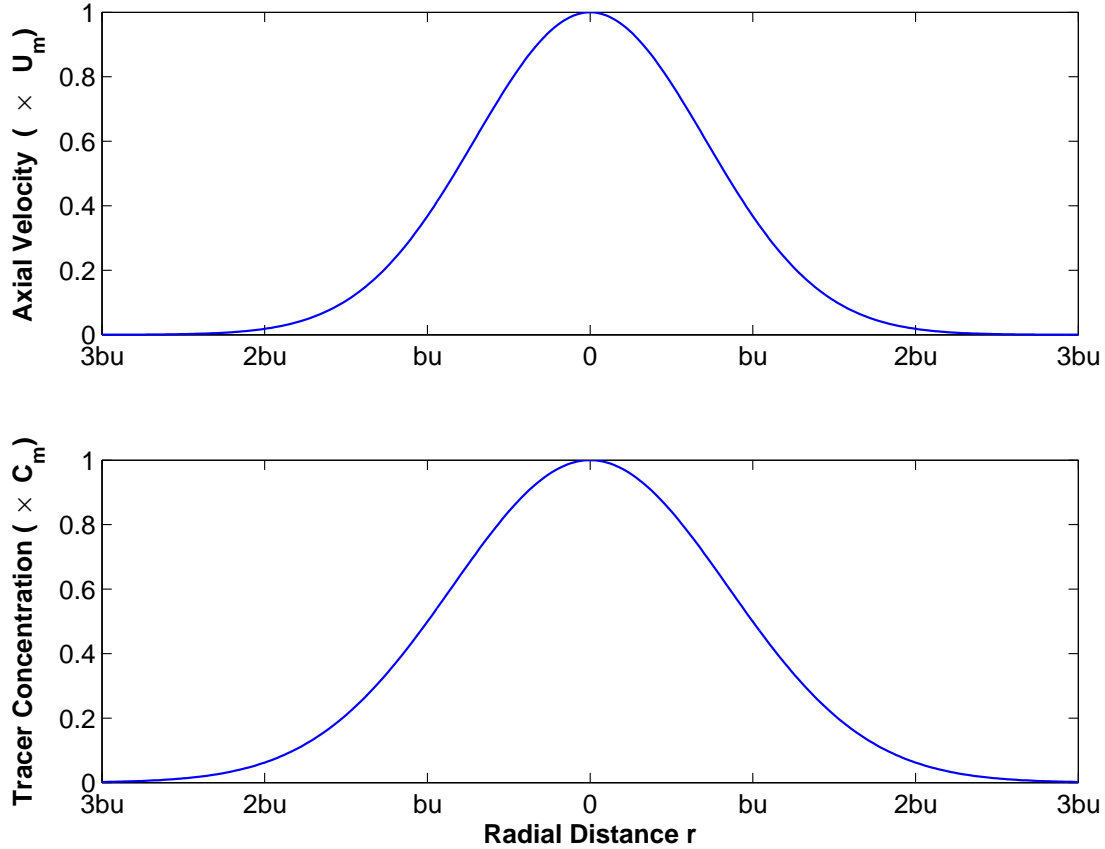


Figure 6.4: Radial distribution profiles for the plume velocity and tracer concentration.

on the results of laboratory experiments generalized by Papanicolaou and List (1988), the radius of the dissolved tracer concentrations is greater than that of the axial velocity and the ratio of proportionality is 1.2. The density deficit is assumed to have an identical distribution profile to that of the dissolved tracer concentrations. Figure 6.4 shows the radial distribution profiles of axial velocity and dissolved tracer concentrations.

Substituting the radial distributions of  $U_s$  and  $\eta$  into the conservation equation of mass, momentum, temperature and salinity anomalies as well as density deficit and calculating the integrals gives,

$$\frac{d}{ds} \left\{ b_u^2 [\rho_a (0.432U_m + U_a \cos \theta) - \eta_m (0.540U_a \cos \theta + 0.285U_m)] \right\} = \sqrt{2} b_u \rho_a E$$

Mass (6.57)

$$\begin{aligned} & \frac{d}{ds} \left\{ b_u^2 \sin \theta [\rho_a (U_a^2 \cos^2 \theta + 0.245 U_m^2 + 0.865 U_a U_m \cos \theta) \right. \\ & \quad \left. - \eta_m (0.540 U_a^2 \cos^2 \theta + 0.57 U_a U_m \cos \theta + 0.185 U_m^2)] \right\} \\ & = 0.540 b_u^2 g \eta_m - \frac{F_D \cos \theta}{2\pi} \end{aligned}$$

Vertical Momentum (6.58)

$$\begin{aligned} & \frac{d}{ds} \left\{ b_u^2 \cos \theta [\rho_a (U_a^2 \cos^2 \theta + 0.245 U_m^2 + 0.865 U_a U_m \cos \theta) \right. \\ & \quad \left. - \eta_m (0.540 U_a^2 \cos^2 \theta + 0.57 U_a U_m \cos \theta + 0.185 U_m^2)] \right\} \\ & = \sqrt{2} b_u \rho_a U_a E + \frac{F_D \sin \theta}{2\pi} \end{aligned}$$

Horizontal Momentum (6.59)

$$\begin{aligned} & \frac{d}{ds} \left\{ T_m b_u^2 [\rho_a (0.285 U_m + 0.540 U_a \cos \theta) - \eta_m (0.388 U_a \cos \theta + 0.208 U_m)] \right\} \\ & = -\frac{dT_a}{ds} b_u^2 [\rho_a (0.432 U_m + U_a \cos \theta) - \eta_m (0.540 U_a \cos \theta + 0.285 U_m)] \end{aligned}$$

Temperature Anomaly (6.60)

$$\begin{aligned} & \frac{d}{ds} \left\{ S_m b_u^2 [\rho_a (0.285 U_m + 0.540 U_a \cos \theta) - \eta_m (0.388 U_a \cos \theta + 0.208 U_m)] \right\} \\ & = -\frac{dS_a}{ds} b_u^2 [\rho_a (0.432 U_m + U_a \cos \theta) - \eta_m (0.540 U_a \cos \theta + 0.285 U_m)] \end{aligned}$$

Salinity Anomaly (6.61)

$$\begin{aligned} & \frac{d}{ds} \left\{ \frac{\eta_m b_u^2}{\rho_a} [\rho_a (0.285 U_m + 0.540 U_a \cos \theta) - \eta_m (0.338 U_a \cos \theta + 0.208 U_m)] \right\} \\ & = -\frac{d\epsilon(s)}{ds} b_u^2 [\rho_a (0.432 U_m + U_a \cos \theta) - \eta_m (0.540 U_a \cos \theta + 0.285 U_m)] \end{aligned}$$

Density Deficit (6.62)

In deriving the equations above, the radius of the plume is assumed to be  $b(s) \approx \sqrt{2} b_u$ . Equations (6.57) to (6.62) are final forms of the simplified conservation equations based on the Taylor's entrainment hypothesis and the self-similarity assumption.

## 6.5 NUMERICAL SOLUTIONS

In order to solve the simplified set of conservation equations, they need to be transformed into forms suitable for numerical calculation. By expanding the derivatives on the left hand sides, the equations are transformed into the following matrix,

$$\begin{aligned}
b_1 \frac{db_u}{ds} + u_1 \frac{dU_m}{ds} + \lambda_1 \frac{d\theta}{ds} + t_1 \frac{dT_m}{ds} + s_1 \frac{dS_m}{ds} + \kappa_1 \frac{d\eta_m}{ds} &= R1 && \text{Mass} \\
b_2 \frac{db_u}{ds} + u_2 \frac{dU_m}{ds} + \lambda_2 \frac{d\theta}{ds} + t_2 \frac{dT_m}{ds} + s_2 \frac{dS_m}{ds} + \kappa_2 \frac{d\eta_m}{ds} &= R2 && \text{Vertical Momentum} \\
b_3 \frac{db_u}{ds} + u_3 \frac{dU_m}{ds} + \lambda_3 \frac{d\theta}{ds} + t_3 \frac{dT_m}{ds} + s_3 \frac{dS_m}{ds} + \kappa_3 \frac{d\eta_m}{ds} &= R3 && \text{Horizontal Momentum} \\
b_4 \frac{db_u}{ds} + u_4 \frac{dU_m}{ds} + \lambda_4 \frac{d\theta}{ds} + t_4 \frac{dT_m}{ds} + s_4 \frac{dS_m}{ds} + \kappa_4 \frac{d\eta_m}{ds} &= R4 && \text{Temperature Anomaly} \\
b_5 \frac{db_u}{ds} + u_5 \frac{dU_m}{ds} + \lambda_5 \frac{d\theta}{ds} + t_5 \frac{dT_m}{ds} + s_5 \frac{dS_m}{ds} + \kappa_5 \frac{d\eta_m}{ds} &= R5 && \text{Salinity Anomaly} \\
b_6 \frac{db_u}{ds} + u_6 \frac{dU_m}{ds} + \lambda_6 \frac{d\theta}{ds} + t_6 \frac{dT_m}{ds} + s_6 \frac{dS_m}{ds} + \kappa_6 \frac{d\eta_m}{ds} &= R6 && \text{density deficit}
\end{aligned}$$

in which  $b_i$ ,  $u_i$ ,  $\lambda_i$ ,  $T_i$ ,  $S_i$  and  $\kappa_i$  ( $i=1:6$ ) are the coefficients of the derivatives of the unknown variables respectively and each of the coefficients are a function of the unknown variables, and  $R_i$  are the corresponding right hand sides of the conservation equations. Appendix A shows the conservation equations expanded out and mathematical representations for  $b_i$ ,  $u_i$ ,  $\lambda_i$ ,  $t_i$ ,  $s_i$ ,  $\kappa_i$  and  $R_i$  ( $i = 1:6$ ).

Let

$$\mathbf{A} = \begin{bmatrix} b_1 & u_1 & \lambda_1 & t_1 & s_1 & \kappa_1 \\ b_2 & u_2 & \lambda_2 & t_2 & s_2 & \kappa_2 \\ b_3 & u_3 & \lambda_3 & t_3 & s_3 & \kappa_3 \\ b_4 & u_4 & \lambda_4 & t_4 & s_4 & \kappa_4 \\ b_5 & u_5 & \lambda_5 & t_5 & s_5 & \kappa_5 \\ b_6 & u_6 & \lambda_6 & t_6 & s_6 & \kappa_6 \end{bmatrix},$$

$$\mathbf{V} = \begin{bmatrix} \frac{db_u}{ds} \\ \frac{dU_m}{ds} \\ \frac{d\theta}{ds} \\ \frac{dT_m}{ds} \\ \frac{dS_m}{ds} \\ \frac{d\eta_m}{ds} \end{bmatrix}$$

and

$$\mathbf{R} = \begin{bmatrix} R_1 \\ R_2 \\ R_3 \\ R_4 \\ R_5 \\ R_6 \end{bmatrix}.$$

The set of conservation equations can then be written in matrix form as,

$$\mathbf{AV} = \mathbf{R} \quad (6.63)$$

and thus

$$\mathbf{V} = \mathbf{A}^{-1}\mathbf{R}. \quad (6.64)$$

A final form suitable for numerical calculation is thus derived by solving the equation above symbolically using MAPLE.

## 6.6 MODEL RESULTS

The Matlab routine ode45 is used to solve the differential equations with an absolute error of  $10^{-9}$ . The initial conditions are

$$b_u(0) = 0.1 \text{ m}$$

$$U_m(0) = 0.5 \text{ m/s}$$

$$\theta(0) = \pi/2$$

$$T_m(0) = \bar{T}_0 - T_{a0} = 324.127^\circ\text{C}$$

$$S_m(0) = \bar{S}_0 - S_{a0} = -5.312 \text{ (pss - 78)}$$

$$\eta_m(0) = \rho_{a0} - \rho_0 = 361 \text{ kg/m}^3$$

and the constant parameters are set following Fan (1967) and Fischer et al. (1979):

$$C_d = 0.01$$

$$\alpha = 0.083$$

$$\beta = 0.5$$

$$U_a = 0.05 \text{ m/s}$$

Figure 6.5 shows the change of the plume's radius  $b(s) \approx 1.2\sqrt{2}b_u(s)$  along the height above its orifice under a uniform horizontal cross-flow of the order of 5 cm/s. According to this figure, the plume's radius increases nonlinearly along the height above the orifice due to the entrainment of the ambient seawater.

Figure 6.6 shows the trajectory of the plume under a uniform horizontal cross-flow of 5 cm/s. The plume bends toward the direction of the flow and is drifted approximately 100 m away from its origin at the height of 120 m. The bending of the plume is caused by the drag force exerted by the horizontal cross-flow on, and the entrainment of the horizontal momentum into the plume.

Figure 6.7 shows the change of the radial-averaged vertical velocity  $\langle W \rangle$  along the height above the orifice ( $\langle W \rangle = \frac{1}{\sqrt{2}b_u} \int_0^{\sqrt{2}b_u} \tilde{W} \exp(-r^2/b_u^2) dr$ ), in which  $\tilde{W}$  is the plume's centerline vertical velocity. As can be seen,  $\langle W \rangle$  decreases exponentially through the plume's ascent due to the loss of buoyancy while mixing with the entrained ambient ocean water and finally reaches zero at roughly 120 m above the orifice. This level can be regarded as the terminal height of the plume where the vertical momentum becomes zero. In addition, the rise-time of the plume (the time taken by the plume to reach its terminal height) is calculated as  $T_{rise} = \int_0^{120} z/W(z) dz = 0.74 \text{ hr}$  which is much shorter than the period of the dominant principal lunar (M2) tide and therefore the plume can be considered steady.

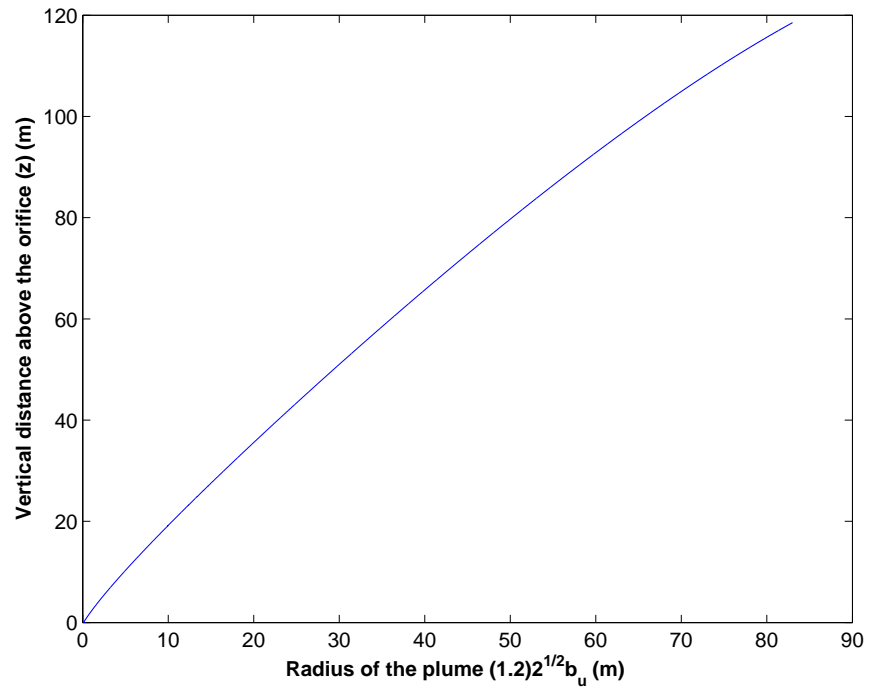


Figure 6.5: Radius of the plume.

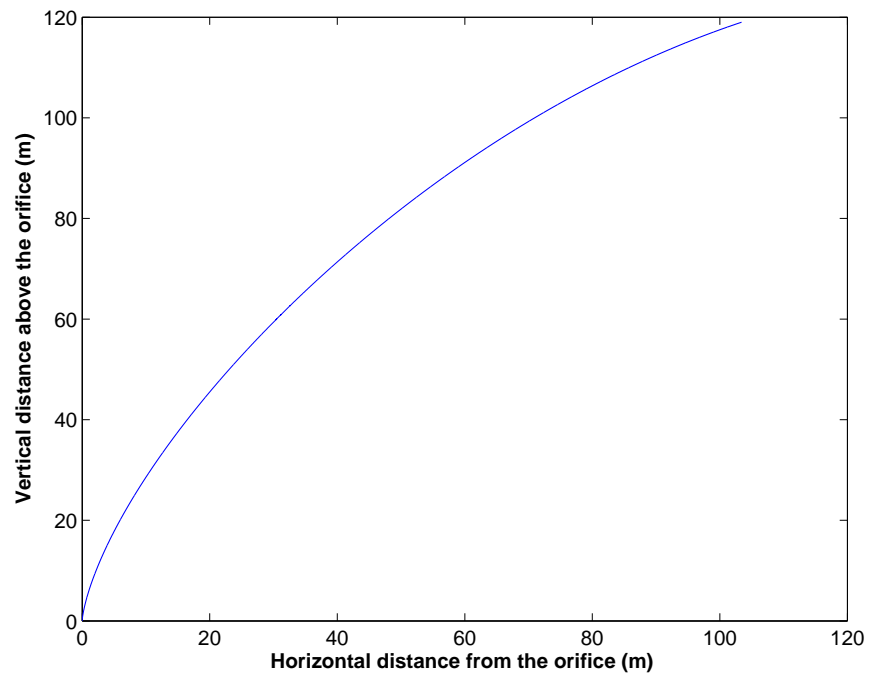


Figure 6.6: Trajectory of the plume.

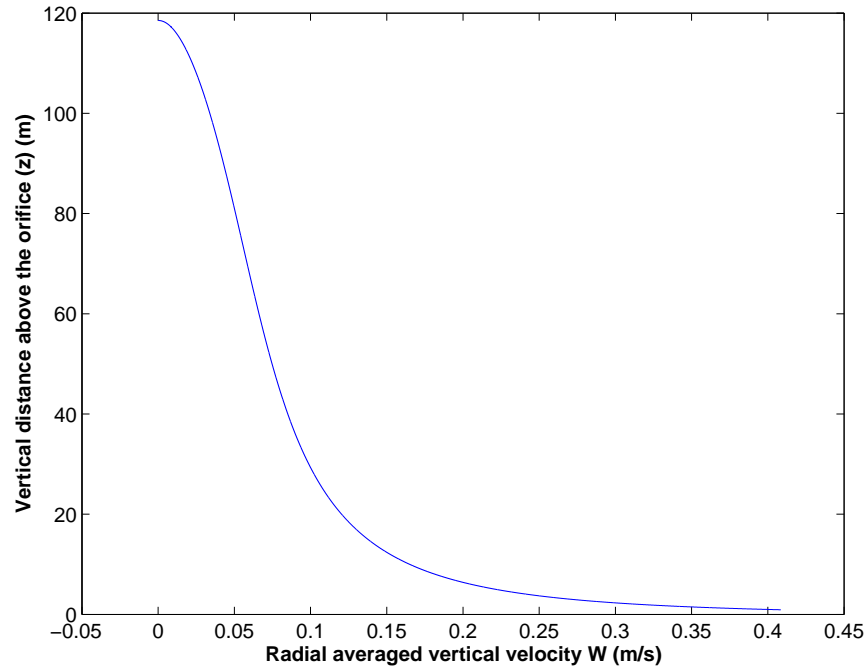


Figure 6.7: Radial averaged vertical velocity of the plume.

Figure 6.8 shows the change of the declination angle (angle between the plume's trajectory and the vertical axis) along the height above the orifice. The declination angle increases exponentially and ultimately reaches  $90^\circ$  at 120 m above. The bending is caused by the horizontal cross-flow which exerts a drag force on and entrains horizontal momentum into the plume. Meanwhile, the horizontal cross-flow also suppresses the vertical velocity of the plume (as will be discussed below) and further enhances the bending.

Figure 6.9 shows the change of the plume's density deficit  $\eta_m$  along the height above the orifice. Unlike  $W$ ,  $\eta_m$  plummets sharply to a value around  $1 \text{ kg/m}^3$  within the initial 10 m rise and then gradually decreases to zero at 100 m above. The negative value after this level indicates the plume has overshoot the neutral-buoyancy level and thus its buoyancy becomes negative.

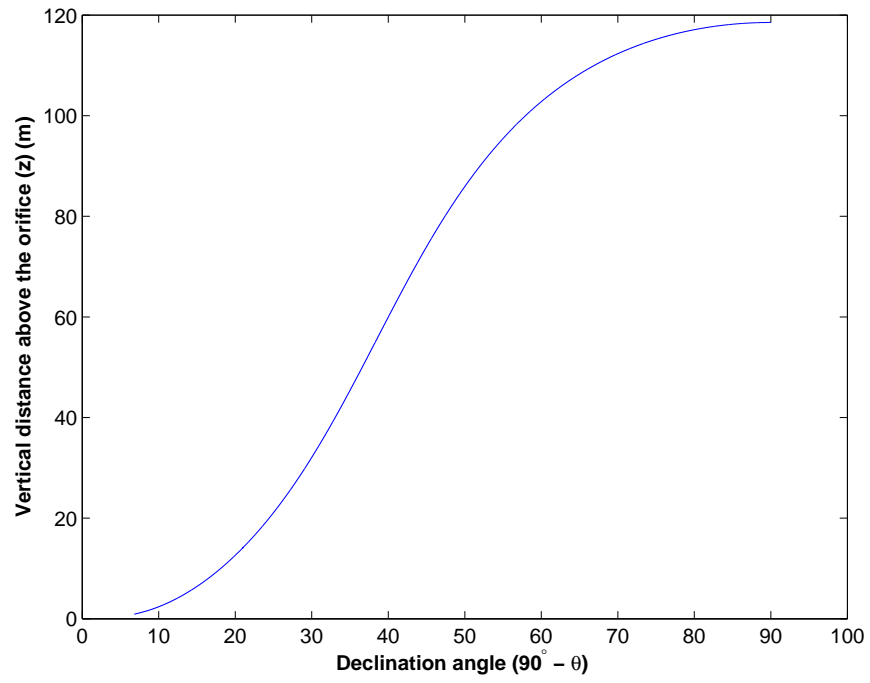


Figure 6.8: Declination angle of the plume's trajectory.

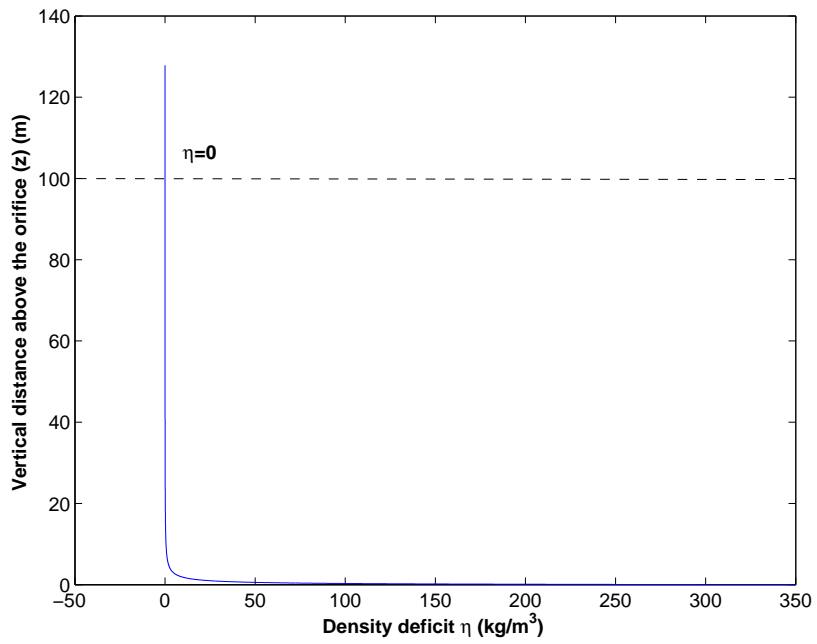


Figure 6.9: Density deficit of the plume.

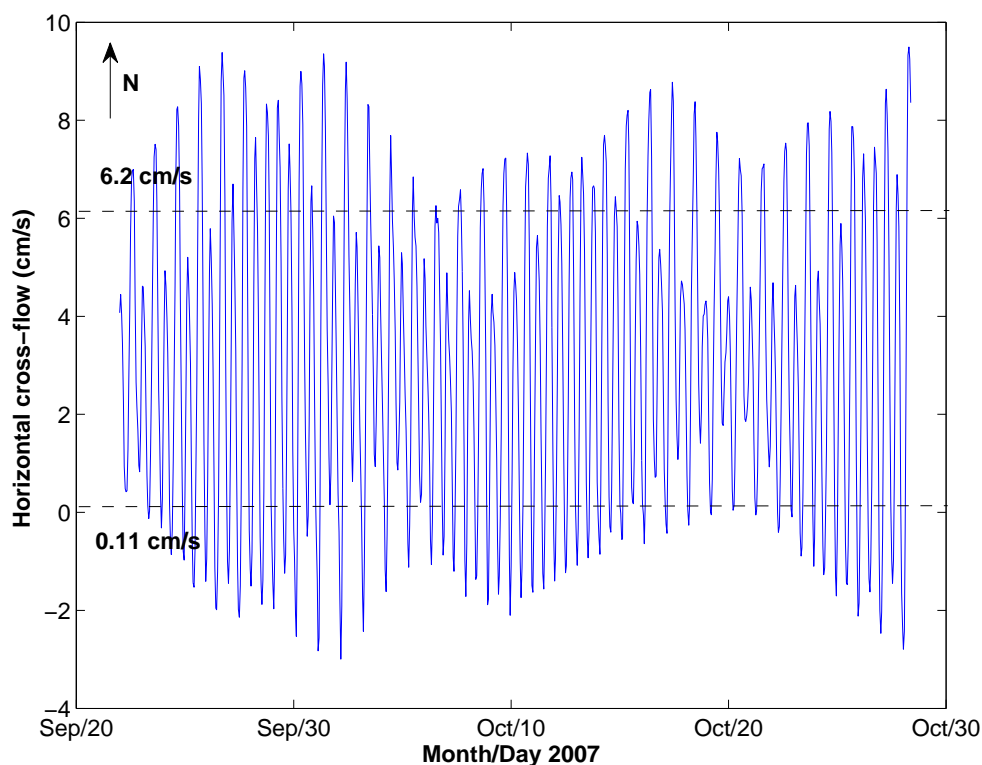


Figure 6.10: Estimated horizontal cross-flow at the time of the acoustic scintillation measurement in 2007. The dashed lines pinpoint one standard deviation above and below the mean value.

## 6.7 COMPARISON WITH EXPERIMENTAL DATA

A comparison between the model and experimental results is made to test the model's validity and accuracy. As is mentioned in Chapter 5, the horizontal cross-flow during the time of the acoustic scintillation measurement can be estimated by adding the mean residual flow ( $\sim 3.14$  cm/s) to the extrapolated tidal currents (see Figure 6.10).

By forcing the model with a horizontal cross-flow varying from 0 to 0.1 m/s, which reflects the range of the fluctuation shown in Figure 6.10, the plume's radial-averaged vertical velocity at 20 m above the orifice is plotted as a function of the horizontal cross-flow in Figure 6.11

with all the other parameters maintained as they were in the previous model run. The plume vertical velocity decreases from 0.2 m/s at zero horizontal cross-flow to 0.09 m/s at 0.1 m/s horizontal cross-flow. Such a significant variation indicates that the horizontal cross-flow has a major effect on the vertical velocity oscillations shown in Figure 4.3. The entrainment of the ambient seawater into the plume is enhanced under a strong horizontal cross-flow, which makes the plume cooler and slower than it is when the horizontal flow is weak. In addition, the bending of the plume caused by the horizontal cross-flow may further decrease the vertical velocity because bending can make the measurement made at 20 m above the orifice further away from the orifice along the plume axis (see Figure 6.12 (a)). Figure 6.12 (b) shows a comparison of the model-estimated vertical velocities of the plume at 20 m above the orifice and at 20 m away from the orifice along the axis as a function of the horizontal cross-flow. The decrease of the vertical velocity caused by the bending is negligible compared with the magnitude of the oscillation observed in the measurement (the maximum in Figure 6.12 (b) is 1.0 cm/s while the range of the oscillation shown in Figure 4.3 reaches 20 cm/s).

In addition to the plume's vertical velocity, the plume's radius can be estimated from the back-scattered sonar images shown in Figure 2.20, according to which, the radius of the plume from Dante at 20 m above the orifice is approximately 7 m. Again, the horizontal cross-flow at the time when the back-scattered sonar image was taken is estimated by adding the mean residual flow of 3.14 cm/s to the extrapolated tidal current. Thus, another model run based on such a horizontal cross-flow is carried out and the predicted radius of the plume is shown in Figure 6.13, in which the radius at 20 m above the orifice is approximately 9.2 m. Note that, the radius of the plume is defined as  $1.2\sqrt{2}b_u$  because, as is discussed in Section 4.2, the lateral profile of the back-scattered intensity within the back-scattered image is supposed to be identical to the profile of the dissolved tracers within the plume, of which the radius is 1.2 times as large as that of the vertical velocity's profile ( $b_u$ ).

In order to test the error induced by the uncertainty of constant parameters employed in the model, several sensitivity tests are conducted. Figure 6.14 shows the radial-averaged

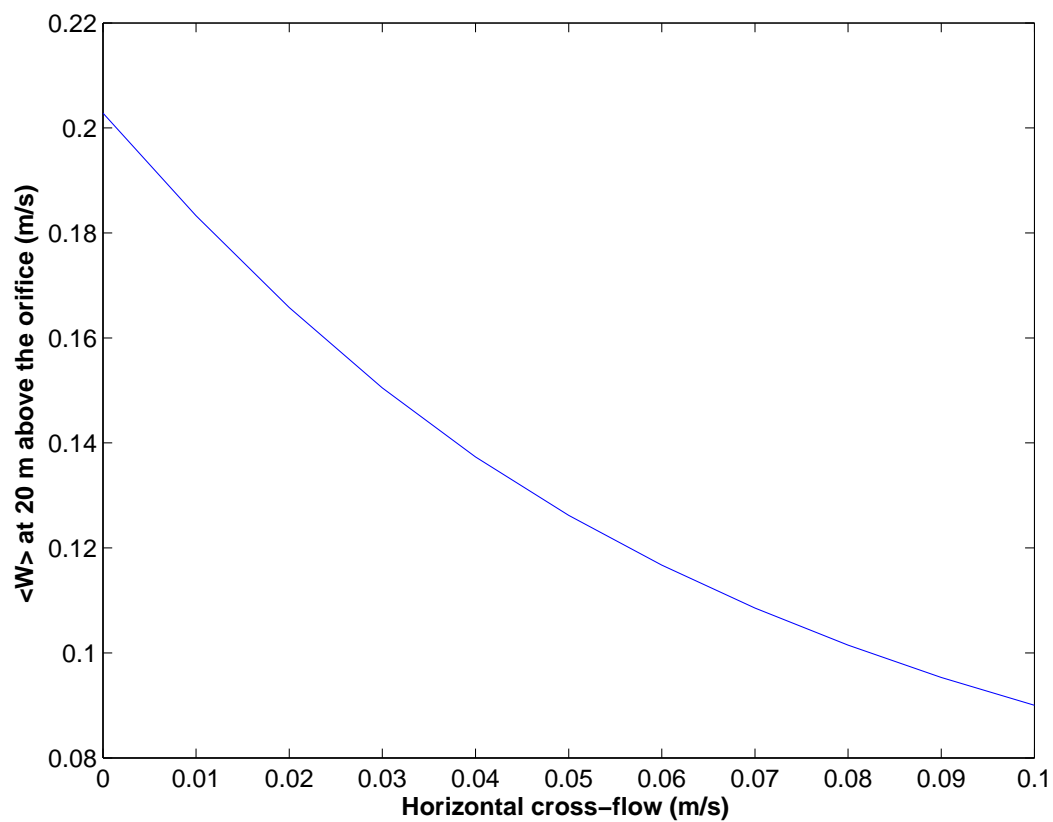


Figure 6.11: The plume's radial-averaged vertical velocity at 20 m above the orifice as a function of the horizontal cross-flow.

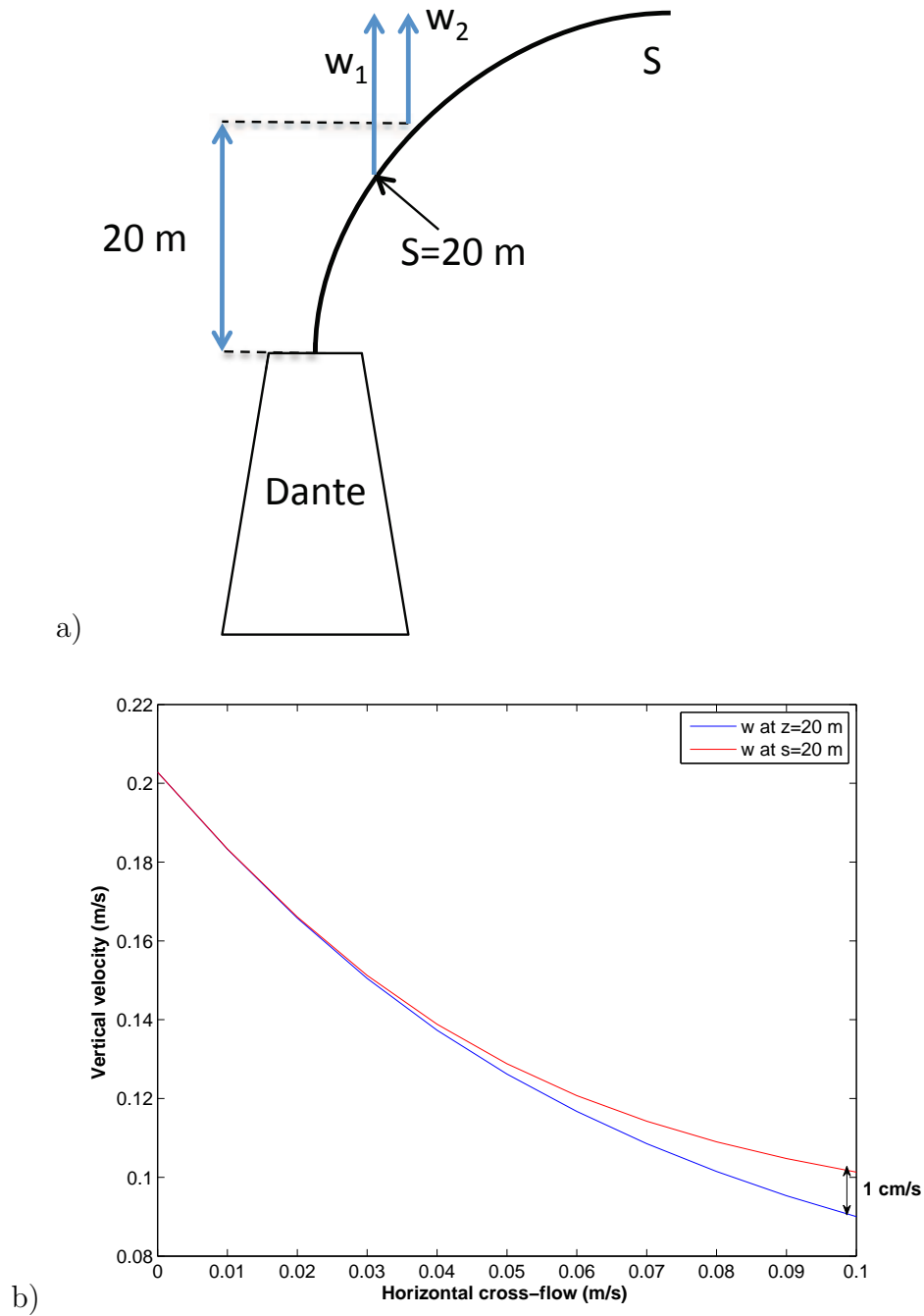


Figure 6.12: (a) The effect of the bending of the plume on the vertical velocity measurement made at 20 m above the orifice.  $S$  is the distance along the plume axis,  $w_1$  is the vertical velocity measured at  $S = 20$  m and  $w_2$  is the vertical velocity measured at 20 m above the orifice. (b) Comparison between the vertical velocity of the plume at 20 m above the orifice and at 20 m away from the orifice along the axis.

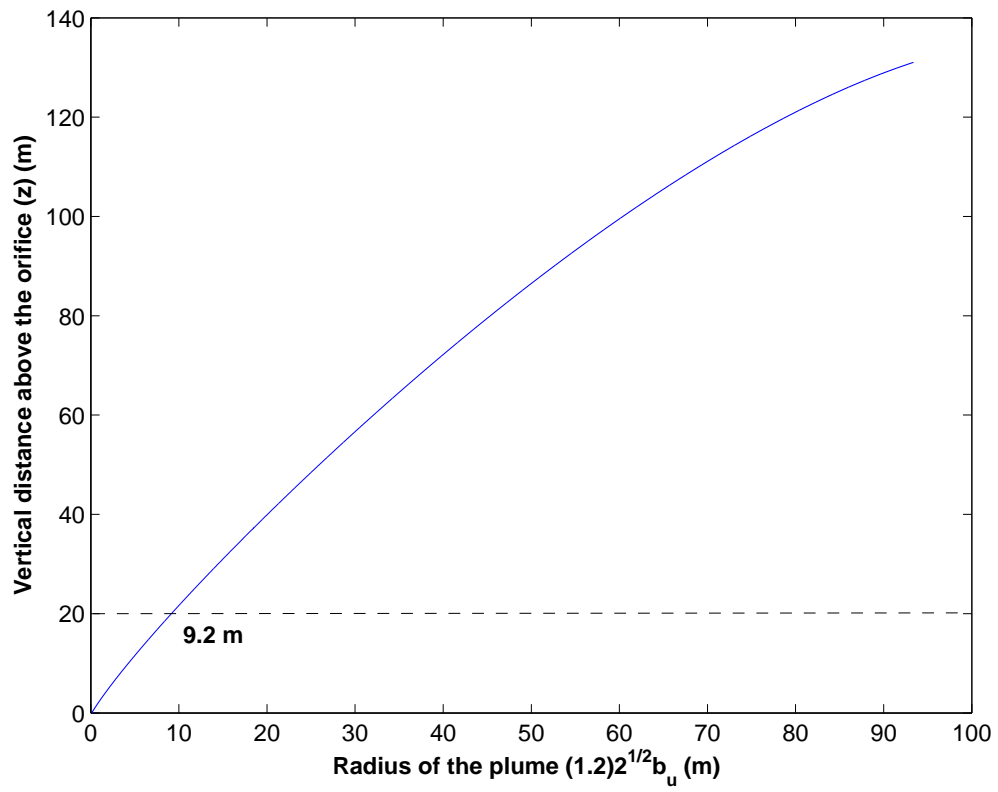


Figure 6.13: Radius of the plume.

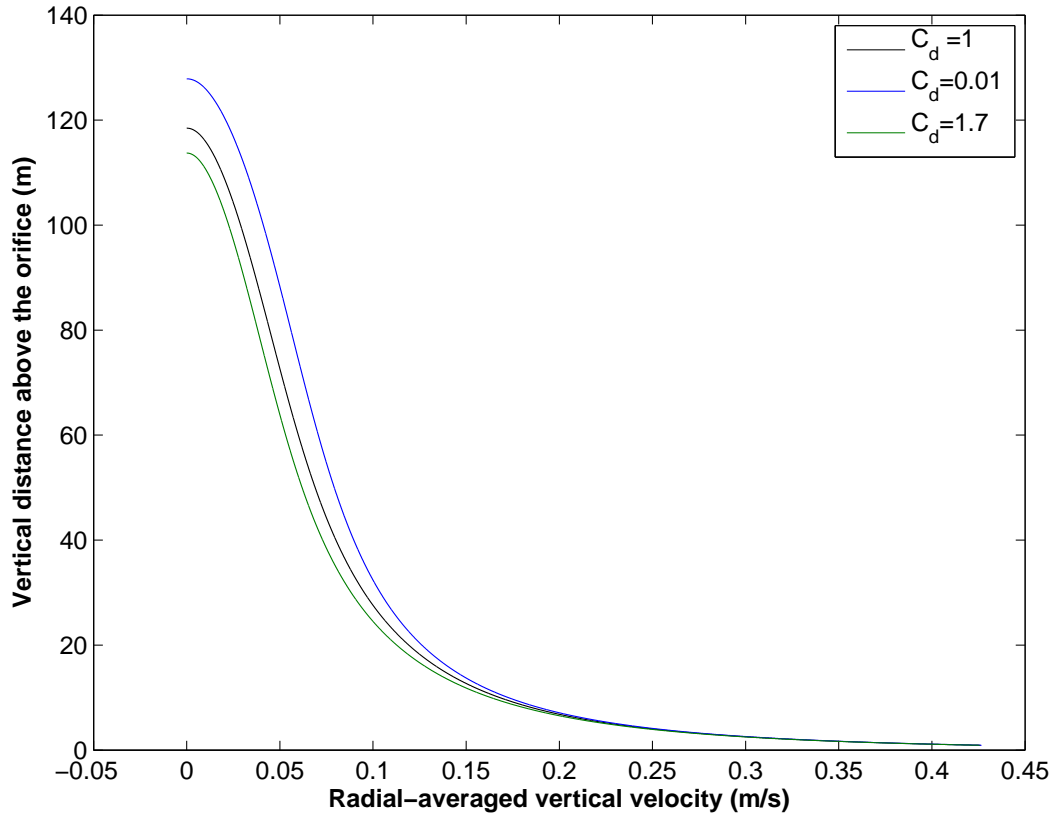


Figure 6.14: Radial-averaged vertical velocity of the plume for different drag coefficients:  $C_d = 0.01$  (blue line),  $C_d = 1$  (black line) and  $C_d = 1.7$  (green line).

vertical velocity of the plume for different drag coefficients ( $C_d = 0.01, 1$  and  $1.7$ ) with all the other parameters maintained as they were in the first model run. It is noted that, the plume's radial-averaged vertical velocity shows only a weak sensitivity to the variation of the drag coefficient. The uncertainty induced by a drag coefficient varying from 0.01 to 1.7 (the maximum value measured by Fan (1967)) is approximately 2 cm/s which is much smaller than the magnitude of the vertical velocity fluctuation shown in Figure 4.3.

Figure 6.15 shows the plume's radial averaged vertical velocity for the initial density deficit  $\eta_0 = 310$  and  $410 \text{ kg/m}^3$  which are  $50 \text{ kg/m}^3$  below and above the value used in

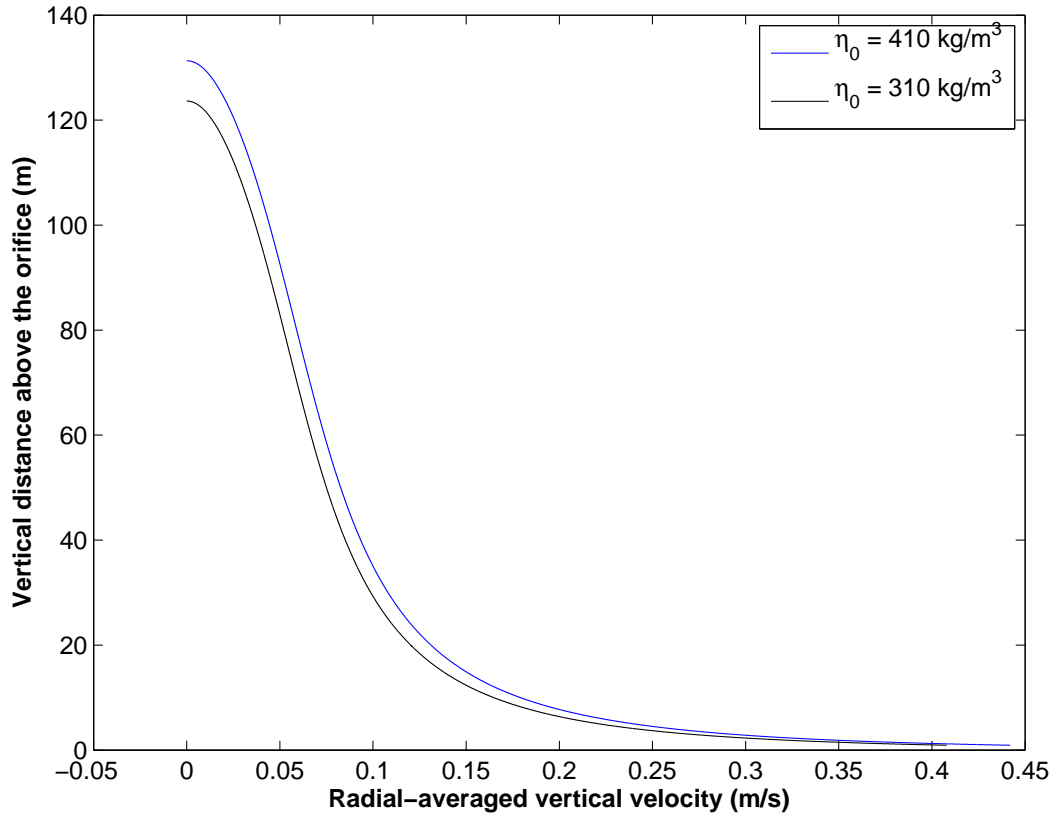


Figure 6.15: Radial-averaged vertical velocity of the plume with initial density deficit  $\eta_0 = 310 \text{ kg/m}^3$  (black line) and  $\eta_0 = 410 \text{ kg/m}^3$  (blue line).

previous model runs respectively. The subsequent vertical velocity difference is approximately 1 cm/s, which is much smaller than the magnitude of oscillation shown in Figure 4.3.

Figure 6.16 shows the plume's radial-averaged vertical velocity  $\langle W \rangle$  at 20 m above the orifice as a function of the horizontal cross-flow under different  $\alpha$  and  $\beta$  combinations. As  $\alpha$  increases from 0.06 to 0.08 while  $\beta$  remains the same,  $\langle W \rangle$  decreases by 4 cm/s at zero horizontal cross-flow. Meanwhile, the decrease of  $\langle W \rangle$  at the maximum horizontal cross-flow is negligible ( $< 1 \text{ cm/s}$ ). As  $\beta$  increases from 0.4 to 0.6 while  $\alpha$  remains the same,  $\langle W \rangle$  decreases by 3 cm/s at the maximum horizontal cross-flow and remains the same at zero horizontal cross-flow.

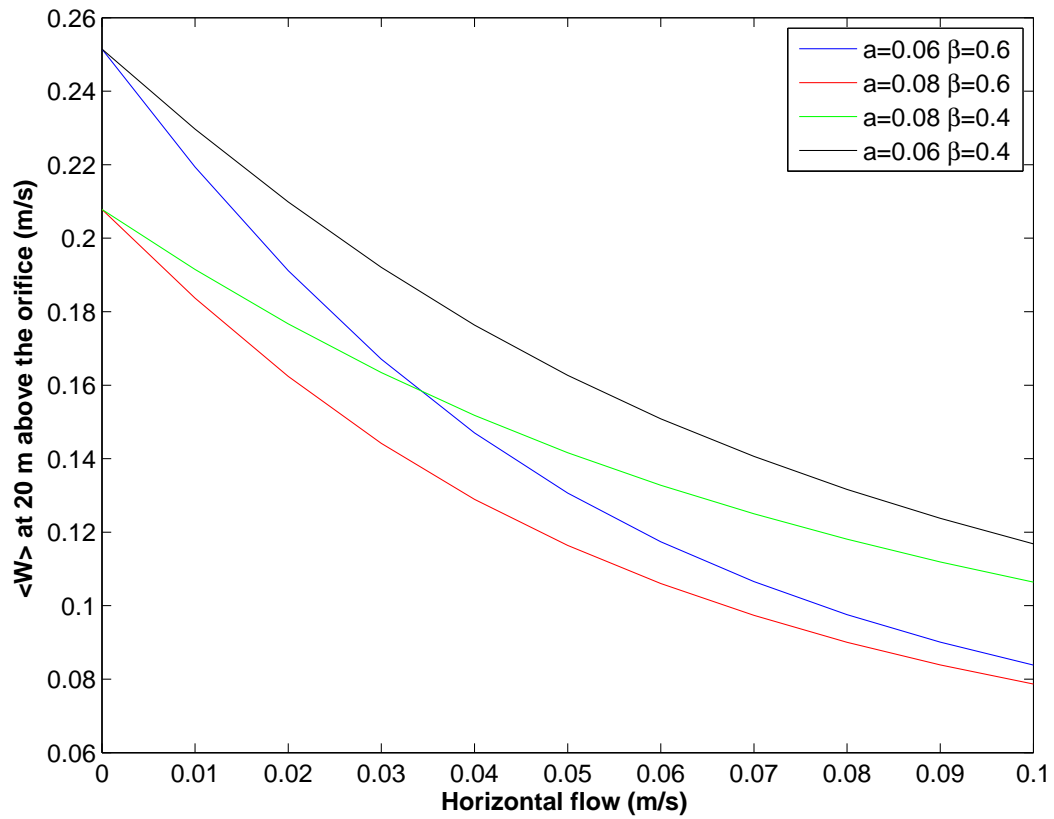


Figure 6.16:  $\langle W \rangle$  at 20 m above the orifice as a function of the horizontal cross-flow for different  $\alpha$  and  $\beta$  combinations.

## 6.8 SYNOPSIS

According to the model results, the comparison with the acoustic scintillation measurements and the sensitivity tests demonstrated above, several conclusions are reached and generalized as follows:

1. The radius of the plume produced by Dante increases nonlinearly along the plume's height above the orifice (see Figure 6.5).
2. The horizontal cross-flow bends and drifts the plume downstream.
3. The declination angle of the plume increases nonlinearly along the plume's height and reaches  $90^\circ$  at its terminal height.
4. The vertical velocity of the plume decreases along the plume's height (see Figure 6.7). An increased horizontal cross-flow leads to a decreased vertical velocity (see 6.11).
5. The bending caused by the horizontal cross-flow has a negligible effect on the vertical velocity oscillations observed in the acoustic scintillation measurement.

For further investigation of the plume's behavior during flooding tide and ebbing tide, two model runs are carried out with the horizontal cross-flow set to 6.2 cm/s and 1.1 cm/s (pinpointed by the dashed lines in Figure 6.10). According to the model results, the declination angle of the plume is enhanced during flooding tide and diminished during ebbing tide (see Figure 6.17). This is consistent with the conclusion drawn by Rona et al. (2006) that the entrainment rate correlates positively with the degree of bending of a hydrothermal plume. The increased terminal height during ebbing tide and decreased terminal height during flooding tide observed in the model result is also consistent with the observation made by Rona et al. (2006) and modeling prediction made by Middleton and Thomson (1986). The consistency between the model result and the acoustic scintillation measurement as well as the published results suggests the validity of the entrainment and tidal response hypothesis posed in Chapter 5. The entrainment rate is enhanced under a strong horizontal cross-flow

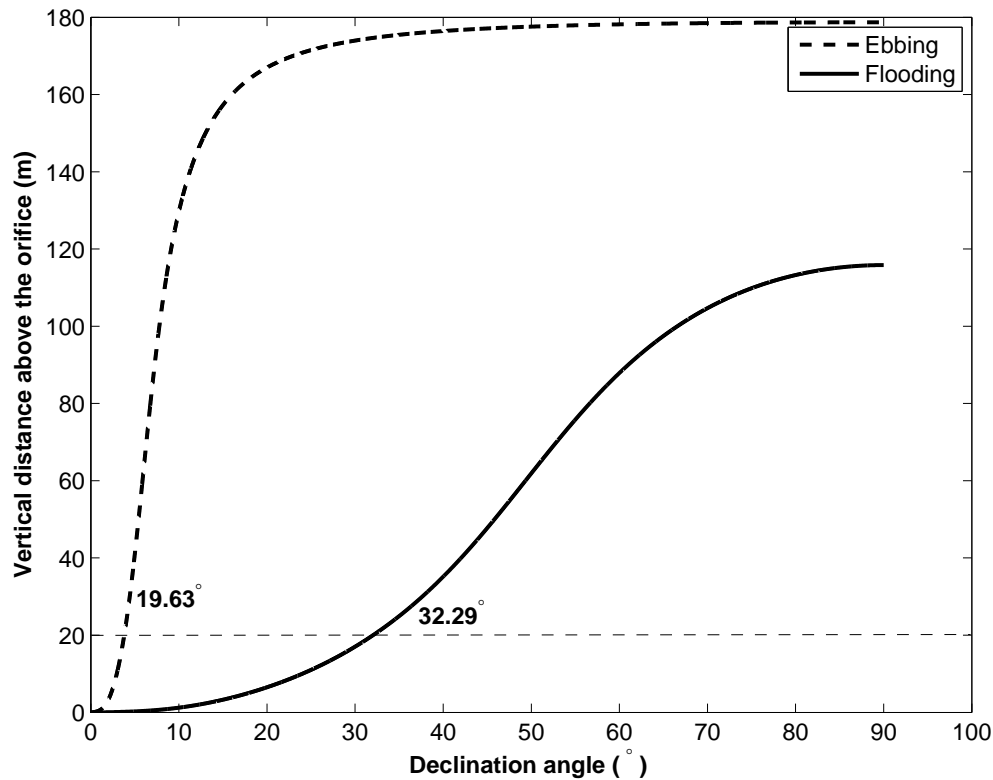


Figure 6.17: Declination angles of the plume: during ebbing tide (dashed line), during flooding tide (solid line)

(predominantly during flooding tide), which increases the dilution of the plume. In this case, the plume loses its buoyancy faster than usual and thus has reduced vertical velocity and terminal height. The bending of the plume is increased in this case due to the increased entrainment of horizontal momentum carried and the intensified drag force exerted by the horizontal cross-flow. In contrast, the plume vertical velocity as well as its terminal height increases under a weak horizontal cross-flow (during ebbing tide) due to the diminished entrainment rate which leads to a reduced dilution of the plume. The bending of the plume is weakened in this case. Furthermore, the consistency between the model and experimental results suggest

the validity of the linear additive form of the entrainment velocity as well as the applied entrainment coefficients ( $\alpha = 0.08$  and  $\beta = 0.5$ ). On average, such a combination of  $\alpha$  and  $\beta$  seem to represent the measurements of the plume's vertical velocity.

## CHAPTER 7

### BACK SCATTERING FROM THE PLUME

#### 7.1 BACK SCATTERING FROM TURBULENCE

The acoustic scintillation technology introduced in the previous chapters is based on the forward scattering of acoustic waves. Apart from forward scattering, many other researchers are using back scattering of acoustic waves to investigate hydrothermal plumes (Palmer and Rona, 1986; Rona et al., 1991; Bemis et al., 2002). Although the application of using back scattering techniques to probe hydrothermal plumes has been available for a long time, the mechanism within the plume dominating the back scattering of acoustic signals is still unclear. Palmer and Rona (1986) and Rona et al. (1991) hypothesize that the major back scatterer within a hydrothermal plume is the suspending particles and that back scattering from turbulence within the plume (temperature, salinity and velocity perturbations) is negligible. In this section, the turbulence effect (measured by forward scattering) will be quantified for comparison to backscattering from particles.

The theory used to estimate the scattering from turbulence was laid out by Batchelor (1959) and generalized by Morse and Ingard (1968) and Ross (1998). The wave equation to begin with has the general form,

$$\begin{aligned}\nabla^2 p + \frac{w^2}{c_0^2} p &= -f(\mathbf{r}) \\ &= \frac{2c'w^2}{c_0^3} p + \frac{\nabla \rho'}{\rho_0} \cdot \nabla p - \frac{ik}{c_0} (\mathbf{u}' \cdot \nabla) p - \rho_0 \nabla \cdot ((\mathbf{u}' \cdot \nabla) \mathbf{u} + (\mathbf{u} \cdot \nabla) \mathbf{u}').\end{aligned}\quad (7.1)$$

where  $c_0$  and  $\rho_0$  are the background sound velocity and density respectively,  $c'$  and  $\rho'$  are the corresponding turbulent perturbations and  $u'$  is the turbulent ambient velocity (zero mean

ambient velocity,  $u_0 = 0$ , is valid for very low Mach numbers,  $M = u_0/c_0 \ll 1$ ). The pressure and velocity perturbation caused by acoustic waves propagating through the medium is  $p$  and  $u$  respectively.

Equation (7.1) can be solved using the standard Green's function method (Morse and Ingard, 1968). The solution is written as

$$p(\mathbf{r}) = p_i + \int_{-\infty}^{\infty} f(\mathbf{r}_0)G(\mathbf{r}, \mathbf{r}_0)dV_0 \quad (7.2)$$

in which  $p_i$  is the incident wave and for a plane wave

$$\begin{aligned} p_i(\mathbf{r}) &= P_0 \exp(i\mathbf{k}_i \cdot (\mathbf{r} - \mathbf{r}') - i\omega t) \\ u_i(\mathbf{r}) &= \frac{\mathbf{n}_i}{c_0\rho_0}p_i(\mathbf{r}) \end{aligned} \quad (7.3)$$

where  $\mathbf{r}'$  is the location of the transmitter and  $\mathbf{n}_i = \mathbf{k}_i/k_i$  is the unit vector of the incident wave-number (see Figure 7.1). The Green's function for waves propagating in a free medium satisfying a radiation boundary condition with the turbulent source located at  $\mathbf{r}_0$  is,

$$G(\mathbf{r}, \mathbf{r}_0) = \frac{\exp(ik|\mathbf{r} - \mathbf{r}_0|)}{4\pi|\mathbf{r} - \mathbf{r}_0|}. \quad (7.4)$$

From the single scattering approximation introduced in Chapter 4,

$$p(\mathbf{r}) = p_i + p_s \quad (7.5)$$

where  $p_s$  is the sound field scattered from the turbulence within the medium. Comparing equation (7.5) with (7.2) and assuming the single scattering approximation, gives

$$p_s(\mathbf{r}) = \int \left\{ -\frac{2c'w^2}{c_0^3}p_i(\mathbf{r}_0) - \frac{\nabla\rho'}{\rho_0} \cdot \nabla p_i(\mathbf{r}_0) + \frac{ik}{c_0}\mathbf{u}' \cdot \nabla p_i(\mathbf{r}_0) + \rho_0\nabla \cdot (\mathbf{u}' \cdot \nabla \mathbf{u}_i + \mathbf{u}_i \cdot \nabla \mathbf{u}') \right\} \times G(\mathbf{r}, \mathbf{r}_0)dV_0. \quad (7.6)$$

Substituting equations (7.3) and (7.4) into equation (7.6) gives

$$p_s(\mathbf{r}) = \int \left\{ -k^2\frac{2c'}{c_0} - \frac{\nabla\rho'}{\rho_0} \cdot ik\mathbf{n}_i - 2k(k - i\mathbf{n}_i \cdot \nabla)(\mathbf{n}_i \cdot \frac{\mathbf{u}'}{c_0}) \right\} \times P_0 \exp(i\mathbf{k}_i \cdot (\mathbf{r}_0 - \mathbf{r}') - i\omega t)G(\mathbf{r}, \mathbf{r}_0)dV_0 \quad (7.7)$$

where  $w = c_0 k$ .

Assuming that the sound field  $p_s(\mathbf{r})$  is measured in the far-field of the scattering volume  $V_0$  ( $r \gg r_0$ ), then the Green's function can be simplified as

$$G(\mathbf{r}, \mathbf{r}_0) \approx \frac{\exp[ik(r - \mathbf{n}_s \cdot \mathbf{r}_0)]}{4\pi r}, \quad (7.8)$$

which is valid for  $\frac{r_0^2}{r} \ll \lambda$  where  $\lambda$  is the wave-length of the acoustic wave and  $\mathbf{r}_{0\perp}$  is the component of  $\mathbf{r}_0$  normal to  $\mathbf{n}_s$  ( $\mathbf{n}_s = \mathbf{r}/r$ ). Substituting equation (7.8) into equation (7.7) gives

$$p_s(\mathbf{r}) = -\frac{P_0 k^2 \exp(ikr - i\mathbf{k}_i \cdot \mathbf{r}')}{2\pi r} \int \left\{ \frac{c'}{c_0} + i \frac{\mathbf{n}_i \cdot \nabla}{2k} \left( \frac{\rho'}{\rho_0} \right) + \left( 1 - i \frac{\mathbf{n}_i \cdot \nabla}{k} \right) \left( \mathbf{n}_i \cdot \frac{\mathbf{u}'}{c_0} \right) \right\} \times \exp[ik(\mathbf{n}_i - \mathbf{n}_s) \cdot \mathbf{r}_0] dV_0. \quad (7.9)$$

The linear form of the equation of state is,

$$\frac{\rho'}{\rho_0} = \frac{\rho - \rho_0}{\rho_0} = -\alpha_t(T - T_0) + \beta_s(S - S_0) = -\alpha_t T' + \beta_s S' \quad (7.10)$$

where  $T'$  and  $S'$  are the ambient temperature and salinity perturbations while  $\alpha_t$  and  $\beta_s$  are the thermal expansion and haline contraction coefficients respectively. In addition, sound velocity in the ocean is a function of temperature, salinity and depth. By maintaining only the first order terms from the 'nine-term equation for sound speed in the oceans' derived by Mackenzie (1981) (see equation (3.48) and omitting the effect of depth), one has

$$c = 1448.96 + 4.591T + 1.340(S - 35). \quad (7.11)$$

The sound speed perturbation can then be written as,

$$\frac{c'}{c_0} = \frac{4.591(T - T_0) + 1.340(S - S_0)}{c_0} = \alpha_c T' + \beta_c S' \quad (7.12)$$

in which  $\alpha_c = 4.591/c_0$  and  $\beta_c = 1.340/c_0$ . Substituting equation (7.10) and equation (7.12) into equation (7.9) gives

$$p_s(\mathbf{r}) = -\frac{P_0 k^2 \exp(ikr - i\mathbf{k}_i \cdot \mathbf{r}')}{2\pi r} \int \left\{ \left( \alpha_c - i \frac{\mathbf{n}_i \cdot \nabla}{2k} \alpha_t \right) T' + \left( \beta_c + i \frac{\mathbf{n}_i \cdot \nabla}{2k} \beta_s \right) S' + \left( 1 - i \frac{\mathbf{n}_i \cdot \nabla}{k} \right) \left( \mathbf{n}_i \cdot \frac{\mathbf{u}'}{c_0} \right) \right\} \exp[ik(\mathbf{n}_i - \mathbf{n}_s) \cdot \mathbf{r}_0] dV_0. \quad (7.13)$$

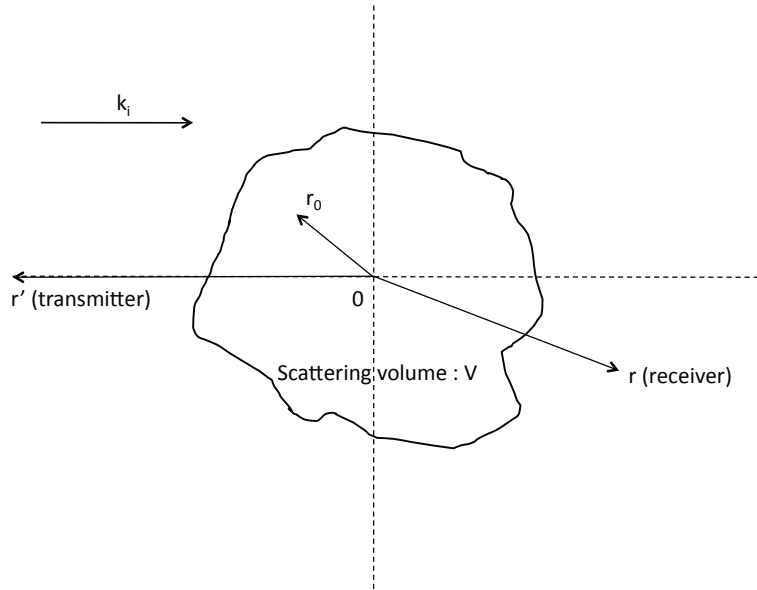


Figure 7.1: Scattering of sound wave from a turbulent medium.  $\mathbf{r}'$  location of the transmitter,  $\mathbf{r}$  location of the receiver,  $\mathbf{r}_0$  location of a turbulent microstructure within the scattering volume,  $\mathbf{k}_i$  incident wave-number.

The scattered sound field  $p_s(\mathbf{r})$  can be represented in its spectral domain based on Fourier transforms of the perturbations in temperature, salinity and velocity field

$$\begin{aligned}
 F_T(\mathbf{K}) &= \frac{1}{(2\pi)^3} \int \exp(-i\mathbf{K} \cdot \mathbf{r}_0) T'(\mathbf{r}_0) dV_0 \\
 F_S(\mathbf{K}) &= \frac{1}{(2\pi)^3} \int \exp(-i\mathbf{K} \cdot \mathbf{r}_0) S'(\mathbf{r}_0) dV_0 \\
 F_{u_i}(\mathbf{K}) &= \frac{1}{(2\pi)^3} \int \exp(-i\mathbf{K} \cdot \mathbf{r}_0) u'_i(\mathbf{r}_0) dV_0
 \end{aligned} \tag{7.14}$$

in which  $\mathbf{K} = k(\mathbf{n}_s - \mathbf{n}_i)$  is the Bragg wave-number (see Figure 7.2) and  $u_i = \mathbf{u}' \cdot \mathbf{n}_i$  is the turbulent velocity's component along the direction of the incident wave. Substituting equation (7.14) into equation (7.13) gives

$$p_s(\mathbf{r}) = -\frac{4\pi^2 P_0 k^2 \exp(ikr - i\mathbf{k}_i \cdot \mathbf{r}')}{r} \left\{ \left( \alpha_c + \frac{\mathbf{n}_i \cdot \mathbf{K}}{2k} \alpha_t \right) F_T(\mathbf{K}) + \right.$$

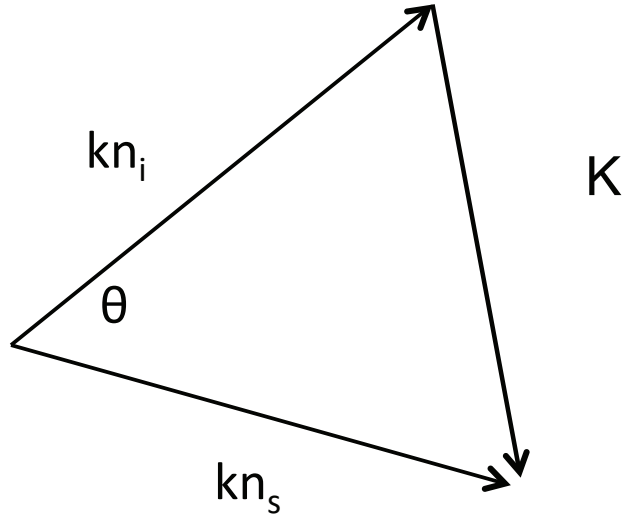


Figure 7.2: Bragg wave-number

$$\left. \begin{aligned} & \left( \beta_c - \frac{\mathbf{n}_i \cdot \mathbf{K}}{2k} \beta_s \right) F_S(\mathbf{K}) + \\ & \frac{k_i}{kc_0} \left( 1 + \frac{\mathbf{n}_i \cdot \mathbf{K}}{k} \right) F_{u_i}(\mathbf{K}) \end{aligned} \right\}. \quad (7.15)$$

According to Figure 7.2,

$$\mathbf{n}_i \cdot \mathbf{K} = \mathbf{n}_i \cdot k(\mathbf{n}_s - \mathbf{n}_i) = -2k \sin^2\left(\frac{\theta}{2}\right). \quad (7.16)$$

Substituting into equation (7.15) gives

$$p_s(\mathbf{r}) = -\frac{4\pi^2 P_0 k^2 \exp(ikr - i\mathbf{k}_i \cdot \mathbf{r}')}{r} \left\{ \begin{aligned} & \left( \alpha_c - \sin^2\left(\frac{\theta}{2}\right) \alpha_t \right) F_T(\mathbf{K}) + \\ & \left( \beta_c + \sin^2\left(\frac{\theta}{2}\right) \beta_s \right) F_S(\mathbf{K}) + \\ & \frac{k_i}{kc_0} \cos \theta F_{u_i}(\mathbf{K}) \end{aligned} \right\}. \quad (7.17)$$

By definition, the differential scattering cross-section (per unit volume) of the turbulent volume  $V$  can be represented as the volume scattering strength:

$$\begin{aligned}
S_V &= \frac{\sigma_s}{V} = \frac{r^2 \langle p_s p_s^* \rangle}{V \langle p_i p_i^* \rangle} \\
&= \frac{(2\pi)^4 k^4}{V} \langle (A(\theta) F_T(\mathbf{K}) + B(\theta) F_S(\mathbf{K}) + \frac{k_i \cos \theta}{c_0 k} F_{u_i}(\mathbf{K})) \times \\
&\quad (A(\theta) F_T^*(\mathbf{K}) + B(\theta) F_S^*(\mathbf{K}) + \frac{k_i \cos \theta}{c_0 k} F_{u_i}^*(\mathbf{K})) \rangle
\end{aligned} \tag{7.18}$$

where

$$\begin{aligned}
A(\theta) &= \alpha_c - \sin^2\left(\frac{\theta}{2}\right) \alpha_t, \\
B(\theta) &= \beta_c + \sin^2\left(\frac{\theta}{2}\right) \beta_s.
\end{aligned}$$

Since

$$\begin{aligned}
\langle F_T(\mathbf{K}) F_T^*(\mathbf{K}) \rangle &= \frac{V}{(2\pi)^3} \Phi_T(\mathbf{K}) \\
\langle F_S(\mathbf{K}) F_S^*(\mathbf{K}) \rangle &= \frac{V}{(2\pi)^3} \Phi_S(\mathbf{K}) \\
\langle F_{u_i}(\mathbf{K}) F_{u_j}^*(\mathbf{K}) \rangle &= \frac{V}{(2\pi)^3} \Phi_{ij}(\mathbf{K}) \\
\langle F_S(\mathbf{K}) F_T^*(\mathbf{K}) \rangle &= \langle F_T(\mathbf{K}) F_S^*(\mathbf{K}) \rangle = \frac{V}{(2\pi)^3} \Phi_{TS}(\mathbf{K})
\end{aligned} \tag{7.19}$$

where  $\Phi_T$ ,  $\Phi_S$  and  $\Phi_{ij}$  are the three dimensional power spectral density for temperature, salinity and turbulent velocity respectively and  $\Phi_{TS}$  is the co-spectrum between temperature and salinity. For isotropic turbulence,  $\Phi(\mathbf{K}) = \Phi(K)$  and  $\Phi_{ij}(\mathbf{K}) = (\delta_{ij} - \frac{K_i K_j}{K^2}) \frac{E(K)}{4\pi K^2}$  (Batchelor, 1952). Therefore the differential scattering cross-section can be written as

$$S_V = 2\pi k^4 (A(\theta)^2 \Phi_T(K) + B(\theta)^2 \Phi_S(K) + 2A(\theta)B(\theta) \Phi_{TS}(K) + (1 + \cos \theta) \frac{\cos^2 \theta E(K)}{8\pi c_0^2 K^2}). \tag{7.20}$$

For back scattering, according to Figure 7.2,  $\theta = \pi$  and  $K = 2k$ . The differential scattering cross-section then becomes

$$S_V = 2\pi k^4 (A(\pi)^2 \Phi_T(2k) + B(\pi)^2 \Phi_S(2k) + 2A(\pi)B(\pi) \Phi_{TS}(2k)) \tag{7.21}$$

where  $A(\pi) = \alpha_c - \alpha_t$  and  $B(\pi) = \beta_c + \beta_s$ . As discussed in Chapter 4, temperature perturbations are the dominant mechanism responsible for the scattering of sound waves from the turbulent medium. Therefore, equation (7.21) can be approximated as

$$S_V \approx 2\pi k^4 A(\pi)^2 \Phi_T(2k). \quad (7.22)$$

At the wave number  $K = 2k$ , the power spectral density of temperature perturbations is assumed to satisfy the Kolmogorov spectrum for isotropic and homogeneous turbulence,

$$\Phi_T(K) = 0.033 C_T^2 K^{-11/3}, \quad (7.23)$$

where  $C_T^2$  is the structure parameter of temperature perturbations. Based on the discussion made in Chapter 4,  $C_T^2$  can be calculated from the measured structure parameter for effective-refractive index fluctuations  $C_{eff}^2$  using the acoustic scintillation method,

$$C_{eff}^2 \approx 4.591^2 C_T^2 / c_0^2.$$

Substituting these equations into equation (7.22) gives

$$\begin{aligned} S_V &= 2\pi k^4 (\alpha_c - \alpha_t)^2 (.033) C_{eff}^2 \frac{c_0^2}{4.591^2} (2k)^{-11/3} \\ &= 7.746 \times 10^{-4} k^{1/3} (\alpha_c - \alpha_t)^2 C_{eff}^2 c_0^2 \\ &= 0.0153 C_{eff}^2 k^{1/3} (\text{m}^{-1}), \end{aligned} \quad (7.24)$$

for a sound velocity of 1480 m/s and a thermal expansion coefficient of  $10^{-4} \text{ }^\circ\text{C}^{-1}$ .

According to Figure 3.6, the mean value of the measured  $C_{eff}^2$  is  $4.5 \times 10^{-7} \text{ m}^{-2/3}$ . The frequency of the acoustic wave used for backscattering measurements is typically 200 kHz. Substituting these values into equation (7.24) gives  $S_V = 6.52 \times 10^{-8} \text{ m}^{-1}$ . It should be noted that the value derived for  $S_V$  may not be an accurate estimation because it is unknown whether the temperature perturbations still satisfy the Kolmogorov spectrum at a wave-number as high as  $2k$  (such a wave-number corresponds to turbulent eddies of the order of 3.7 mm). Such an assumption can be verified by measuring the Kolmogorov wave-number of the plume

$$\kappa_\nu = 2\pi(\epsilon/\nu^3)^{1/4}, \quad (7.25)$$

where  $\epsilon$  is the turbulent kinetic energy dissipation and  $\nu$  is the kinematic viscosity ( $1 \times 10^{-6} \text{ m}^2/\text{s}$ ). If  $\epsilon > 1 \times 10^{-8} \text{ W/kg}$ , then an inertial subrange is expected to hold out to wave-number  $2k$  and temperature perturbations still bear the Kolmogorov spectrum.

## 7.2 BACK SCATTERING FROM SUSPENDING PARTICLES

Similar to the estimation of back scattering of acoustic waves from the turbulence within the plume demonstrated in the last section, back scattering from suspending particles can be theoretically quantified using the single scattering approximation and Rayleigh scattering theory (refer to Section 4.1 for details). According to equation (3.7) and Figure 7.3, the back-scattered sound field produced by suspending particles within the plume can be written as

$$u_f(\mathbf{r}) = \int_{V'} A_0 f(\mathbf{i}, -\mathbf{i}) \frac{\exp[2ik(|\mathbf{r}_0 - \mathbf{r}'|) - \gamma_i]}{|\mathbf{r}_0 - \mathbf{r}'|^2} \rho_n dV'. \quad (7.26)$$

in which  $f(\mathbf{i}, -\mathbf{i})$  (given in equation (3.21)), is the scattering amplitude of a single particle in the backward direction based on Rayleigh scattering theory and  $\gamma_i = \int_{r_i}^{r_i'} \rho_n \sigma_t dr$  describes the attenuation of sound waves due to the absorption and scattering of the particles lying in the acoustic line-of-sight. For spherical incident waves,

$$u_i = A_0 \frac{\exp(ikr_0 - \gamma_0/2)}{r_0}, \quad (7.27)$$

in which  $\gamma_0 = \int_0^R \sigma_t \rho_n dr'$ . The differential back scattering cross-section (per unit volume) is then written as

$$\begin{aligned} S_V &= \frac{r^2 \langle u_f u_f^* \rangle}{\langle u_i u_i^* \rangle V} \\ &= \frac{r^4}{V} |f(\mathbf{i}, -\mathbf{i})|^2 \int_{V'} \frac{\exp(\gamma_0 - 2\gamma_i)}{|\mathbf{r}_0 - \mathbf{r}'|^4} \rho_n dV'. \end{aligned} \quad (7.28)$$

According to Figure 7.3, the volume of the plume illuminated by the incident wave is  $V = \pi R^2 h = 1.54 \times 10^3 \text{ m}^3$ . Suspending particles are assumed to be rigid spheres with grain size of  $250 \mu\text{m}$ . The particle number concentration density is given by equation (3.25) as  $\rho_n = 3.88 \times 10^4 \text{ particles/m}^3$ . Substituting  $V$  and  $\rho_n$  into equation (7.28) and numerically

calculating the integral gives,

$$S_V = 8.859 \times 10^{-5} \text{ m}^{-1}. \quad (7.29)$$

Note that, the differential back scattering cross-section (per unit volume) estimated this way is highly sensitive to the grain size of the suspending particles. The grain size ( $250\mu\text{m}$ ) used for deriving the value in equation (7.29) is likely to be an overestimate. If the particle's grain size is  $15\mu\text{m}$ ,  $S_V$  will reduce to  $1.89 \times 10^{-8} \text{ m}^{-1}$ . Therefore, an accurate measurement of the plume's suspending particles' grain size is needed to give a reliable estimation of the particles' contribution to back scattering of acoustic waves. Nonetheless it appears that the turbulent effect to backscattering could be smaller than the backscattering effect from suspended particles.

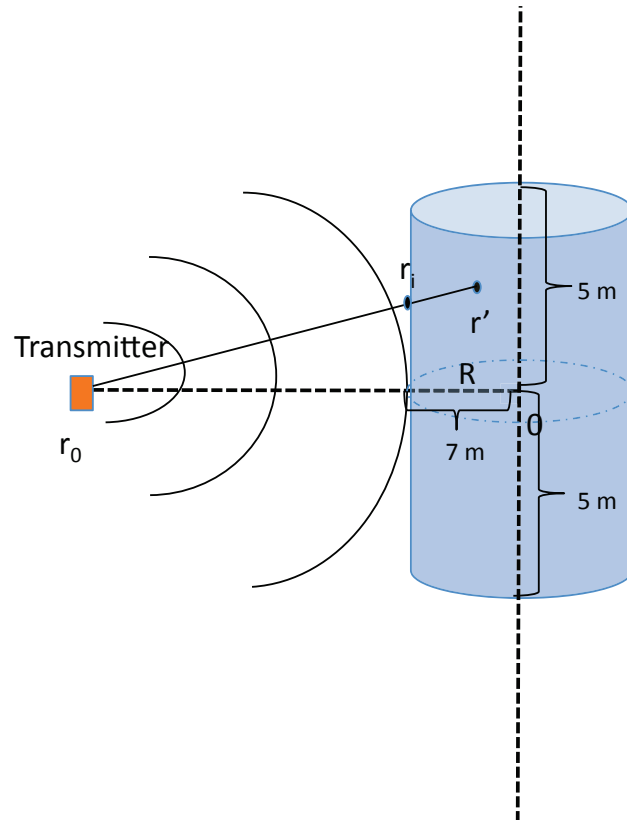


Figure 7.3: back scattering from suspending particles.  $\mathbf{r}_0$  location of the monostatic transmitter,  $\mathbf{r}'$  location of a single particle,  $\mathbf{r}_i$  intersection between the scattered acoustic line-of-sight and the boundary of the plume,  $\mathbf{R}$  radius of the plume.

## CHAPTER 8

### CONCLUSIONS AND SUGGESTIONS FOR FUTURE RESEARCH

#### 8.1 CONCLUSIONS

In this thesis, data collected at a vigorous deep ocean hydrothermal plume using the acoustic scintillation instrument is presented and analyzed to show the validity and prospect of using the acoustic scintillation method to investigate hydrothermal vents. An integral plume model is established to support the acoustic scintillation data and reveal the underlying mechanism for the interaction between the hydrothermal plume and its ambient environment shown in the data. The contribution of the turbulence and suspending particles within the plume to acoustic forward and back scattering is discussed and quantified theoretically in order to determine the major scattering mechanism within the plume. Several conclusions have been reached.

The effect of suspending particles within the plume on acoustic forward scattering and hence acoustic scintillation is discussed and quantified theoretically in Chapter 3. The theoretical framework is based on the single scattering approximation and Rayleigh scattering from particles and shows that the effect is negligible in comparison with the acoustic scintillation measurement. This suggests that turbulent microstructure from temperature variations, rather than the suspending particles, must be the dominant mechanism for the acoustic forward scattering from the hydrothermal plume. In fact, the measured log-amplitude spectrum is shown to fit an isotropic homogeneous turbulence model (i.e. the Kolmogorov spectrum) for the effective refractive index fluctuations very well (see Figure 3.5). In addition, the temperature standard deviation calculated from the acoustic scintillation data at 20 m above the sulfide structure of Dante (see Figure 3.9) is consistent with the CTD measurement and

hence temperature variations made with ROV Jason. Both of these results suggest that the acoustic scintillation method is most sensitive to temperature variations and can be used to quantify the temperature structure parameter ( $C_T^2 \propto C_{eff}^2$ ) that quantifies the level of turbulence in the plume.

Tidal oscillations were observed in both the turbulence ( $C_{eff}^2$ ) and vertical velocity measured at 20 m above the sulfide structure of Dante using the acoustic scintillation method (see Figure 3.6 and Figure 4.3), which indicates a significant physical interaction between the hydrothermal plume and ambient horizontal flows. In comparison with the predicted horizontal flow (extrapolated tidal currents plus the mean residual flow, Figure 5.8 and Figure 5.9), the interaction is characterized in Chapter 5 as the suppressed vertical velocity and turbulence during flooding tide (when the horizontal flow reaches a maximum) and the enhanced vertical velocity as well as turbulence during ebbing tide (when the horizontal flow reaches a minimum).

In chapter 6, an integral plume model based on the conservations laws of mass, momentum, density deficit and dissolved tracers is established using the Taylor's entrainment hypothesis with a linear additive form of the entrainment velocity. The model results show good consistency with the experimental measurements, which suggests that the interaction between the hydrothermal plume and horizontal flows is controlled by the tidally varying entrainment velocity, which reaches a minimum during ebbing tide (when the horizontal flow is weak) and reaches a maximum during flooding tide (when the horizontal flow is strong). More ambient sea water will be brought into the plume due to the increased entrainment during flooding tide making the plume cooler and slower, which leads to the reduced vertical velocity and turbulence within the plume. On the other hand, less ambient sea water will be brought into the plume during ebbing tide due to the reduced entrainment making the plume warmer and faster, which leads to the increased vertical velocity and turbulence. The discovery of the tidally varying entrainment is of great importance to the studying of

a hydrothermal plume's effect on its ambient environment (i.e. chemical mineral and larvae transport).

Acoustic back scattering from turbulent structures within the plume is quantified theoretically in Chapter 7 using the  $C_{eff}^2$  measured by acoustic scintillation (forward scattering). The result is compared with the back scattering from the suspending particles quantified using the same theories for forward scattering in Chapter 3. The result indicates that suspending particles within the plume play a dominant role in acoustic back scattering. However, this result is limited by the uncertainty of the particle grain size as well as the turbulence spectrum at high wave numbers.

## 8.2 SUGGESTIONS FOR FUTURE RESEARCH

Since the physical mechanism underlying the interaction between multiple coalescing plumes is still unclear, a vigorous plume formed from a single vent may serve better for the acoustic scintillation measurement as well as the integral plume model than an integrated plume from multiple vents (i.e. the plume above Dante). In addition, longer time series is needed to reveal the potential low frequency oscillations (seismic action induced) of a hydrothermal plume. The acoustic scintillation system described in this thesis and configured with reciprocal transmitting arrays can be integrated into the Neptune Canada underwater observatory (<http://www.neptunecanada.ca/about-neptune-canada>) for a long term observation and monitoring of the sound speed, horizontal flow and the vertical velocity of a hydrothermal plume. By measuring the ambient horizontal flow simultaneously along with the acoustic scintillation measurement will help better understand the effect of horizontal flows on the hydrothermal plume and the tidally varying entrainment mechanism.

## BIBLIOGRAPHY

- Allen, S. E. and Thomson, R. E. (1993). Bottom-trapped Subinertial Motions over Midocean Ridges in a Stratified Rotating Fluid. *Journal of Physical Oceanography*, 23:566–581.
- Baines, W. D. and Turner, J. S. (1969). Turbulent buoyant convection from a source in a confined region. *Journal of Fluid Mechanics*, 37:51–80.
- Baker, E. T., Feely, R. A., Mottl, M. J., Sansone, F. T., Wheat, C. G., Resing, J. A., and Lupton, J. E. (1994). Hydrothermal plumes along the East Pacific Rise, 8°40' to 11°50'N: Plume distribution and relationship to the apparent magmatic budget. *Earth Planetary Science Letters*, 128:1–17.
- Baker, E. T. and Massoth, G. J. (1987). Characteristics of hydrothermal plumes from two vent fields on the Juan de Fuca Ridge, northeast Pacific Ocean. *Earth Planetary Science Letters*, 85:59–73.
- Batchelor, G. K. (1952). *The Theory of Homogeneous Turbulence*. Cambridge University Press.
- Batchelor, G. K. (1959). Small-scale variation of convected quantities like temperature in turbulent fluid. *Journal of Fluid Mechanics*, 5:113–139.
- Bemis, K. G., Herzen, R. P. V., and Mottl, M. J. (1993). Geothermal Heat Flux From Hydrothermal Plumes on the Juan de Fuca Ridge. *Journal of Geophysical Research*, 98:6351–6365.
- Bemis, K. G., Rona, P. A., Jackson, D., Jones, C., Silver, D., and Mitsuzawa, K. (2002). A comparison of black smoker hydrothermal plume behavior at Monolith Vent and at Clam

- Acres Vent Field: Dependence on source configuration. *Marine Geophysical Researches*, 23:81–96.
- Berdeal, I. G., Hautala, S. L., Thomas, L. N., and Johnson, H. P. (2006). Vertical structure of time-dependent currents in a mid-ocean ridge axial valley. *Deep-Sea Research Part I*, 53:367–386.
- Bischoff, J. L. and Rosenbauer, R. J. (1985). An empirical equation of state for hydrothermal seawater (3.2 percent NaCl). *American Journal of Science*, 285:735–763.
- Butterfield, D. A., McDuff, R. E., Mottl, M. J., Lilley, M. D., Lupton, J. E., and Massoth, G. J. (1994). Gradients in the composition of hydrothermal fluids from the Endeavour segment vent field: Phase separation and brine loss. *Journal of Geophysical Research*, 99:9561–9583.
- Cannon, G. A. and Thomson, R. E. (1996). Characteristic of 4-day oscillations trapped by the Juan de Fuca Ridge. *Geophysical Research Letters*, 23:1613–1616.
- Clifford, S. and Farmer, D. (1983). Ocean flow measurements using acoustic scintillation. *Journal of the Acoustical Society of America*, 74:1826–1832.
- Clifford, S. F. (1971). Temporal-Frequency Spectra for a Spherical Wave Propagating through Atmospheric Turbulence. *Journal of the Optical Society of America*, 61:1285–1292.
- Converse, D., Holland, K., and Edmond, J. (1984). Flow rates in the axial hot springs of the East Pacific Rise (21°N): Implications for the heat budget and the formation of massive sulfide deposits. *Earth Planetary Science Letters*, 69:159–175.
- Crone, T. J. and Wilcock, W. S. D. (2005). Modeling the effects of tidal loading on mid-ocean ridge hydrothermal systems. *Geochemistry Geophysics Geosystems*, 6:doi:10.1029/2004GC000905.

- Delaney, J. R., Robigou, V., Mcduff, R. E., and Tivey, M. K. (1992). Geology of a Vigorous Hydrothermal System on the Endeavour Segment, Juan de Fuca Ridge. *Journal of Geophysical Research*, 97:19663–19682.
- Devenish, B. J., Rooney, G., Webster, H., and Thomson, D. (2010). The Entrainment Rate for Buoyant Plumes in a Crossflow. *Boundary-Layer Meteorology*, 134:411–439.
- Dewey, R. K. (1999). Mooring Design and Dynamics – a MATLAB package for designing and analyzing oceanographic moorings. *Marine Models Online*, pages 103–157.
- DiIorio, D. (1994). *Measurements of Turbulence Parameters and Observations of Multipath Arrivals in Two Contrasting Coastal Environments Using Acoustical Scintillation Analysis*. PhD thesis, University of Victoria.
- DiIorio, D. and Farmer, D. M. (1994). Path-averaged turbulent dissipation measurements using high-frequency acoustical scintillation analysis. *Journal of the Acoustical Society of America*, 96:1056–1069.
- DiIorio, D. and Farmer, D. M. (1998). Separation of current and sound speed in the effective refractive index for a turbulent environment using reciprocal acoustic transmission. *Journal of the Acoustical Society of America*, 103:321–329.
- DiIorio, D., Lemon, D., and Chave, R. (2005). A Self-Contained Acoustic Scintillation Instrument for Path-Averaged Measurements of Flow and Turbulence with Application to Hydrothermal Vent and Bottom Boundary Layer Dynamics. *Journal of Atmospheric and Oceanic Technology*, 22:1602–1617.
- Egbert, G., Bennett, A., and Foreman, M. (1994). TOPEX/Poseidon tides estimated using a global inverse model. *Journal of Geophysical Research*, 99:24821–24852.
- Egbert, G. and Erofeeva, S. (2002). Efficient inverse modeling of barotropic ocean tides. *Journal of Atmospheric and Oceanic Technology*, 19:183–204.

- Fan, L.-N. (1967). Turbulent buoyant jets into stratified or flowing ambient fluids. Technical report, California Institute of Technology.
- Farmer, D. M. and Clifford, S. F. (1986). Space-time acoustic scintillation analysis: A new technique for probing ocean flows. *IEEE Journal of Oceanic Engineering*, OE-11 (1):42–50.
- Farmer, D. M., Clifford, S. F., and Verrall, J. A. (1987). Scintillation structure of a turbulent tidal flow. *Journal of Geophysical Research*, 92:5369–5382.
- Feely, R., Geiselman, T., Baker, E., Massoth, G., and Hammond, S. (1990). Distribution and Composition of Hydrothermal Plume Particles from the Ashes Vent Field at Axial Volcano, Juan de Fuca Ridge. *Journal of Geophysical Research*, 95:12855–12873.
- Feely, R. A., Lewison, M., Massoth, G. J., Robert-Baldo, G., Lavelle, J. W., Byrne, R. H., Damm, K. L. V., and Herbert C.Curl, J. (1987). Composition and Dissolution of Black Smoker Particulates from Active Vents on the Juan de Fuca Ridge. *Journal of Geophysical Research*, 92:11347–11363.
- Fischer, H. B., List, E. J., Koh, R. C., Imberger, J., and Brooks, N. H. (1979). *Mixing in Inland and Coastal Waters*, chapter 9. Academic Press.
- Foreman, M. and Henry, R. F. (1979). Tidal analysis based on high and low water observations. Technical report, Institute of Ocean Sciences, Patricia Bay, Sidney, B.C., Canada.
- Foreman, M. G. G. (1977). Manual for tidal heights analysis and prediction. Technical report, Institute of Ocean Sciences, Patricia Bay, Sidney, B.C., Canada.
- Foreman, M. G. G. (1978). Manual for tidal currents analysis and prediction. Technical report, Institute of Ocean Sciences, Patricia Bay, Sidney, B.C., Canada.
- Fornari, D. J. and Embley, R. W. (1995). Tectonic and Volcanic Controls on Hydrothermal Processes at the Mid-Ocean Ridge: An Overview Based on Near-Bottom and Submersible Studies. In Humphris, S. E., Zierenberg, R. A., Mullineaux, L. S., and Thomson, R. E.,

- editors, *Seafloor Hydrothermal Systems: Physical, Chemical, Biological, and Geological Interactions*, pages 1–46. American Geophysical Union. Geophysical Monograph, vol: 91.
- Fujioka, K., Kobayashi, K., Kato, K., Aoki, M., Mitsuzawa, K., Kinoshita, M., and Nishizawa, A. (1997). Tide-related variability of TAG hydrothermal activity observed by deep-sea monitoring system and OBSH. *Earth Planetary Science Letters*, 153:239–250.
- Ginster, U. and Mottl, M. J. (1994). Heat flux from black smokers on the Endeavour and Cleft segments, Juan de Fuca Ridge. *Journal of Geophysical Research*, 99:4937–4950.
- Helfrich, K. R. and Speer, K. G. (1995). Oceanic Hydrothermal Circulation: Mesoscale and Basin-Scale Flow. In Humphris, S. E., Zierenberg, R. A., Mullineaux, L. S., and Thomson, R. E., editors, *Seafloor Hydrothermal Systems: Physical, Chemical, Biological, and Geological Interactions*, pages 347–356. American Geophysical Union. Geophysical Monograph, vol: 91.
- Hoult, D. P. and Weil, J. C. (1972). Turbulent plume in a laminar cross flow. *Atmospheric Environment*, 6.
- Ishimaru, A. (1978a). *Wave Propagation and Scattering in Random Media*, volume 2. Academic Press.
- Ishimaru, A. (1978b). *Wave Propagation and Scattering in Random Media*, volume 1. Academic Press.
- Jannasch, H. W. (1995). Microbial Interactions With Hydrothermal Fluids. In Humphris, S. E., Zierenberg, R. A., Mullineaux, L. S., and Thomson, R. E., editors, *Seafloor Hydrothermal Systems: Physical, Chemical, Biological, and Geological Interactions*, pages 273–296. American Geophysical Union. Geophysical Monography, vol : 91.
- Johnson, H. P. and Hautala, S. L. (2002). Hydrothermal circulation on the Northern Juan de Fuca Ridge. *EOS, Transactions, American Geophysical Union*, 83:73–79.

- Johnson, H. P., Hutnak, M., Dziak, R. P., Fox, C. G., Urcuyo, I., Cowen, J. P., and Nabelek, J. (2000). Earthquake-induced changes in a hydrothermal system on the Juan de Fuca mid-ocean ridge. *Nature*, 407:174–177.
- Johnson, H. P., Tivey, M. A., Bjorklund, T. A., and Salmi, M. S. (2010). Hydrothermal circulation within the Endeavour Segment, Juan de Fuca Ridge. *Geochemistry Geophysics Geosystems*, 11.
- Kelley, D. S., Delaney, J. R., Lilley, M. D., and Butterfield, D. A. (2001). Vent Field Distribution and Evolution Along the Endeavour Segment, Juan de Fuca Ridge. *EOS, Transactions, American Geophysical Union*, 82 (47):F612.
- Kinoshita, M., Herzen, R. P. V., Matsubayashi, O., and Fujioka, K. (1998). Tidally-driven effluent detected by long-term temperature monitoring at the TAG hydrothermal mound, Mid-Atlantic Ridge. *Physics of The Earth and Planetary Interiors*, 108:143–154.
- Larson, B. I. and Lilley, M. D. (2002). Tidal perturbations of a submarine hydrothermal system. *EOS, Transactions, American Geophysical Union*, 83 (4). Ocean Sci. Meet. Suppl. Abstract OS31F-94.
- Little, S. A., Stolzenbach, K. D., and Grassle, F. J. (1988). Tidal current effects on temperature in diffuse hydrothermal flow: Guaymas basin. *Geophysical Research Letters*, 15:1491–1494.
- Mackenzie, K. V. (1981). Nine-term equation for sound speed in the oceans. *Journal of the Acoustical Society of America*, 70:807–812.
- Marsh, A. G., Mullineaux, L. S., Young, C. M., and Manahan, D. T. (2000). Larval dispersal potential of the tubeworm *Riftia pachyptila* at deep-sea hydrothermal vents. *Nature*, 411:77–80.
- McDuff, R. E. (1995). Physical Dynamics of Deep-Sea Hydrothermal Plumes. In Humphris, S. E., Zierenberg, R. A., Mullineaux, L. S., and Thomson, R. E., editors, *Seafloor*

- Hydrothermal Systems: Physical, Chemical, Biological, and Geological Interactions*, pages 357–368. American Geophysical Union. Geophysical Monography, vol : 91.
- McDuff, R. E. and Delaney, J. R. (1995). Periodic variability in fluid temperature at a seafloor hydrothermal vent. *EOS, Transactions, American Geophysical Union*, 76 (46). Fall Meet. Supl., F710.
- Medwin, H. and Clay, C. S. (1998). *Fundamentals of Acoustical Oceanography*. Academic Press.
- Middleton, J. M. and Thomson, R. E. (1986). Modeling the rise of hydrothermal plumes. *Canadian Technical Report of Hydrography and Ocean Sciences*, 69.
- Morse and Ingard (1968). *Theoretical Acoustics*. Princeton University Press.
- Morton, B., Taylor, G., and Turner, J. (1956). Turbulent Gravitational Convection from Maintained and Instantaneous Sources. *Proceedings of the Royal Society of London*, 234:1–23.
- Oeschger, J. and Goodman, L. (1996). Acoustic scattering from a thermally driven buoyant plume. *Journal of the Acoustical Society of America*, 100:1353–1367.
- Ostashev, V. E. (1991). Propagation and scattering of sound waves in the turbulent media (atmosphere or ocean). *Atmospheric Optics*, 4:653–656.
- Palmer, D. (1996). Rayleigh scattering from nonspherical particles. *Journal of the Acoustical Society of America*, 99:1901–1912.
- Palmer, D. and Rona, P. (1986). Acoustic imaging of high-temperature hydrothermal plumes at sea floor spreading centers. *Journal of the Acoustical Society of America*, 80:888–898.
- Palmer, D. R. (2009). Coherent and incoherent scattering by a plume of particles advected by turbulent velocity flow. *Journal of the Acoustical Society of America*, 126(2):587–598.

- Papanicolaou, P. N. and List, E. (1988). Investigation of round vertical turbulent buoyant jet. *Journal of Fluid Mechanics*, 195:341–391.
- Pawlowicz, R., Beardsley, B., and Lentz, S. (2002). Classical tidal harmonic analysis including error estimates in MATLAB using T-TIDE. *Computer and Geosciences*, 28:929–937.
- Pruis, M. J. and Johnson, H. P. (2004). Tapping into the sub seafloor: Examining diffuse flow and temperature form an active seamount on the Juan de Fuca Ridge. *Earth Planetary Science Letters*, 217:379–388.
- Riddihough, R. (1984). Recent Movements of the Juan de Fuca Plate System. *Journal of Geophysical Research*, 89:6980–6994.
- Rona, P. A., Bemis, K. G., Jones, C. D., and Jackson, D. R. (2006). Entrainment and bending in a major hydrothermal plume, Main Endeavour Field, Juan de Fuca Ridge. *Geophysical Research Letters*, 33:doi:10.1029/2006GL027211.
- Rona, P. A., Bemis, K. G., Silver, D., and Jones, C. D. (2002). Acoustic imaging, visualization and quantification of buoyant hydrothermal plumes in the ocean. *Marine Geophysical Researches*, 23:147–168.
- Rona, P. A., Palmer, D. R., Jones, C., Chaves, D. A., Czarnecki, M., Carey, E. W., and Guerrero, J. C. (1991). Acoustic imaging of hydrothermal plumes: East pacific rise. 21°N. 109°W. *Geophysical Research Letters*, 18:2233–2236.
- Ross, T. (1998). *Sound Scattering from Oceanic Turbulence*. PhD thesis, University of Victoria.
- Roth, S. E. and Dymond, J. (1989). Transport and settling of organic material in a deep-sea hydrothermal plume: evidence from particle flux measurements. *Deep-Sea Research Part I*, 36:1237–1254.

- Rytov, S., Kravtsov, Y., and Tatarskii, V. (1989). *Principles of Statistical Radiophysics*, volume 3. Springer-Verlag.
- Schultz, A., Delaney, J. R., and McDuff, R. E. (1992). On the partitioning of heat flux between diffuse and point source seafloor venting. *Journal of Geophysical Research*, 97:12299–12314.
- Shampine, L. F. (2008). Vectorized adaptive quadrature in MATLAB. *Journal of Computational and Applied Mathematics*, 211:131–140.
- Stahr, F. R., McDuff, R. E., Yoerger, D. R., Bradley, A. M., and Nakamura, K. (2000). Heat flux measurements at the Main Endeavour vent field, Juan de Fuca Ridge. *EOS, Transactions, American Geophysical Union*, 81 (48):Abstract OS521–03.
- Stein, C. and Stein, S. (1994). Constraints on hydrothermal heat flux through the oceanic lithosphere from global heat flow. *Journal of Geophysical Research*, 99:3081–3095.
- Stein, C. A. and Stein, S. (1992). A model for the global variation in oceanic depth and heat flow with lithospheric age. *Nature*, 359:123–129.
- Stommel, H. (1982). Is the South Pacific Helium-3 plume dynamically active? *Earth Planetary Science Letters*, 61:63–67.
- Tatarskii, V. (1961). *Wave Propagation in a Turbulent Medium*. McGraw-Hill Book Company, Inc.
- Tatarskii, V. I. (1971). *The Effects of the Turbulent Atmosphere on Wave Propagation*. Translated from Russian by Israel Program for Scientific Translations, Jerusalem.
- Tennekes and Lumley (1972). *A First Course in Turbulence*. The MIT Press.
- Thomson, R., Delaney, E. E., McDuff, R. E., Janecky, D. R., and McClain, J. S. (1992). Physical characteristics of the Endeavour Ridge hydrothermal plume during July 1988. *Earth Planetary Science Letters*, 111:141–154.

- Thomson, R. E., Mihaly, S. F., Rabinovich, A. B., McDuff, R. E., Veirs, S. R., and Stahr, F. R. (2003). Constrained circulation at Endeavour ridge facilitates colonization by vent larvae. *Nature*, 424:545–549.
- Thomson, R. E., Roth, S. E., and Dymond, J. (1990). Near-Inertial Motions Over a Mid-Ocean Ridge: Effects of Topography and Hydrothermal Plumes. *Journal of Geophysical Research*, 95:7261–7278.
- Thomson, R. E., Subbotina, M. M., and Anisimov, M. V. (2005). Numerical simulation of hydrothermal vent-induced circulation at Endeavour Ridge. *Journal of Geophysical Research*, 110.
- Turner, J. (1986). Turbulent entrainment: the development of the entrainment assumption, and its application to geophysical flows. *Journal of Fluid Mechanics*, 173:431–471.
- Turner, J. and Campbell, I. (1987). Temperature, density and buoyancy fluxes in 'black smoker' plumes, and the criterion for buoyancy reversal. *Earth Planetary Science Letters*, 86:85–92.
- Veirs, S. R., McDuff, R. E., and Stahr, F. R. (2006). Magnitude and variance of near-bottom horizontal heat flux at the Main Endeavour hydrothermal vent field. *Geochemistry Geophysics Geosystems*, 7 (2):doi:10.1029/2005GC000952.
- Webster, H. and Thomson, D. (2002). Validation of a Lagrangian model plume rise scheme using the Kincaid data set. *Atmospheric Environment*, 36:5031–5042.
- Wetzler, M. A., Lavelle, J. W., Cannon, G. A., and Baker, E. T. (1998). Variability of temperature and currents measured near Pipe Organ hydrothermal vent site. *Marine Geophysical Researches*, 20:505–516.

## APPENDIX A

### COEFFICIENTS OF THE CONSERVATION EQUATIONS

#### A.1 CONSERVATION EQUATION OF MASS

By calculating the derivative of the product on the left hand side, equation (6.57) becomes

$$b_1 \frac{db_u}{ds} + u_1 \frac{dU_m}{ds} + \lambda_1 \frac{d\theta}{ds} + t_1 \frac{dT_m}{ds} + s_1 \frac{dS_m}{ds} + \kappa_1 \frac{d\eta_m}{ds} = R_1 \quad (\text{A.1})$$

where  $b_1$ ,  $u_1$ ,  $\lambda_1$ ,  $t_1$ ,  $s_1$  and  $\kappa_1$  are the derivative coefficients and they are functions of the unknown variables  $b_u$ ,  $U_m$ ,  $\theta$ ,  $T_m$ ,  $S_m$  and  $\eta_m$ . The explicit forms are as follows

$$b_1 = b_u[\rho_a(0.864U_m + 2U_a \cos \theta) - \eta_m(1.080U_a \cos \theta + 0.57U_m)], \quad (\text{A.2})$$

$$u_1 = b_u^2(\rho_a 0.432 - \eta_m 0.285), \quad (\text{A.3})$$

$$\lambda_1 = b_u^2(0.540\eta_m U_a \sin \theta - U_a \rho_a \sin \theta), \quad (\text{A.4})$$

$$t_1 = 0, \quad (\text{A.5})$$

$$s_1 = 0, \quad (\text{A.6})$$

$$\kappa_1 = -b_u^2(0.540U_a \cos \theta + 0.285U_m). \quad (\text{A.7})$$

$$R_1 = \sqrt{2}b_u \rho_a E - b_u^2(0.432U_m + U_a \cos \theta) \frac{d\rho_a}{ds}. \quad (\text{A.8})$$

#### A.2 CONSERVATION EQUATION OF VERTICAL MOMENTUM

By calculating the derivative of the product on the left hand side, equation (6.58) becomes

$$b_2 \frac{db_u}{ds} + u_2 \frac{dU_m}{ds} + \lambda_2 \frac{d\theta}{ds} + t_2 \frac{dT_m}{ds} + s_2 \frac{dS_m}{ds} + \kappa_2 \frac{d\eta_m}{ds} = R_2. \quad (\text{A.9})$$

The explicit mathematical representations of the derivative coefficients and the right hand side are as follows

$$b_2 = 2b_u \sin \theta [\rho_a (U_a^2 \cos^2 \theta + 0.245U_m^2 + 0.865U_a U_m \cos \theta) - \eta_m (0.540U_a^2 \cos^2 \theta + 0.57U_a U_m \cos \theta + 0.185U_m^2)], \quad (\text{A.10})$$

$$u_2 = b_u^2 \sin \theta [\rho_a (0.490U_m + 0.865U_a \cos \theta) - \eta_m (0.57U_a \cos \theta + 0.370U_m)], \quad (\text{A.11})$$

$$\begin{aligned} \lambda_2 = & b_u^2 \cos \theta [\rho_a (U_a^2 \cos^2 \theta + 0.245U_m^2 + 0.865U_a U_m \cos \theta) - \\ & \eta_m (0.540U_a^2 \cos^2 \theta + 0.57U_a U_m \cos \theta + 0.185U_m^2)] + \\ & b_u^2 \sin \theta [-\rho_a (2U_a^2 \cos \theta \sin \theta + 0.865U_a U_m \sin \theta) + \\ & \eta_m (1.080U_a^2 \cos \theta \sin \theta + 0.57U_a U_m \sin \theta)], \end{aligned} \quad (\text{A.12})$$

$$t_2 = 0, \quad (\text{A.13})$$

$$s_2 = 0, \quad (\text{A.14})$$

$$\kappa_2 = -b_u^2 \sin \theta (0.540U_a^2 \cos^2 \theta + 0.57U_a U_m \cos \theta + 0.185U_m^2), \quad (\text{A.15})$$

$$R_2 = 0.540b_u^2 g \eta_m - \frac{F_D \cos \theta}{2\pi} - b_u^2 \sin \theta (U_a^2 \cos^2 \theta + 0.245U_m^2 + 0.865U_a U_m \cos \theta) \frac{d\rho_a}{ds}. \quad (\text{A.16})$$

### A.3 CONSERVATION EQUATION OF HORIZONTAL MOMENTUM

By calculating the derivative of the product on the left hand side, equation (6.59) becomes

$$b_3 \frac{db_u}{ds} + u_3 \frac{dU_m}{ds} + \lambda_3 \frac{d\theta}{ds} + t_3 \frac{dT_m}{ds} + s_3 \frac{dS_m}{ds} + \kappa_3 \frac{d\eta_m}{ds} = R_3. \quad (\text{A.17})$$

The explicit mathematical representations of the derivative coefficients and the right hand side are as follows

$$b_3 = 2b_u \cos \theta [\rho_a (U_a^2 \cos^2 \theta + 0.2454U_m^2 + 0.865U_a U_m \cos \theta) - \eta_m (0.540U_a^2 \cos^2 \theta + 0.57U_a U_m \cos \theta + 0.185U_m^2)] \quad (\text{A.18})$$

$$u_3 = b_u^2 \cos \theta [\rho_a(0.4908U_m + 0.865U_a \cos \theta) - \eta_m(0.57U_a \cos \theta + 0.370U_m)], \quad (\text{A.19})$$

$$\begin{aligned} \lambda_3 = & b_u^2 \sin \theta [-\rho_a(U_a^2 \cos^2 \theta + 0.2454U_m^2 + 0.865U_aU_m \cos \theta) + \\ & \eta_m(0.540U_a^2 \cos^2 \theta + 0.57U_aU_m \cos \theta + 0.185U_m^2)] + \\ & b_u^2 \cos \theta [-\rho_a(2U_a^2 \cos \theta \sin \theta + 0.865U_aU_m \sin \theta) + \\ & \eta_m(1.080U_a^2 \cos \theta \sin \theta + 0.57U_aU_m \sin \theta)], \end{aligned} \quad (\text{A.20})$$

$$t_3 = 0, \quad (\text{A.21})$$

$$s_3 = 0, \quad (\text{A.22})$$

$$\kappa_3 = -b_u^2 \cos \theta (0.540U_a^2 \cos^2 \theta + 0.57U_aU_m \cos \theta + 0.185U_m^2), \quad (\text{A.23})$$

$$R_3 = \rho_a \sqrt{2} b_u U_a E + \frac{F_D \sin \theta}{2\pi} - b_u^2 \cos \theta (U_a^2 \cos^2 \theta + 0.2454U_m^2 + 0.865U_aU_m \cos \theta) \frac{d\rho_a}{ds} \quad (\text{A.24})$$

#### A.4 CONSERVATION EQUATION OF TEMPERATURE ANOMALY

By calculating the derivative of the product on the left hand side, equation (6.60) becomes

$$b_4 \frac{db_u}{ds} + u_4 \frac{dU_m}{ds} + \lambda_4 \frac{d\theta}{ds} + t_4 \frac{dT_m}{ds} + s_4 \frac{dS_m}{ds} + \kappa_4 \frac{d\eta_m}{ds} = R_4. \quad (\text{A.25})$$

The explicit mathematical representations of the derivative coefficients and the right hand side are as follows

$$b_4 = T_m b_u [\rho_a(1.080U_a \cos \theta + 0.570U_m) - \eta_m(0.416U_m + 0.676U_a \cos \theta)], \quad (\text{A.26})$$

$$u_4 = T_m b_u^2 (0.285\rho_a - 0.208\eta_m), \quad (\text{A.27})$$

$$\lambda_4 = T_m b_u^2 (-0.540\rho_a U_a \sin \theta + 0.338\eta_m U_a \sin \theta), \quad (\text{A.28})$$

$$t_4 = b_u^2 [\rho_a(0.540U_a \cos \theta + 0.285U_m) - \eta_m(0.338U_a \cos \theta + 0.208U_m)], \quad (\text{A.29})$$

$$s_4 = 0, \quad (\text{A.30})$$

$$\kappa_4 = -T_m b_u^2 (0.338 U_a \cos \theta + 0.208 U_m), \quad (\text{A.31})$$

$$R_4 = -\frac{dT_a}{ds} b_u^2 [\rho_a (0.432 U_m + U_a \cos \theta) - \eta_m (0.540 U_a \cos \theta + 0.285 U_m)] - T_m b_u^2 (0.285 U_m + 0.540 U_a \cos \theta) \frac{d\rho_a}{ds}. \quad (\text{A.32})$$

#### A.5 CONSERVATION EQUATION OF SALINITY ANOMALY

By calculating the derivative of the product on the left hand side, equation (6.61) becomes

$$b_5 \frac{db_u}{ds} + u_5 \frac{dU_m}{ds} + \lambda_5 \frac{d\theta}{ds} + t_5 \frac{dT_m}{ds} + s_5 \frac{dS_m}{ds} + \kappa_5 \frac{d\eta_m}{ds} = R_5. \quad (\text{A.33})$$

The explicit mathematical representations of the derivative coefficients and the right hand side are as follows

$$b_5 = S_m b_u [\rho_a (1.080 U_a \cos \theta + 0.570 U_m) - \eta_m (0.416 U_m + 0.676 U_a \cos \theta)], \quad (\text{A.34})$$

$$u_5 = S_m b_u^2 (0.285 \rho_a - 0.208 \eta_m), \quad (\text{A.35})$$

$$\lambda_5 = S_m b_u^2 (-0.540 \rho_a U_a \sin \theta + 0.338 \eta_m U_a \sin \theta), \quad (\text{A.36})$$

$$t_5 = 0, \quad (\text{A.37})$$

$$s_5 = b_u^2 [\rho_a (0.540 U_a \cos \theta + 0.285 U_m) - \eta_m (0.338 U_a \cos \theta + 0.208 \eta_m U_m)], \quad (\text{A.38})$$

$$\kappa_5 = -S_m b_u^2 (0.338 U_a \cos \theta + 0.208 U_m), \quad (\text{A.39})$$

$$R_5 = -\frac{dS_a}{ds} b_u^2 [\rho_a (0.432 U_m + U_a \cos \theta) - \eta_m (0.540 U_a \cos \theta + 0.285 U_m)] - S_m b_u^2 (0.285 U_m + 0.540 U_a \cos \theta) \frac{d\rho_a}{ds}. \quad (\text{A.40})$$

## A.6 CONSERVATION EQUATION OF DENSITY DEFICIT

By calculating the derivative of the product on the left hand side, equation (6.62) becomes

$$b_6 \frac{db_u}{ds} + u_6 \frac{dU_m}{ds} + \lambda_6 \frac{d\theta}{ds} + t_6 \frac{dT_m}{ds} + s_6 \frac{dS_m}{ds} + \kappa_6 \frac{d\eta_m}{ds} = R_6. \quad (\text{A.41})$$

The explicit mathematical representations of the derivative coefficients and the right hand side are as follows

$$b_6 = \frac{b_u \eta_m}{\rho_a} [\rho_a (0.570 U_m + 1.080 U_a \cos \theta) - \eta_m (0.676 U_a \cos \theta + 0.416 U_m)] \quad (\text{A.42})$$

$$u_6 = \frac{b_u^2 \eta_m}{\rho_a} (0.285 \rho_a - 0.208 \eta_m), \quad (\text{A.43})$$

$$\lambda_6 = \frac{b_u^2 \eta_m}{\rho_a} (-0.540 \rho_a U_a \sin \theta + 0.338 \eta_m U_a \sin \theta), \quad (\text{A.44})$$

$$t_6 = 0, \quad (\text{A.45})$$

$$s_6 = 0, \quad (\text{A.46})$$

$$\kappa_6 = \frac{b_u^2}{\rho_a} [\rho_a (0.285 U_m + 0.540 U_a \cos \theta) - \eta_m (0.676 U_a \cos \theta + 0.416 U_m)], \quad (\text{A.47})$$

$$R_6 = -\frac{d\epsilon}{ds} b_u^2 [\rho_a (0.432 U_m + U_a \cos \theta) - \eta_m (0.54 U_a \cos \theta + 0.285 U_m)] + \frac{b_u^2 \eta_m^2}{\rho_a^2} (0.338 U_a \cos \theta + 0.208 U_m) \frac{d\rho_a}{ds}. \quad (\text{A.48})$$